ACTIVE CONTROL OF AIRCRAFT WING VIBRATION

2023
MASTER THESIS
MECHANICAL ENGINEERING

Hadi Mostafa Kadhim ALTALAB

Thesis Advisor
Assist. Prof. Dr. Mehmet BAKIRCI
Assist. Prof. Dr. Moammed Jawad MOHAMMED

ACTIVE CONTROL OF AIRCRAFT WING VIBRATION

Hadi Mostafa Kadhim ALTALAB

Thesis Advisor

Assist. Prof. Dr. Mehmet BAKIRCI

Assist. Prof. Dr. Moammed Jawad MOHAMMED

T.C.

Karabük University

Institute of Graduate

Programs Department of Mechanical Engineering

Prepared as

Master Thesis

KARABÜK

June 2023

I certify that in my opinion the thesis submitted by Hadi Mostafa Kadhim ALTALAB titled "ACTIVE CONTROL OF AIRCRAFT WING VIBRATION" is fully adequate in scope and quality as a thesis for the degree of Master of Science.

Assist. Prof. Dr. Mehmet BAKIRCI .....
Thesis Advisor, Department of Mechanical Engineering

This thesis is accepted by the examining committee with a unanimous vote in the Department of Mechanical Engineering as a Master of Science thesis. June 7, 2023

Examining Committee Members (Institutions)	Signature
Chairman : Prof. Dr. Bilge DEMİR (KBÜ)	.....
Member : Assist. Prof. Dr. Mehmet BAKIRCI (KBÜ)	.....
Member : Assoc. Prof. Dr. Fuat KARTAL (KÜ)	.....

The degree of Master of Science by the thesis submitted is approved by the Administrative Board of the Institute of Graduate Programs, Karabük University.

Prof. Dr. Müslüm KUZU .....
Director of the Institute of Graduate Programs

“I declare that all the information within this thesis has been gathered and presented in accordance with academic regulations and ethical principles and I have according to the requirements of these regulations and principles cited all those which do not originate in this work as well.”

Hadi Mostafa Kadhim ALTLABA

ABSTRACT

M. Sc. Thesis

ACTIVE VIBRATION CONTROL FOR AIRCRAFT EING

Hadi Mostafa Kadhim ALTALAB

Karabük University
Institute of Graduate the Programs
Department of Mechanical Engineering

Thesis Advisor:
Assist. Prof. Dr. Mehmet BAKIRCI
Assist. Prof. Dr. Moammed Jawad Mohammed AL JAWAD
June 2023, 107 pages

Aeroelastic instability resulting from vibration and harmful energy can significantly impact an aircraft's performance, stability, and safety, potentially leading to catastrophic failure. The annoyance caused by noise and the fatigue experienced by passengers due to vibration further highlights the importance of addressing this issue. This study applied an active management approach using the PID-PSO technique to mitigate vibration in a UAV's wing. Based on the NACA 2416 type, the wing was fabricated using a 3D printer with PLA material. Experimental tests were conducted at three speeds: 10, 15, and 20 m/s, and airspeed data was collected for each speed. These studies highlight the integration of modeling and control techniques to mitigate vibration in the UAV's wing. By accurately modeling the wing's behavior and applying the optimized control system, the mean squared error and vibration reduction ratio improved, leading to enhanced performance, increased safety, and a significant reduction in vibration levels. The wing's behavior was modeled using the neural network's method known as NN-NARX. The modeling process aimed to capture the

wing's response and predict the vibration accurately. The mean squared error (MSE) was calculated to evaluate the accuracy of the model, and the best MSE achieved for the modeling system was 0.0028 at 10 m/s, 0.000035217 at 15 m/s, and 0.00064992 at 20 m/s. Additionally, the active control process, implemented with the PID-PSO technique, effectively reduced vibration and improved performance. The control system's MSE was used to assess its effectiveness in minimizing vibration, with the best MSE achieved being 0.0092 at 10 m/s, 0.0668 at 15 m/s, and 0.0013 at 20 m/s. Moreover, the vibration reduction ratio was calculated to quantify the extent of vibration reduction achieved by the control system. The vibration reduction ratios obtained were 47.995% at 10 m/s, 44.837% at 15 m/s, and 44.812% at 20 m/s.

Key Words : PID controller, artificial neural network, active vibration control, system identification, wing aircraft.

Science Code : 91410

ÖZET

Yüksek Lisans Tezi

UÇAK KANADI İÇİN AKTİF TİTREŞİM KONTROLÜ

Hadı Mostafa Kadhım ALTALAB

Karabük Üniversitesi
Lisansüstü Eğitim Enstitüsü
Makine Mühendisliği Anabilim Dalı

Tez Danışmanı:
Dr. Öğr. Üyesi Mehmet BAKIRCI
Dr. Öğr. Üyesi Moammed Jawad Mohammed AL JAWAD
Haziran 2023, 107 sayfa

Titreşim ve zararlı enerjiden kaynaklanan aeroelastik kararsızlık, bir uçağın performansını, stabilitesini ve güvenliğini ciddi şekilde etkileyebilir ve felaketle sonuçlanabilir. Titreşimden kaynaklanan rahatsızlık ve yolcuların yaşadığı yorgunluk, bu sorunun ele alınmasının önemini vurgular. Bu çalışmada, bir İHA'nın kanadında titreşimi azaltmak için PID-PSO tekniği kullanılarak aktif bir yönetim yaklaşımı benimsendi. NACA 2416 tipine dayanarak kanat, PLA malzemesi kullanılarak 3D yazıcı ile üretildi. Deneyler, 10, 15 ve 20 m/s olmak üzere üç farklı hızda gerçekleştirildi ve her hız için hava hızı verileri toplandı. Bu çalışmalar, modelleme ve kontrol tekniklerinin entegrasyonunu vurgulayarak UAV kanadındaki titreşimi azaltmayı hedeflemektedir. Kanadın davranışını doğru bir şekilde modellemek ve optimize edilmiş kontrol sistemi uygulamak suretiyle ortalama karesel hata ve titreşim azaltma oranı iyileştirildi, bu da performansın artmasına, güvenliğin artmasına ve titreşim seviyelerinin önemli ölçüde azalmasına yol açtı.Kanadın davranışı, NN-

NARX olarak bilinen yapay sinir ağları yöntemi kullanılarak modellendi. Modelleme süreci, kanadın tepkisini yakalamayı ve titreşimi doğru bir şekilde tahmin etmeyi amaçlamaktadır. Modelin doğruluğunu değerlendirmek için ortalama karesel hata (MSE) hesaplandı ve modelleme sistemi için en iyi MSE değerleri, sırasıyla 10 m/s'de 0.0028, 15 m/s'de 0.000035217 ve 20 m/s'de 0.00064992 olarak elde edildi. Ayrıca, PID-PSO tekniği ile uygulanan aktif kontrol süreci, titreşimi etkin bir şekilde azalttı ve performansı iyileştirdi. Kontrol sisteminin MSE değeri, titreşimi en aza indirmedeki etkinliğini değerlendirmek için kullanıldı ve en iyi MSE değerleri sırasıyla 10 m/s'de 0.0092, 15 m/s'de 0.0668 ve 20 m/s'de 0.0013 olarak elde edildi. Ayrıca, kontrol sisteminin başardığı titreşim azaltma oranını belirlemek için titreşim azaltma oranı hesaplandı. Elde edilen titreşim azaltma oranları sırasıyla 10 m/s'de %47.995, 15 m/s'de %44.837 ve 20 m/s.

Anahtar Kelimeler : PID kontrolcüsü, yapay sinir ağı, aktif titreşim kontrolü, sistem tanımlama, kanatlı hava aracı.

Bilim Kodu **:** 91410

ACKNOWLEDGMENT

In the outset, I want to give because of Almighty (Allah S.W.T.), the most gracious and most merciful, for blessing me with the intelligence, motivation, and endurance to finish this study. We pray that Allah SWT showers his mercy and blessings on the last prophet, Mohammad S.A.W. To my supervisors, I offer my deepest gratitude and respect "Assist. Prof. Dr. Mehmet BAKIRCI " and "Assist. Prof. Dr. Mohammed jawad MOHAMMED " They are the ones who gave me their precious time and their sea of information and their extensive knowledge that proved invaluable to the research project, since I relied heavily on their direction and suggestions throughout the study, so I ask Allah Almighty to reward him with the best reward. Last but not least, my dear father, my generous mother, and my beloved wife, who were the first to support me in reaching what I have reached. as well as sibling and friend who assisted and contributed to the accomplishment of this thesis in any way, I'd want to single out my pal, Eng. Ghiath Yassin helped me tremendously with this project.

CONTENTS

Page

Page

Page

LIST OF FIGURES

Page

Page

Page

LIST OF TABLES

Page

LIST OF SYMBOLS AND ABBREVIATIONS

SYMBOLS

x_1, x_2, x_3	:	Actual input data neural network layers 1, 2 and 3
y_k	:	Actual output
y_1, y_2, y_3	:	Actual output data for neural network layers 1, 2 and 3
m_a	:	Added mass
A	:	Amplitude
b_1, b_2, b_3	:	Bias weights for neural layers 1, 2 and 3
$\Delta e(t)$	:	Change of error in continuous time
$\Delta e(k)$	:	Change of error in discrete time
$u(t)$	:	Controller output in continuous time form
$u(s)$	:	Controller output in Laplace transform and continuous
$Gz)$	:	Controller output in Laplace transform and discrete
m	:	Cylinder mass
C	:	Damping coefficient
$\zeta ratio$	:	Damping ratio
$A(z^{-1})$	:	Denominator of polynomials with associated
K_D	:	Derivative gain
y_d	:	Desired output
Γ_D	:	Differential learning parameter
C_d	:	Drag coefficient
$e(t)$	:	Error in continuous time
$e(k)$	:	Error in discrete time
ρ	:	Fluid density
U	:	free-stream velocity of fluid
R_k	:	Fuzzy control condition
$u(k)$	:	Input data

K_I	:	Integral gain
Ψ_I	:	Integral learning parameter
μ	:	Kinematic viscosity
lth	:	Layers
L	:	Length of cylinder
CL	:	Lift coefficient
F_L	:	Lift force
$m*$	:	Mass ratio
π	:	Mathematical constant equal to 3.1415
$\varepsilon(t)$	:	Mean square error
$x_{id}n+1$	:	New position
$v_{id}{}^{n+1}$	:	New velocity
f	:	Nonlinear function
N	:	Number of elements
$Bz^{-1})$	:	Numerator of polynomials with associated parameters
$y(k)$	:	Output data
$O_{l,i}$	:	Output for ANFIS layer
n_a	:	Past value
θ	:	Permeable plate angle
$\hat{y}(k)$	:	Predicted output
a_i, b_i, c_i	:	Premise parameters
K_P	:	Proportional gain
Φ_P	:	Proportional learning parameter
$rand( )$	:	Random function
U_r	:	Reduced velocity
Re	:	Reynolds number
k	:	Spring coefficient
S_t	:	Strouhal number
W	:	Swarm size
wij	:	The weights between the neural network layers
M_{total}	:	Total moving mass
P_I	:	Updated position

V_1 : Updated velocity

$\xi(k)$: Zero mean white noise

ABBREVIATIONS

AVC : Active vibration control

BF : Bacterial foraging

CC : Cohen Coon CCW - Counter-clockwise

CFD : Computational fluid dynamic

CHR : Chien-hrone-reswich method

CRBRP : Control rods beside the riser position

CRFBRP : Control rods in front-back the riser position

CW : Clockwise DAC - Digital to analogue converter

DAC : Digital to analogue converter

DAQ : Data acquisition system

DC : Direct current DE - Differential evolutionary

DFE : Dynamic Finite Element

DFT : Discrete Fourier transform

FEA : Finite Element Analysis

MSE : Mean square error

NACA : National Advisory Committee for Aeronautics

NAR : Nonlinear auto-regressive

NARX : Kind of nonlinear regression that takes in extra data from the outside

ND : Count of delays

NE : Number of hidden neuron

NN : Neural network

NN-NAR : Nonlinear auto-regressive neural networks

NN-NARX : Nonlinear auto-regressive neural network that takes in extraneous data (exogenous)

NN-NIO : Artificial neural network with nonlinear input-output

NNOE : Neural network based output error

P : Proportional

PC : Personal computer

PD	:	Proportional-derivative
PEM	:	Prediction error model
PI	:	PID Proportional-integral The Proportional-Integral-Derivative
PID	:	Proportional-Integral-Derivative
PIV	:	Particle image velocimetry
PSO	:	Particle swarm optimization
QEP	:	Quadratic eigenvalue problem
SI	:	System identification
VIV	:	Vortex induced vibration
ZE	:	Zero
ZN	:	Ziegler-Nichols

PART 1

INTRODUCTION

1.1. PREFACE

The vibration of a mechanical system is undesirable due to the system's structure's susceptibility to failure. It is crucial to safeguard the vibrating structure against collapse in order to avert catastrophic consequences, and even more so when the structure is going to be in human contact, the dynamic analysis of the wings is the most crucial since their performance is crucial for the overall safety of the aircraft. The dynamic stability of the aircraft's wings is an important design element. The primary purpose of a wing structure is to resist aerodynamic loads [1].

In structures, vibrations and dynamic chaos are undesirable phenomena. They cause disruption, discomfort, destruction, and damage to the system or structure [2].

Lifting surfaces for modern aircraft must be thinner, lighter, and more flexible to reduce weight and fuel consumption without sacrificing speed. Hence, aeroelasticity is essential in the development of lifting surfaces for airplanes. Deformation of an elastic body under aerodynamic loads, in a cross-flow is the primary focus of aeroelasticity. You may easily explore two or more interaction phenomena with just a few hours of work and a familiarity of dynamics, aerodynamics, and elasticity. Three types of interactions are given: structural dynamics, static aeroelasticity, and dynamical aeroelasticity. As the loads (aerodynamics) are highly dependent on the deformation (structural dynamics), and even the deformation (structural dynamics) depends on the loads, we may say that aeroelasticity is a linked problem. For the most part, static aeroelasticity is concerned with static instability (also known as divergence), while dynamic aeroelasticity is more concerned with flutter [3].

Flutter is one of the most severe cross-flow instabilities that aircraft wings and tails can exhibit. Integrated mode fluttering of aircraft wings can be correctly defined that used the two-mode approximations of kinematics and the flow rate estimate of the aerodynamic forces [4].

The construction of an aircraft wing must transfer and withstand loads. It is composed of thin shell constructions in order to withstand bending, compression, and twisting loads, the structure is supported with longitudinal stiffening components but also transverse frames. due to the aerodynamic effect, this sturdy construction generates unwanted vibration despite its durability [5].

Aeroelastic stability is a significant factor in aeronautical design, especially for aircraft with thin wings as well as a high aspect ratio. the first few free vibrational modes of an aircraft with a high aspect ratio are typically wing modes because, natural frequencies of the fuselage and tailplane is typically significantly higher. To achieve acceptable results, the free vibration and flutter analyses of wings take precedence over the cantilever boundary condition of the airfoil [6].

Other wing components are designed with a relatively high aspect ratio to generate adequate lift. Compared to the fuselage, the wing's bending and torsional stiffnesses are significantly lower. Obviously, the wings are considered the most vital and delicate components of an aircraft. this study focuses solely on the flutter and vibration study of free of aircraft wing surfaces. The wing can be considered cantilevered on the fuselage's side wall without sacrificing many generalities. Due to its non-coincident mass and shear center, it is typical for an aircraft wing's bending and torsional deformations to be coupled [6].

Vortex-induced vibration is a phenomenon that occurs when solid objects are placed directly in the path of a fluid vortex [7].

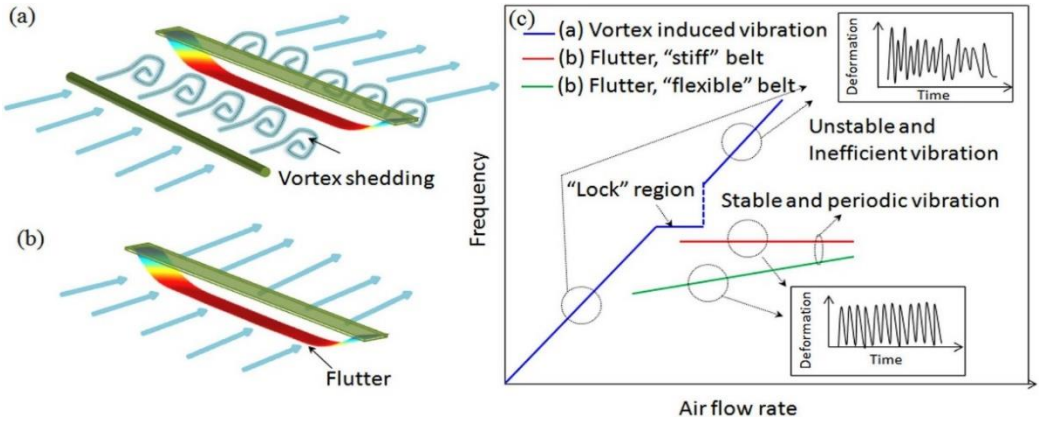

Figure 0.1. VIV is a significant cause of structural failure, particularly When the frequency of vortex shedding is the same as the frequency at which resonant transverse vibration occurs without the need for passive or active controls, the result is a strong [8] [9].

An adverse effect of VIV with strong amplitudes on the structure can be expected. Hence, preventative measures are required to eliminate or lessen their effects. The three main types of vortex suppression tools are: Instruments, both active and passive, and hybrids, Active control mechanisms utilize external energy to modify the circulation of fluids in the body. Whether it's a change to the body's surface or some additional hardware, passive devices can alter the fluid's flow around the body without any additional power. Compound devices combine the use of both active and passive [10].

In active control technology, gust load alleviation and flutter suppression methods are classified as contorollers of structural vibration. These vibration control methods are for practical uses according to the development of control technology [11].

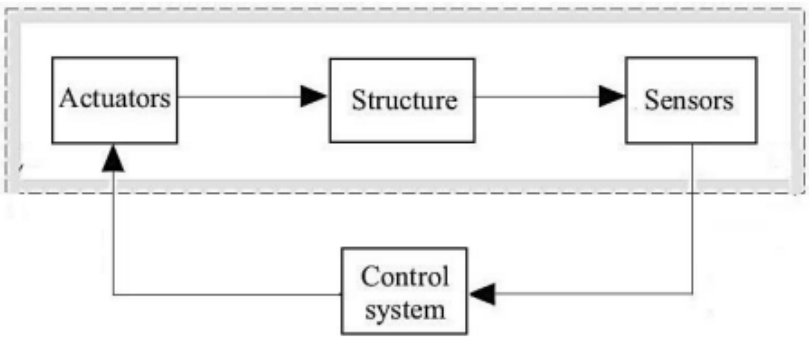

Figure 0.2. Using actuators and sensors, an active control approach provides a feedback signal [12].

1.2. PROBLEM STATEMENT

When vibration interacts with unstable aerodynamic forces, it can occasionally result in aeroelastic instability, such as a flutter. Flutter can compromise an aircraft's performance, stability, and safety, ultimately leading to its destruction. In addition to causing passenger discomfort, airplane vibration can also cause weariness and produce undesired noise. To maintain structural and vehicle safety, one must implement vibration control techniques. Thus, the design of vibration control systems for aircraft is crucial and must optimize structural factors such as size, mass, and volume. The cost of such systems determines whether or not they are installed on an aircraft.

Nevertheless, passive methods are not very effective for low-frequency band vibrations, which are commonly encountered in airplanes, helicopters, etc. AVC systems are consequently more suited in the frequency range of 0 to 500 Hz, which helps to limit the negative impacts of external disturbances. Reduced structural vibrations can result in increased fatigue life and flutter margin, ensuring the structural integrity of the aircraft. Often, these AVC systems are fashioned with both analog and digital filters [13], [14].

Active vibration control (AVC) systems are currently regarded as an unexplored field for innovative researchers due to the intricate dynamics, despite recent innovations in the AVC of flexible structures such as plates, and cylinders. First attempts at controlling the VIV via AVC were made by Williams and Baz; subsequently, the work on AVC became more advanced [15], [16].

The low consumption of energy by miniature devices such as DC motors has recently strengthened the advantages of the active control method. These small-sized devices are light in weight and give high performance via sensors and actuators. Therefore, AVC has captured the interest of researchers relative to passive control. AVC can also be implemented for complex systems designed by modeling and analysis [8].

1.3. RESEARCH OBJECTIVES

This concept intends to mitigate the influence of VIV on a segmented aircraft wing model utilizing conventional and intelligent control approaches inside a simulated AVC strategy environment. These were the aims of this thesis:

1. Modeling VIV systems employing nonlinear SI techniques such as neural network time series (NN-NARX) to forecast the dynamic reactions.
2. The purpose of this study is to develop a particle swarm optimization–based (PSO) active vibration control system for the Vortex induced vibration.
3. Investigation of the control units using various tuning techniques on the nonlinear models derived from the system determination (SI) techniques of the aircraft wing.
4. develop the best controller to suppress the attenuation of the undesired vibration on the aircraft wing system.

1.4. RESEARCH SCOPE

1. Development of a laboratory-scale experimental to withstand the vibration of a model aircraft wing, being built by a 3D printer, type in this model is NACA 2416, The wing will be printed into parts and then the body will be assembled. It can be printed using PLA material, the velocities in this study ranged from10 m/s to 20 m/s.
2. MATLAB program, along with integrating the flow measuring devices and data acquisition (DAQ) system, is utilized to get the data regarding vibrations.
3. Using nonlinear system identification (SI) methods such as neural network time series, the aircraft wing was modeled, the neural network time series consists of neural networks based on nonlinear auto-regressive external (exogenous) input (NN NARX).
4. The controller simulation by developing the typical PID controller using a particle swarm optimization method, in the VIV-affected wing. Discrete-time P, PI, PD, and PID controllers were developed on the aircraft wing under VIV.

1.5. RESEARCH SIGNIFICANCE AND MOTIVATION

Active vibration control is being used in airplanes in order to improve performance, expand the operational range, and reduce structural weight [17], [18].

Smart beams are commonly utilized for simulating the dynamics and studying the active vibration reduction potential in aviation wing surfaces. Many benefits are acquired with this method. The aircraft's stability and maneuverability, resistance to turbulence, passenger safety, and decreased fatigue damage are examples [17].

Damage to the wing's structural integrity isn't the only thing that flutter may ruin for an airplane; it also affects the plane's ability to take off and land safely and how well it flies., and energy economy. Thus, effective flutter avoidance methods are required for the certification of new aircraft [17].

1.6. RESEARCH CONTRIBUTIONS

1. Use a Nonlinear auto-regressive neural network that takes in extraneous data (NN-NARX)to model vibration in a wing and Predict emotional reactions.
2. The best controller was Developed to suppress vibration on the aircraft wing system by Improving a Proportional-Integral-Derivative.
3. Improve a Proportional-Integral-Derivative (PID) system by Particle swarm optimization (PSO) for vibrating in a wing Unmanned Aerial Vehicle.
4. Reduction of the influence of Vortex-induced vibration on an aircraft wing model utilizing the Active vibration control (AVC) strategy.

1.7. RESEARCH METHODOLOGY

The research methodology consisted of two main steps. Firstly, an extensive review of technical papers, journals, and books on Vortex-Induced Vibration (VIV) in Aircraft wing systems was conducted to identify key problems and establish a theoretical framework. This involved comparing active and passive control strategies within the context of VIV.

The second step involved designing and implementing an experimental setup for the Aircraft wing. The objective was to gather data on the input-output relationship, where the input parameter was the flow rate and the output parameter was the wing vibration or displacement. Appropriate devices and instruments, such as flow measurement tools and accelerometers, were utilized to achieve this. PSO-PID controllers were used in MATLAB software to simulate Active Vibration Control (AVC). This control unit is intended to dampen vibration in the wing. NARX predicted the vibration. The PID controller was tuned using particle swarm optimization (PSO).

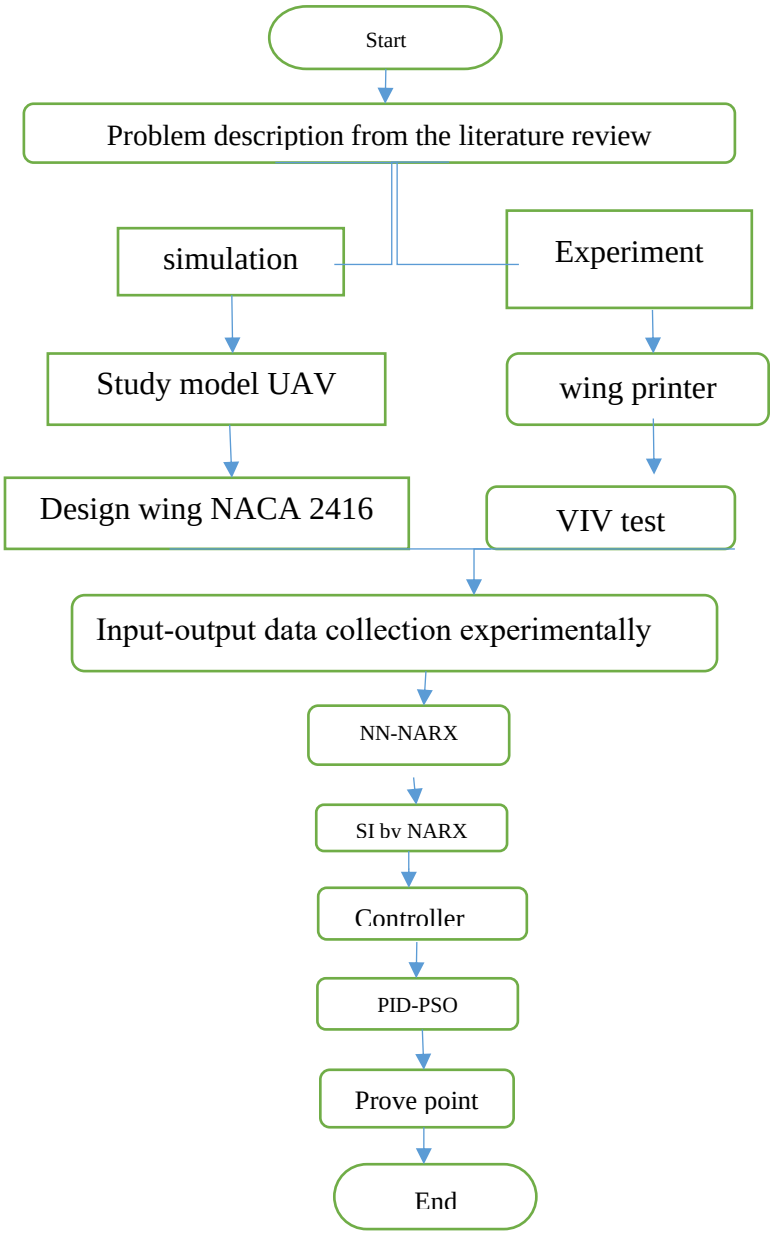

Figure 0.3. Research methodology flowchart.

1.8. THESIS ORGANIZATION

The following is a synopsis of the eight chapters that make up this thesis:

Chapter 1: The introduction, context, scope, research challenge, research motivation, and contributions are described. A flowchart illustrating the research technique.

Chapter 2: This chapter focuses on a literature review of the theory and foundations of vibration and VIV in aircraft wings. It also describes the techniques utilized to handle vibration utilizing AVC controllers. In various applications, the methodologies and performance of AVC on VIV, as well as the idea of employing neural networks to minimize vibration via controllers, have been addressed. In addition, research gaps are examined.

Chapter 3: The experiment involved using drone model with specific wing design and NACA for it and dimensions after that printed the wing. An air generator provided thrust, while sensors measured vibration levels. Fixed supports ensured stability, and connecting data transfer. Natural frequency and vibration amplitude were calculated, and MATLAB was used for data analysis and displaying realistic vibration results.

Chapter 4: presents the results of nonlinear SI techniques predict the dynamic reaction of the wing to VIV. The models were created using nonlinear SI as neural network time series. the time series of the neural network comprised of three unique kinds. Three types of nonlinear neural networks have been developed: those with non-linear auto-regressive external (exogenous) inputs (NN-NARX), nonlinear autoregressive (NN-NAR), and nonlinear input-output relationships (NN-IOR) (NN-NIO). (NN-NARX) model was selected and tested using the MSE validation method and correlation tests.

Chapter 5: describes the results of the simulation of AVC using modeling technique (NN-NARX). The controller settings were fine-tuned using particle swarm optimization (PSO). approach Iterative learning algorithm (ILA) was employed to enhance the P, PI, PD, and PID performance of the controllers.

Chapter 6: Findings and draws conclusions from one point of view. Suggestions are made for future studies on the control of Vortex induced vibration.

PART 2

SURVEY OF REVIEW

2.1. PREFACE

This chapter provides a summary of prior studies. Four main components comprised the literature review. The first section examines the vibration phenomena of an aircraft wing model through the lens of fundamental theory and describes how researchers approached the problem.

The second section presents the modeling of Vibration via SI techniques and other applications. The third section demonstrates how conventional and intelligent controllers suppress vibration and looks at applied controllers used in different applications.

Finally, the fourth section details both active and passive control methods to reduce the vibration on an aircraft wing and fill the existing research gaps.

2.2. VIBRATION ON THE AIRCRAFT WING

In this subsection, the theory and fundamentals of the vibration phenomenon on an aircraft wing are presented as expressed by the researchers [5].

In this study, Finite element an aircraft wing's dynamic behavior can be calculated with the help of analysis. ACAD model of the wing is created, including the aerofoil, the associated engine, and the winglet's specifics. Detailed frequency study in the region of 0-300 Hz is performed on the wing in relation to maximum displacement and VON MISES stress by [1].

Using the CALFUN program (Computation of flutter speed using normal modes), we analyzed the free vibration and flutter of wings with a high aspect ratio. In this study, we used CALFUN data to determine that torsional rigidity (GJ) does have a bigger influence on flutter speed than bending rigidity (EI), with GJ having an effect on flutter speed of at least 9% for all three aircraft, while EI had an effect of less than 0.7% [19].

Using the dynamic stiffness approach, natural frequencies and modes of shapes to the wings are determined, the results of computing the first six natural frequencies and modes of shapes are examined and contrasted. After modal analysis, a flutter analysis is conducted using the normal mode approach in combination with generalized coordinates and theodorsen's two-dimensional unstable aerodynamic theory. Four aircraft's flutter speeds and flutter frequencies are determined [6].

A control system utilizing an electric actuator of the eccentric mass type and equipped with damping properties is proposed as a solution to the non-fixed-wing aircraft vibration problem. Experiments show that the actuator resultant force amplitude error is less than 5%, a frequency error is less of about 0.5%, and even the step steady-state accuracy is even less than 5%; the dynamic settling time required for quite a phase change of 30 does not exceed 0.1s, as well as the phase steady-state accuracy is less than 5%. This information is used to analyze the effect of gear authorization on the steady-state and dynamic effectiveness of the active vibration control system [20].

Aircraft wing dynamics can be modeled with smart beams, and active vibration reduction solutions can be studied. As a result of using this method, an transfer function of a linear system in continuous time has been calculated. Finally, the smallest realization shapes for the resulting function were identified. This was made possible by employing a method predicated on the concept of one-dimensional digraphs[17].

Here, we offer an approach to measuring flutter velocity and exploring aeroelastic reactions by constructing a flutter mechanism for use in a subsonic wind tunnel. The experimental setup is tailored to permit the most wiggle room in all parameters depending on this double mathematical model. The bending stiffness and torsion stiffness of the first mode are calculated with ANSYS. Research shows that the UAV

encounters flutter around 240 m/s (466 knots). This speed greatly exceeds its maximum potential. Hence, this UAV wing can flutter at its maximum speed without being severely compromised [21].

Of this article, we looked at the NACA 0012 airfoil with high attack angles, where the vortex can form and shed predictably in the downstream direction. By utilizing test data from the references, the VIV was numerically analyzed and validated. The vortex-shedding mechanism was shown to be relatively unaffected by the ratio of frequencies, amplitudes of vibrations, or direction of entering flow. The phase of airfoil vibration plus vortex shedding varies in the V-lock-in zone as a function of frequency ratio. This is due to the fact that the phase In addition intensity of vortex shedding are almost constant with the vibration amplitude when the frequency ratio is one. To investigate the mechanisms of VIV in regard to energy balance, a method is given based on the features of vortex shedding for separating the disturbances generated between airfoil vibrations and vortex shedding [22].

experimental investigation with a movable NACA 0021 airfoil, they measured the VIV response at $0^{\circ} \leq \alpha \leq 180^{\circ}$. Because it is used in VAWT (Vertical-Axis Wind Turbine) designs, this airfoil is worthy of consideration. The experimental results of this investigation show that oscillations occur at attack angles around sixty and one hundred thirty degrees. Since the full-scale velocity reduction predictions are consistent with the measured VIV, VAWTs [23].

Based on the VIV phenomenon, the force that develops behind the structure is split into two types, lift and drag forces, based on direction of the force. the drag force flows parallel to or in line with the free-stream fluid flow, whereas, a force of lift moves perpendicular or in a transverse vibration, the lift coefficient is provided by [24]:

$$\mathrm{C_L} = \frac{L}{0.5\rho\, \mathrm{A_c U^2}}\,\mathrm{s} \tag{0.1}$$

$$C_D = \frac{D}{0.5 * A * V^2} \tag{0.2}$$

Eq 2.1: L represents the lift force, represents the fluid density, Ac represents the body's characteristic area, furthermore U represents free-flowing speed. The lift coefficient, which is equivalent to St, also depends on Re. The lift coefficient was experimentally determined and in Eq 2.2: Cd drag coefficient, D drag force, ρ is the density, V is the velocity, A is the reference. by Norberg by [24].

Table 0.1. Vibration phenomenon in the literature review**.**

Author	Plant	Type of study	Type of vibration
Norberg (2001)	Cylinder	Effects of reynolds number	VIV
Banerjee (2013)	Aircraft wings	Characteristics of aspect ratio	Free vibration and flutter
Mohammed (2017)	Wing	Analysis of high aspect ratio	Analysis free vibration and, flutter
Markowski (2017)	Aircraft wings	Active vibration	Free vibration and flutter
Babar (2019)	NACA 2415 Wing	Experimental Analysis	Flutter
Benner (2019)	NACA 0021 Airfoil	Investigate Its (VIV) Response At Varying Angles Of Attack	VIV
Hao (2020)	Main spiral blade of non-fixed wing	Vibration-damping electric actuator control	Produce periodic vibration force
Basutkar (2020)	Wing	Analysis	Force Vibration
Han (2021)	Airfoil NACA 0012	Method of separating disturbances	VIV

2.3. VIBRATION CONTROL APPROACHES

It was suggested that many different ways may be used to significantly lessen or get rid of these vibrations. In this paper, the authors use piezoelectric transducers (PZT) mounted on the model's outer skin as actuators to explore the feasibility of applying the velocity feedback method (VF) to the control of an aircraft wing. ANSYS.16 was used to run simulations of the entire wing. High degrees of response augmentation was achieved with a gain of 1.2, where the settling time of the controlled wing was reduced to 55% of its settling time when free vibrated.by [25].

Namic Aeroelastic response and active/passive aeroelastic control of modern aircraft wings are systematically explored using a model in which the wings are modeled as thin-walled beams. The current work builds off of the thin-walled beam model and refines it by include other non-classical factors that are often also important; the model is then tested against the available experimental, FEA, DFE, and other analytical predictions by [26].

In this laboratory, the importance of aircraft vibration testing is explored by determining the "undamped natural frequency", ω_u, as well as corresponding damping-ratio, ζ, of a lumped-mass aircraft model. The first mode resonant frequency is then used to evaluate the corresponding mode shape. Improvements can be made by increasing the number of measurements near the resonant frequency. Non-linear behavior could be estimated using the POD (Proper Orthogonal Decomposition) method by [27].

Parametric design (APDL) of ANSYS and placed into a finite element method. The use of a piezoelectric shaker for forced vibration control allows for the consideration of harmonic excitation (sin wave), the results of which were found to be in good agreement with those obtained using APDL ANSYS. Force vibration displacement amplitude while the control is off is 0.04 m and when it is on it is 0.0005 m [5].

Aircraft wing dynamics & active vibration suppression options are commonly investigated with the use of the smart beam. Two types of controllers Fractional Order Proportional Derivative and Linear Quadratic Regulator are discussed. Vibrations were dampened using piezoelectric patches in an experiment using an intelligent beam to investigate active vibration control approaches. This paper's study provides a necessary foundation for tailoring an improved fractional-order Square Root of a Linear Function by [28].

Vibration of just an aircraft wing subjected to various excitation forces is addressed, and the corresponding fact the main of (non-linear differential equations) is solved using the approach of multiple-scale perturbation. There are two primary methods employed. Both active and passive ways of regulation exist. We consider the identical

system with only a 1:2 internal resonance controller and with a tuned mass absorber applied at synchronous primary resonance (passive control) (active control). Its stability is obtained and investigated by using frequency response functions, and the analytical solution is developed up to the fourth-order approximation [29].

Table 0.2. Literature review for vibration control system modeling.

Authors	Type of modeling	Type of study	Controller method
Qin (2001)	Finite element analysis	Simulation	Piezoelectric material technology
El-Serafi (2006)	Non-linear dynamical	Mathematical study	Non_linear differential equation representing
Abdulameer (2015)	ANSYS APDL	Simulation	Smart structure technology is
Kane (2016)	Comparative analysis	Experiment	Quadratic regulator and fractional order proportional
Ali (2016)	ANSYS.16 software	Simulation	Velocity feedback [VF]
Pinho (2020)	Testing	Experiment	Used to the resonant frequency is to evaluate the corresponding mode shape

2.4. NEURAL NETWORK SYSTEM IDENTIFICATION

One of the greatest difficulties in the control in analytical domains is ensuring the accuracy of mathematical models. The controller's effectiveness may be constrained by the quality of the model used in its construction. There have been a variety of approaches used in the past to accomplish this goal. Among these methods is physical-based modeling, which is based on obtaining the (input/output) properties of the system analytically. ,some argue that the conclusions do not reliably correlate with the observed reaction of the actual system and that the process as a whole is too sophisticated to be practical. SI has rapidly become one of the most promising technologies for diagnosing machine failures and keeping track of their status in the manufacturing sector. SI is the study of the mathematical connections between a physical system's inputs and outputs as it performs in real time. Modeling, controlling (via dynamic specification of control), and forecasting is all possible with SI (prediction of commodities and expectation of energy load). as a result, a mathematical

model can be constructed directly from measurable input/output data from the system, thus recreating the observed behavior. Collecting high-quality input/output data, determining the best model within system category, furthermore evaluating the model's attributes are the three main components of SI [30].

Patil et al. investigated and contrasted numerous Si models, including AR, ARX, ARMA, & "NN-NARX" [31]. These models were utilized to foretell what the air temperature, solar radiation, and humidity would be like in a tropical greenhouse. The outcomes demonstrated that the "NN-NARX" models were superior to the alternatives. A paper on the dynamic modeling of a horizontally moving two-rotor, multiple-system was presented [32]. Parametric linear analysis and neural networks (NN) were used to examine the modeling of a horizontally moving two-rotor, multiple-system (TRMS), in order to simulate how TRMS operates, two SI methods, two distinct neural networks, the recursive least square (RLS) and the multi-layer perceptron (MLP-NN), were built. Results from numerous statistical tests, such as mean square error (MSE), one step ahead (OSA) prediction, and correlation tests, were utilized to validate both approaches. the results showed that SI might be used to model unconventional aircraft setups like a (TRMS) system.

For uncontrolled buildings, Gómez Pizano compared NN-NARX to neural network output error models for MISO and SISO systems [33]. Both acceleration and force were fed into the system, with acceleration serving as the output. Each set of results demonstrated that the NN-NARX model outperformed its counterpart, the neural network based output error model (NNOE).

During their VIV study, Shaharuddin and Mat Darus used SI units for an elastically supported rigid cylinder in a single direction .[34]–[36] When subjected to free flow, the cylinder could only wobble in a direction perpendicular to that of the flow, the dynamic behavior of VIV was predicted using both the recursive least square (RLS) also and adaptive neural fuzzy inference system (ANFIS) models that were constructed. The results showed that compared to RLS, ANFIS provided the most accurate model of the system.

Mohammed utilized the NN-NARX model to estimate solar radiation on an hourly basis using different training procedures and checked the accuracy of his predictions using the root mean square error (RMSE) statistic [37]. Data comparison revealed that the NN NARX model successfully determined the connection between input and output variables, allowing for precise prediction of solar radiation hours.

Tahseen used the ANFIS technique to make predictions about the pressure drop and heat transfer in a flat tube operating at the cross-flow direction in real time. The prediction algorithm took into account transverse pitch, longitudinal pitch, and Re as inputs [38]. This study demonstrates that the ANFIS technique is useful in engineering since it provides accurate predictions of the system's output.

Using an exogenous input time-varying autoregressive (TVARX) model, Yazid et al. determined the transfer function response for an offshore structure [39] At first, the wave motion was created with the use of a discrete Fourier transform (DFT). The TVARX coefficient was determined using the Kalman smoother algorithm, which is a mix of a Kalman filter and an expectation-maximization (EM) algorithm. Furthermore, transfer function was created using the least mean square (LMS) also restricted least squares (RLS). According to the findings, the transfer function generated by the TVARX model was reliable, with low levels of noise. A solar collector's temperature efficiency was predicted using two NN models developed [40].

In order to model an electro-hydraulic actuator (EHA) system, YLing et al. used the ANFIS method, taking information from the experimental setup and verifying it using root-mean-squared error [41]. It was determined that best results were obtained from the ANFIS model. From response performance for complex nonlinear systems. how well a solar collector works in terms of temperature efficiency.

Using a variation of the Neural Network with Nonlinear Inputs and Outputs with Auto-Regressive Learning, Mohammed et al. and Mat Darus created a Neural Network (NAR) with external (exogenous) input. A heuristic-based discrete-time proportional-integral-derivative (PID) controller. Lastly, evidence was provided that NARX is

superior to other approaches in representing VIV on the pipe riser in terms of MSE [42].

Partial differential equations (PDEs) also multiple ordinary to differential equations were used to model of dynamic behavior to a flexible wing, which was investigated by Gao, S. (ODES). Existing control approaches for similar PDE systems are fine in most cases, but following control input quantization, they can lead to sloppy behavior and even stability losses. An adaptive quantitative control strategy using a radial basis function (RBF) neural network is suggested to reduce to wing's elastic deformation following input quantization. [43].

Table 0.3. SI from the literature review.

Author	SI type	Application	Algorithm	Remark
Mat Darus and Lokaman, 2010	Linear and nonlinear	Tropical greenhouse temperature	AR, ARX, ARMA and NARX	NARX performance was the best
Gómez Pizano (2011)	Linear and nonlinear	TRMS	(RLS-ARX NN-NARX)	(MLP-NN) Performance better than RLS
Shaharuddin and Mat Darus, (2012)	Linear	VIV	(LS-ARX RLS-ARX)	RLS performance better than LS
Shaharuddin and Mat Darus (2013a)	Linear	VIV	LS and RLS	RLS performance better than LS
Shaharuddin and Mat Darus, (2013b)	Linear and nonlinear	VIV	RLS and ANFIS	ANFIS performance better than RLS
Mohammed (2013)	Nonlinear	Solar radiation	ANFIS	Excellent for heat transfer prediction
Tahseen (2013)	Nonlinear	Heat transfer	ANFIS	Excellent for heat transfer prediction
Yazid (2013)	Linear	Sea waves	RLS-ARX	RLS-ARX accurate performance
Hamdan (2013)	Nonlinear	Solar radiation	NNEL and NN-NARX	NN-NARX performance better than NNEL
Ling 2014	Nonlinear	Electro_hydraulic actuator	ANFIS	Excellent for prediction
Radzakrishnan, (2014)	Linear	VIV	PEM and GA	GA performance better than PEM
Mohammed (2014)	Nonlinear	VIV	NN-NARX	Neural Network (NARX) based on the Nonlinear Auto- Regressive
Gao (2020)	Linear	Flexible wing	RBF	Radial basis function (RBF)neuralnetwork is proposed

2.5. ACTIVE VIBRATION CONTROL

In this application, few intelligent controllers were employed to reduce vibration. therefore, this subsection presents t PID controllers in, other applications with a focus on PID controllers on aircraft. a wide variety of models, including beams, plates, and cylinders, have been controlled using classical or traditional linear controllers like PID controllers. One of the benefits of these approaches is that they can handle a wide range of variables and loads, while also being dependent on controller gains on operating conditions [44].

Three different tuning methods for a PID controller were utilized by Aishwarya et al. to maintain consistent engine thrust [45]. To tune the engine, we used the Ziegler-Nichols (ZN) approach, a heuristic method that builds on the ZN method by employing the filters coefficient (1/1+N) in place of the derivative parameter in the PID equation, and eventually, a linearized method that relies on utilizing alternative engine speed models. As opposed to the complex nonlinear system used by the engine model in the previous tuning approaches, this one worked on such a linear system. Based on the findings, the heuristic approach clearly outperformed the alternatives. controller's simplicity and ease of learning are offset by the difficulty of gains tweaking [46]. Many methods, including, genetic algorithm (GA), particle swarm optimization (PSO), and differential evolutionary (DE), have been attempted and found to be effective in overcoming these obstacles and obtaining optimal values for PID parameters 34 [30]. The Ziegler-Nichols (ZN) approach was compared to the performance of a PID system controller for an DC Electric motor model by [47]. In order to decrease the fitness value, PSO used four different evaluation strategies. There were the IAE, ISE, ITSE, and ITE (ITAE). When compared to the ZN method, the PSO approach was found to produce better outcomes in terms of identifying the optimal response feature. the technique was far superior to its rivals.

For DC motor speed control, they used both traditional and smart optimization tuning strategies, then compared their results [48] PSO, GA, ant colony optimization (ACO), & evolutionary programming (EP) were all used for intelligent optimization tuning. Historically, Cohen Coon (CC) and (ZN) tuning methods made up the standard

repertoire. The standardization of Evaluation (ISE) Method is the determining factor in the evaluation criteria. The PSO approach achieved a decreased ISE, and the performance for intelligent optimizations was superior to that of traditional tunings. Furthermore, the PSO showed a faster settling time and the ACO a faster rise time. Yatim and Mat Darus compared use of self-tuning proportional-integral-derivative (PID) and proportional-integral-polar-sine (PID-PSO) controllers on the flexible manipulator for regulate hub angle and endpoint displacement response [49].

Using (RLS) as a SI approach, we developed the model, then we used MSE to analyze every system. Results showed that the (PID-PSO) controller was the most effective at regulating the position of the movable link and dampening vibration at the end point.by using PSO, bacterial foraging (BF), Ibrahim et al. tuned PID parameters for DC motor speed control. PSO outperformed BF in every metric [50].

Both Vishal and Jyoti hold the position of GA. When designing an airplane, engineers develop both linear quadratic regulator (LQR) and proportional integral derivative (PID) controllers for the pitch system. The parameters of the LQR and PID controllers are optimized with the aid of a genetic algorithm (GA). A mathematical model taking into consideration the longitudinal motion of an airplane is the starting point for the controller's design. the step's response is a representation of the results of a MATLAB simulation of the pitch angle response of an airplane. Both the LQR and PID controllers have tunable settings [51].

In Stability Enhancement of Commercial Boeing Aircraft with Integration of PID Controller modeling of a commercial Boeing aircraft control system (BACS) and PID controller employed to improve BACS stability. UrRehman 2021 The authors of Stability Improvement of Commercial Boeing Aircraft modeled that Boeing Aircraft Control System (BACS) with a PID controller in an effort to improve BACS stability. Because they produce best results, these strategies are used on closed-loop systems. The state space models and controller construction procedures are developed in MATLAB (R2021a). The results suggest that PID can be used to successfully counteract the framework's disruptive forces. Time domain specifications are used to assess the control system design's efficacy. We zeroed in on the stability pivot, where

we stressed the importance of a quick and smooth framework settle. Comparison of PID-controlled and uncontrolled state-space modal results [52].

Harris hawks optimization (HHO), is a revolutionary meta-heuristic technique designed to find the best values for the PID controller used in an airplane's pitch control. For the purpose of validating the efficacy of the HHO-tuned PID controller, we selected to compare it to other, more modern, and successful algorithm meta-heuristic, based on the PID controllers, such as automated search optimization (ASO) and tuning the salp swarm algorithm, Controllers based on a PID algorithm with fine-tuned tuning. Keeping track of an airplane's pitch angle with an HHO-tuned PID controller is the subject of a recent proposal. has been shown to outperform alternative techniques. Given the importance of the pitch angle to the aircraft's safe operation in flight, Through this study, a novel control strategy built on the HHO algorithm has emerged [53].

In Table 2.3, we get a rundown of how researchers have used simulation to fine-tune PID controllers using both conventional and artificially intelligent optimization techniques.

Table 0.4. Active vibration control by PID controller.

Author	PID tuning methods	Application	Simulation /Experiment	Remarks
Solihin (2011)	ZN and PSO	DC motor	Simulation	PID-PSO was the best
Nagaraj and Murugananth, (2011)	ZN, CC, PSO, GA, AC and EP	DC motor	Simulation	PSO recorded lowest ISE for other optimizations
Yatim and Mat Darus, (2014)	PSO	Flexible manipulator	Simulation	PID-ZN succeeded for vibration control
Ibrahim (2014)	PSO and BF	DC motor	Simulation	PSO efficiency was the best on PID
Vishal (2015)	LQR and PID	Aircraft	Simulation	Can be developed and applied to control
Izci (2020)	ASO and SSA	Aircraft	Statistical analysis	Improves the stability control system
UrRehman (2021)	(BACS) and PID	Aircraft	Simulation	Which is the best-proposed solution

2.6. RESEARCH GAPS

Previous research used AVC controllers experimentally to control unwanted vibration in an aircraft wing, but no attempt was made to control aircraft wing undergoing VIV using traditional and intelligent controllers experimentally. SI techniques have been applied in many applications for modeling linear and nonlinear systems. However, nonlinear SI methods for aircraft wing systems are still limited in the literature. The literature review uncovered one paper that studied (PDEs) , (ODES) are used to model the dynamic characteristics of the bendy wing. A control adaptive-quantitative strategy using a Radial basis functions (RBFs) neural-network is suggested to reduce the wing's elastic deformation following input quantization [43].

Thus, in this research, nonlinear SI via neural networks depended on dependent with respect to exogenous non-linear autoregressive inputs (NN-NARX), model was utilized to represent the dynamic response, as nonlinear SI was proven previously to be better than the linear SI techniques.

The control of the models via traditional and intelligent controllers has been implemented experimentally in many different applications. However, using traditional and intelligent controllers to mitigate the undesired vibration on aircraft wings has not yet been applied; furthermore, previous research used traditional and intelligent controllers on linear SI models (LS and RLS), even though the system was nonlinear. Also, one previous paper used ILA to tune a classical PID controller. No attempt was recorded to use another optimization method, such as PSO, which proved effective in many applications besides traditional optimizations. Thus, classical (PID) controllers were simulated on a nonlinear SI model (NN-NARX) to control the unwanted vibration on an aircraft wing in addition to using traditional (heuristic) and intelligent (PSO) optimization approaches on the PID controller.

PART 3

ANALYTICAI AND EXPERIMENTAL SET-UP

3.1. PREFACE

This chapter represents the design and improvement of the analytical and experimental setup for an Aircraft wing model under Vibrations. The data collection process was done by the necessary instrumentation such accelerometer and sensor of flow rate, and other devices. The results of the decay test, which may be used to determine the natural frequency and vibration at different velocities, are also presented in this chapter.

3.2. MODEL OF AIRCRAFT

Eclipson Airplanes has created a printed flying-wing airplane called the EWW180. In order to propel itself, it utilizes a specialized electric ducted fan (EDF). 3D-printable remote-controlled airplane part of a line of designs released by Eclipson. As its name suggests, the EWW180 has a wingspan of roughly 1.8 meters (180 cm). The airframe is optimized for stability and responsiveness, making it flexible enough to accommodate many pilot preferences and mission requirements. loading the wing 28 g/m^2 electric ducted fan (EDF) is 40 g/m^2, the ideal for propelling it . Information on how to choose an EDF unit, motor, and battery configuration that will achieve the desired performance and flight characteristics is provided on the website. NACA 2416 wings are airfoils. surface area of wing 30 dm^2 angle of attack ten degrees.

In Figure 3.1, the final image of the UAV aircraft is depicted after undergoing a series of modifications. It is worth mentioning that the focus of this study was specifically on the wing of the UAV aircraft, and it was utilized without incorporating a winglet. Also, see the clip he took from her for work.

Figure 0.1. Model of UVA [54].

3.3. AIRCRAFT WING MODEL

NACA 2416 is an airfoil design developed by the National Advisory Committee for Aeronautics (NACA), a precursor to NASA, in the early 20th century. This airfoil profile is widely used in various aircraft applications and has several advantages, including its versatility, speed capabilities, efficiency, and aerodynamic capacity. While primarily designed the NACA 2416 airfoil is most effective in the low-to-moderate speed range. The NACA 2416 airfoil provides a good lift-to-drag ratio, meaning it generates a significant ability to resist vibration and the strength of the wing structure at aerodynamic turbulence In our experiment, we investigated the performance and behavior of a drone wing utilizing the NACA 2416 airfoil. The wing had a root chord of 23.6 cm, a tip chord of 9.2 cm, and a wingspan of 75.2 cm. We conducted tests at three different speeds: 10 m/s, 15 m/s, and 20 m/s, in order to evaluate the wing's characteristics across a range of velocities. Comparing our range of velocity to the general knowledge about the NACA 2416 airfoil, we can affirm that our velocity with its expected characteristics.

In figure 3.2 The aileron type in this model is NACA 2416 ,to study the wing design and its dimensions and Solve the problem.

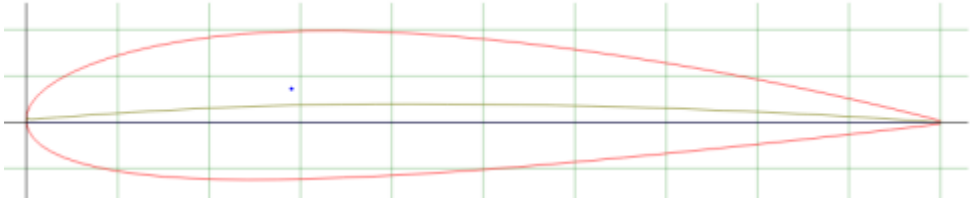

Figure 0.2. NACA 2416 [55].

Calculate area for trapezoidal wing:

$$A = 0.5*S*[CT + CR] \quad (0.1)$$

Where, S=span, CT= tip chord, CR= root chord, A= erea.

Table 3.1 The cantilever wing dimensions table presents a concise overview of the wing's structural parameters.

Table 0.1. Cantilever wing dimensions.

NACA 2416	
Root chord	23.6 cm
Tip chord	9.2 cm
Wing span	75.2 cm

A= (23.6+9.2)*0.5*75.2

A= 1233.28cm^2

A= 0.1233m^2

Aspect ratio

$$AR = \frac{S^2}{A} \quad (0.2)$$

$$AR=\frac{\mathbf{0.75^2}}{\mathbf{0.1233}} \quad (0.3)$$

AR= 4.5

When A chord Taper, ratio can be defined, as the ratio of its tip chord to its root. chord.

$$\mathrm{TA} = \frac{\mathbf{CT}}{\mathbf{CR}} \qquad (0.4)$$

$$\mathrm{TA} = \frac{\mathbf{0.236}}{\mathbf{0.92}}$$

$$\mathrm{TA} = 0.25$$

(Mean aerodynamic chord)

$$\bar{C} = S/b \qquad (0.5)$$

$$\bar{\mathrm{C}} = \frac{\text{wing area}}{\text{span}}$$

$$\bar{C} = \frac{0.1233}{0.75}$$

$$\overline{\boldsymbol{C}} = 0.1644$$

This table 3.2 presents subtractive wing information properties, including wing, type model, Aspect Ratio, mean chord, taper ratio, thickness wing and area wing.

Table 0.2. Specification of aircraft wing.

Aspect Ratio	**4.5**
Mean Chord	0.1644
Taper Ratio Average	0.25
Thickness wall (mm)	5
Wing Area m^2	0.1233
Wing Span m	0.75
Wing type model	Trapezoidal

Figure 3.3 showcases the wing's shape along with various dimensions, presenting a finalized design created using the Solidworks program. The wing shall be hollow and the thickness of the wall shall be 5 mm.

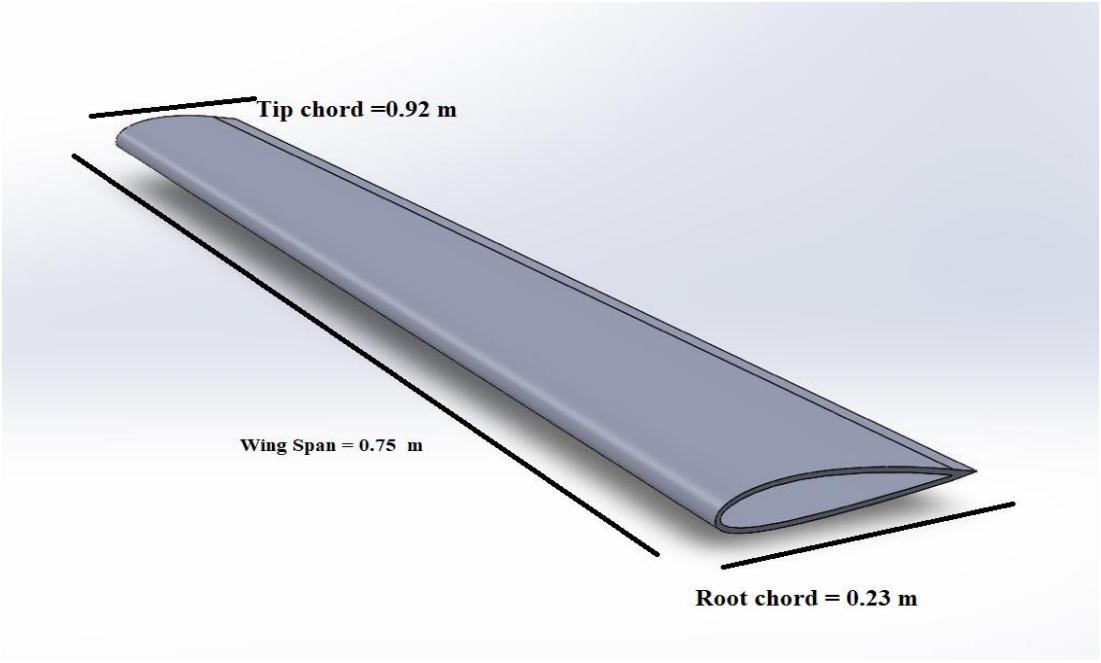

Figure 0.3. Geometry of the wing.

3.4. EXPERIMENTAL SET-UP

3.4.1. 3D Printing of an Aircraft Wing

After determining the dimensions of the wing and finalizing the designs in SolidWorks, we used an Ender 3 3D printer to print the wing in four parts. Each part took 14 hours to print and required a plastic wire reel and glue to assemble. We then sanded the wing using sandpaper starting from 60 degrees, moving up to 80 degrees, 180 degrees, and 360 degrees to achieve a smooth surface. After sanding, we applied car putty to eliminate any pores on the surface, followed by water-based sandpaper to fill any remaining fine pores. We then applied primer paint to the wing and finally painted it with rust oleum in gray.

In the second stage of the project, we designed and printed a carrier or holder for the wing. The holder is shaped like a wing on the inside and contains six screw holes. We made the holder using two parts.

In Table 0.3 material properties table presents a comprehensive and scholarly analysis of the critical properties of the PLA material.

Table 0.3. material properties

Density	**1.24** $\frac{g}{cm^3}$
Material	Polylactic (PLA)
modulus of elasticity	3.5 GPa
Poisson's ratio	0.3

The printing procedure is broken down into individual stages and explained in Figure 3.4. After printing, the parts are put together and given a final polish with sandpaper. There are pictures showing the four different grits of sandpaper that were used, the glue used to glue the pieces together, the dye used to color the parts, and the completed wing. This in-depth talk analyses the post-printing processes necessary for a polished and aesthetically pleasing wing structure. In Figure 3.5 the holder was designed in the CAD software Solidworks and then printed in two pieces via a multi-step process that involved stacking the material. This method of building, which is accomplished in stages, ensures accuracy and permits the incorporation of the intricate wing and fixed wood structural components.

Figure 0.4. 3D Printing of an Aircraft Wing.

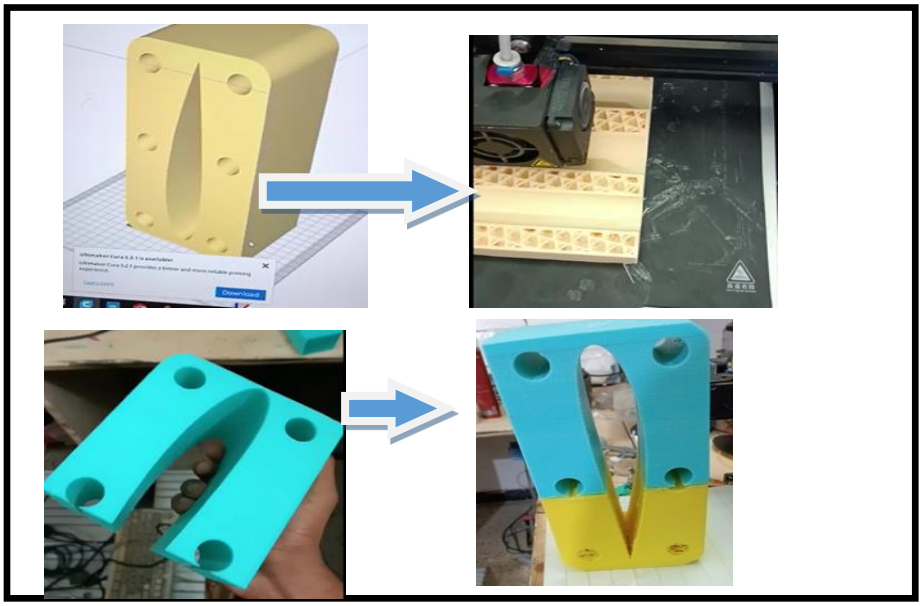

Figure 0.5. 3D Printing of holder.

3.4.2. Experiment

In the Electromechanical Laboratory at the University of Technology in Baghdad, we studied the vibration caused by liquid passing over the surface of a solid plastic wing. In this experiment, Anemometer was used to determine the velocity of the air passing over the wing. In addition, Pitot static tube was used to determine the velocity of the air at the point of calculating the vibration caused by the vortices air. Data logger Arduino (Nano) is used to transmit information from the Pitot static tube air speed sensor to the computer, while Data logger Arduino (MEGA) is employed to transmit information from the accelerometer.

Moreover We control the velocity of the air coming out of a centrifugal fan by inverter increasing or decreasing the frequency of the electric current as well as Fix the wing with a fixed support made of wood and connect with it using a part made of plastic, wing natural frequency and the vibration caused by the passage of the fluid at three different speeds were calculated .

In the first section for the cases of experiment was conducted on speed 10 m/s and the results showed 300 readings from , Pitot static tube , it represents the air speed at this point , and a similar one from a sensor Accelerometer , this represents the vibration on the wing at speed 10 m/s equals 36 km/h . In the second phase of this project, the air velocity coming out of Centrifugal fan was increased by increasing the frequency of the current arriving at the mechanism, to calculate the vibration on the wing at 15 m/s and equals 54 km/h. In the last section of this experiment, we recorded the readings at a speed 20 m/s equals 72 km/h of Accelerometer and Pitot static tube , The results were as final a portion in this chapter.

3.4.3. Experiment Components

A number of different parts and various materials were used to ensure that the experiment was carried out correctly and accurately. We will explain each of these parts and explain its use and function in the study. Detailed and comprehensive details will be provided in Appendix B of Study, where each part and material will be

discussed separately and important information and techniques used in its preparation and use will be clarified:

1. Anemometer Proskit (MT-4615)
2. Arduino (MEGA)
3. Arduino (NANO)
4. Centrifugal Fan
5. Clamp
6. Connecting Wires
7. Diffuser
8. Fixed Support From Wood
9. Holder
10. Interface MPU6050 Accelerometer
11. Inverter
12. Pitot Static Tube
13. Plastic Wing Stem Stabilizer
14. Solder Machine

In Table 3.4 the characteristics of the centrifugal fan that was used in the study. Furthermore, the wattage required to power it. centrifugal fan's power needs.

Table 0.4. The Centrifugal Fan DF-5 Properties.

TYPE	**DF-5**
Power	550 W
Volt	220 V
Flow rate	850 m/h
Pressure	1020 pa
Frequency	50 Hz

Figure 3.6, the essential parts of the experiment are depicted in this all-inclusive photo. The wing is fixed in place and pointed toward the air source, where it receives a controlled airflow. The image also draws attention to the wing's effective air distribution.

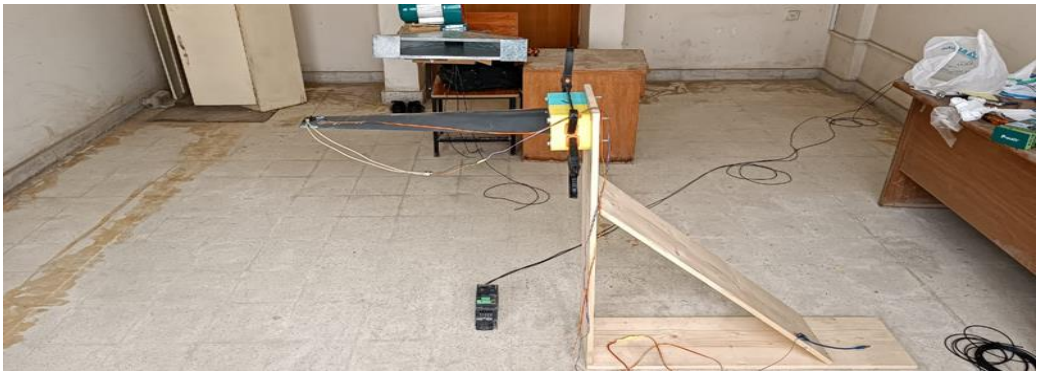

Figure 0.6. Photographer for experiment.

As shown Figure 3.7, the experiment relies on airflow, which is provided by a centrifugal fan. The controls fine-tune the airflow near the blower, There is also a displayed air velocity meter for precise determination of the air's velocity.

Figure 0.7. The Photographer for components.

In this Figure 3.8 An essential part of the experiment is to achieve wing stability and a secure connection to a fixed pillar with as slight vibration as possible. The primary goal is to separate the vibrations caused by the air vortex. This picture exemplifies the careful planning and building that ensured the wing would not come loose from the pillar under any circumstances. Keeping the link solid and free of tremors.

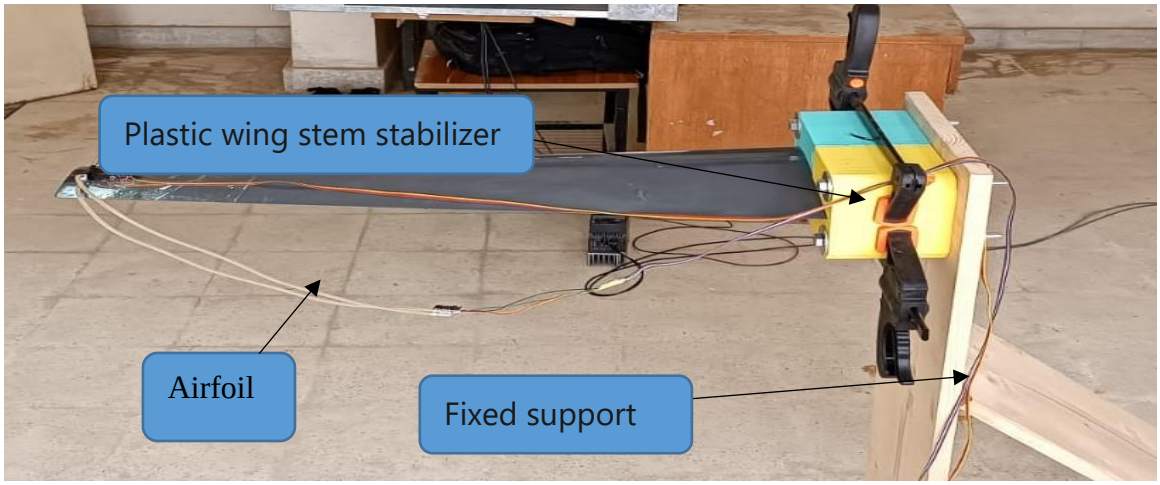

Figure 0.8. The Photographer for wing and fixed support.

Careful vibration and wind speed sensors installation at critical locations where wing vibration is most noticeable is essential. Their pinpoint positioning guarantees they will perform optimally, allowing for exact data collecting near the points at which wing vibrations are generated. This image exemplifies the careful consideration of sensor placement, which is essential for obtaining accurate results. By providing the sensors with a stable platform, this system facilitates in-depth investigation into the wing's vibrational characteristics and the impact of wind speed on its behavior. The relevant code for each sensor, used for data collection and transmission to the computer, is detailed in Appendix A. Data collection from the experiment's sensors is technically described and illustrated via the code implementation As shown Figure 3.9.

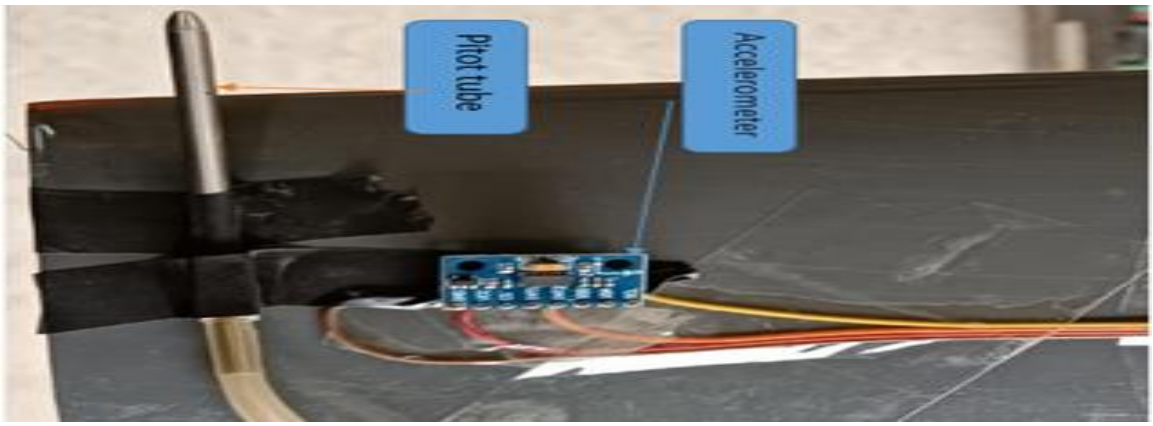

Figure 0.9. The Photographer for sensors.

After assembling all the numbers mentioned in the figures (3.6,3.7,3.8,3.9), the wing was clicked once, and the natural frequency is calculated and lasted ten seconds at a rate of 10 readings per second. and then the experiment started by pushing the air on the wing after conducting the experiment, we have three speeds at each speed. Input data, Collected data from sensors placed at the tip of the wing. Measured air velocity and vibration acceleration over a period of 30 seconds at a rate of ten readings per second, resulting in 300 data points, Preprocessed the collected data by filtering, resampling, or removing any noise or outliers. Ensured that the data was properly scaled and formatted for further analysis by low pass filter. We have obtained the vibration amplitude, the amount of displacement of the aircraft wing upwards and downwards, measured in (m /s^2), using the MATLAB method, the vibration amplitude was converted into a vibration In Hertz, the amount of its effect is measured by dB The code is placed in Appendix A, in the table each speed and how many information and how many matrices.

Table 0.5. The number and data of information.

Speed	Data	Matrices	columns	type
10 m/s	300	2	1	300 for speed 300 for vibration
15 m/s	300	2	1	300 for speed 300 for vibration
20 m/s	300	2	1	300 for speed 300 for vibration

3.5. RESULT EXPERIMENT

The amplitude, measured in meters per second squared, is the most significant magnitude of acceleration felt during a single cycle of vibration or oscillation. Quantifying acceleration intensity or strength is crucial in assessing and constructing vibration-affected systems. the figures (3.10, 3.12, 3.14. 3.16) show the vibration after entering a unit m/s2 after transferring the data that was taken from the experiment, We gave 300 parameters representing the vibration, and the result was the amplitude of the vibration.

The frequency (on a logarithmic scale, Hertz) is shown along the x-axis, and the magnitude response (on the y-axis) is expressed in decibels. At each frequency, the magnitude response is the power output divided by the power input. The magnitude response can be more efficiently represented over a wide range of values using the dB scale. As a result, responses across a wide range of magnitudes are simpler to visualize and compare. Positive numbers show frequency-dependent Amplification or attenuation, whereas negative ones show attenuation. the figures (3.11, 3.13, 3.15, 3.17) show the pointed of the vibration after converting it by code to Hertz and calculating its intensity dB.

3.5.1. Data Natural Frequency

In Figure 3.10 graph represents the amplitude in the natural frequency of an aircraft wing in response to an external force. Over ten seconds, the amplitude is measured, and the range is from -0.15 to 0.2 m/s^2 for the frequency.

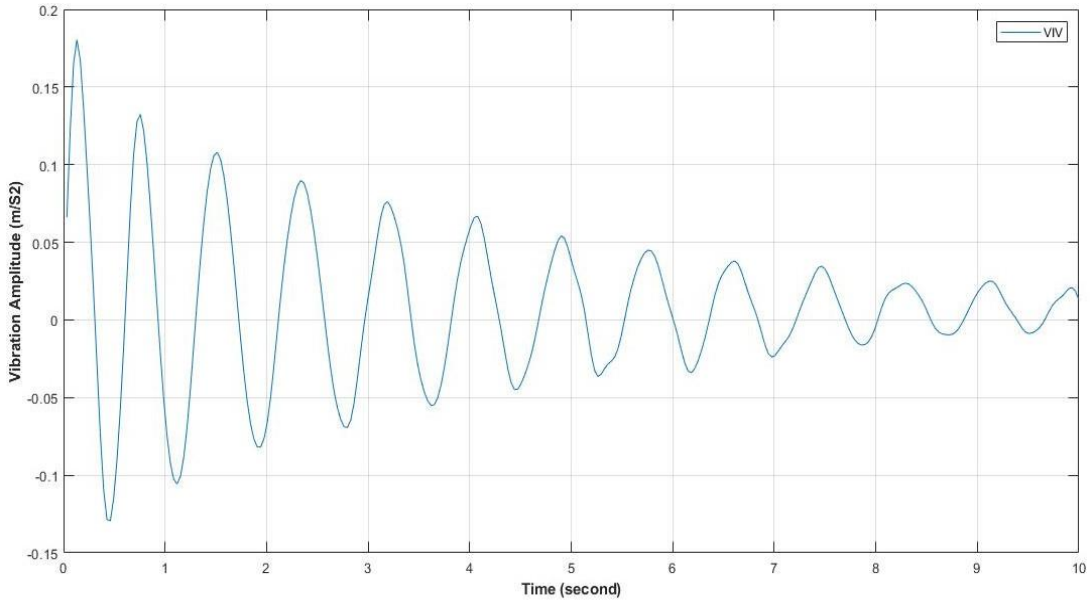

Figure 0.10. VIV of natural frequency.

In Figure 3.11 utilizing the MATLAB program and the code provided in Appendix A, the vibration amplitude was converted into a vibration magnitude of 8.54 dB at a frequency of 3.94 Hz.

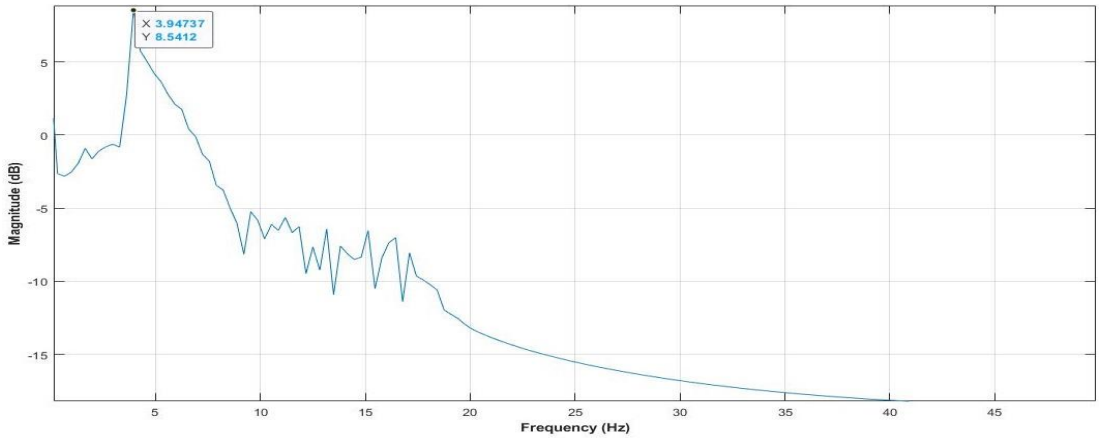

Figure 0.11. The magnitude and frequency vibration.

3.5.2. At Speed=10m/s

In Figure 3.12 amplitude of VIV (Vortex-Induced Vibration) can vary from -1.0 to 0.8 m/s^2, as seen in the image. This into the intensity of VIV experienced by the system under investigation. The spectrum of amplitudes displays the spectrum of vibrations caused by the vortices.

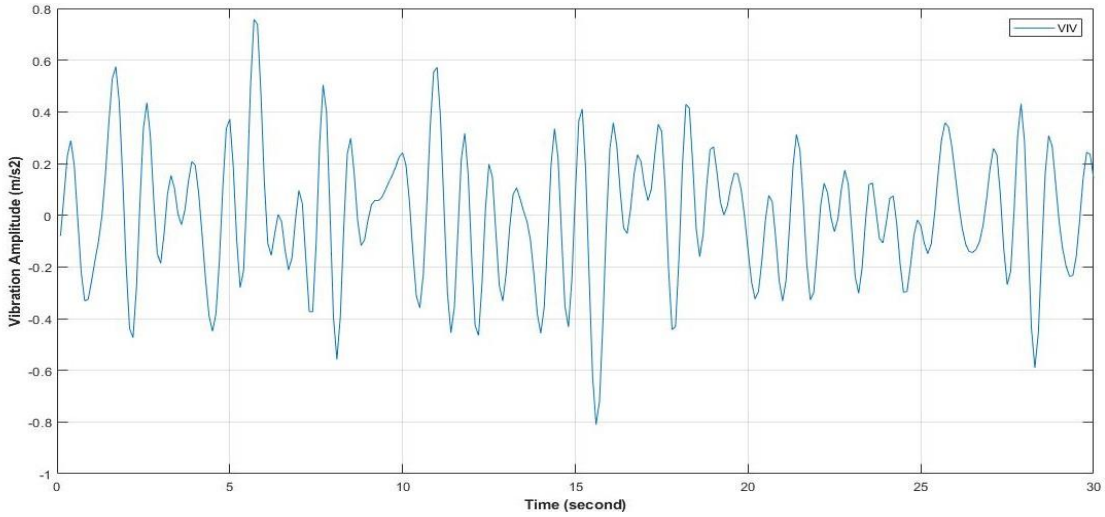

Figure 0.12. Vortex-induced vibration at speed 10 m/s.

The highest magnitude of vibration measured was 12,620 dB at a frequency of 13.33 Hz, as shown Figure 3.13 which was recorded at 10 meters per second. This high magnitude of vibration demonstrated.

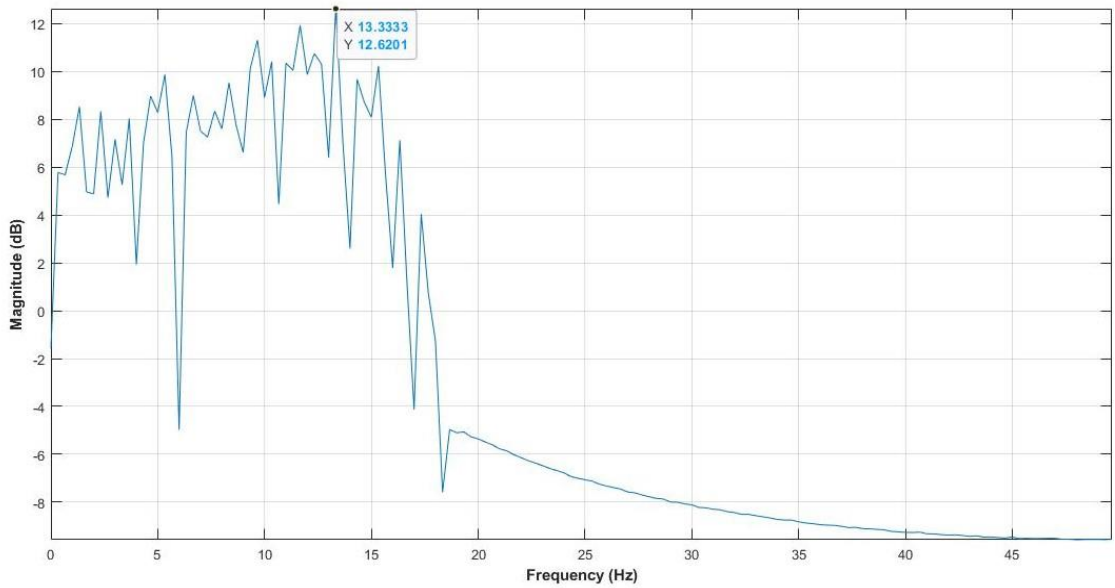

Figure 0.13. The magnitude and frequency of the vibrations, in 10 m/s.

3.5.3. At Speed 15 m/s

The range of vibration amplitudes increases from -0.2 to 0.2 m/s^2 as the air velocity increases from 10 to 15 m/s as shown in Figure 3.14.

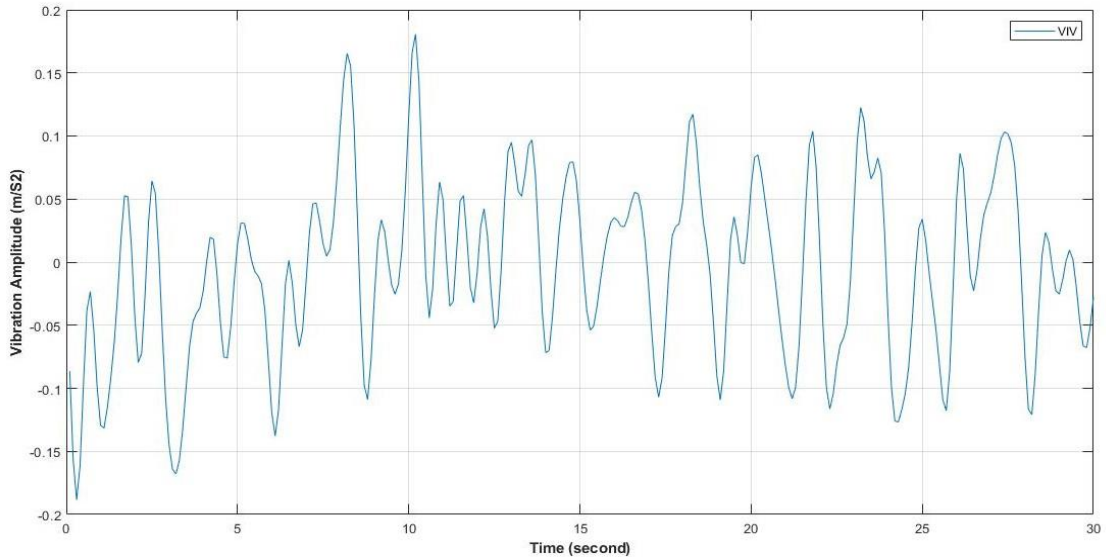

Figure 0.14. Vortex-induced vibration at speed 15 m/s.

From the figure retrieved from MATLAB, seems to be the high point in the vibration magnitude, corresponding to 6.560 dB at 5.66 Hz as shown in figure 3.15.

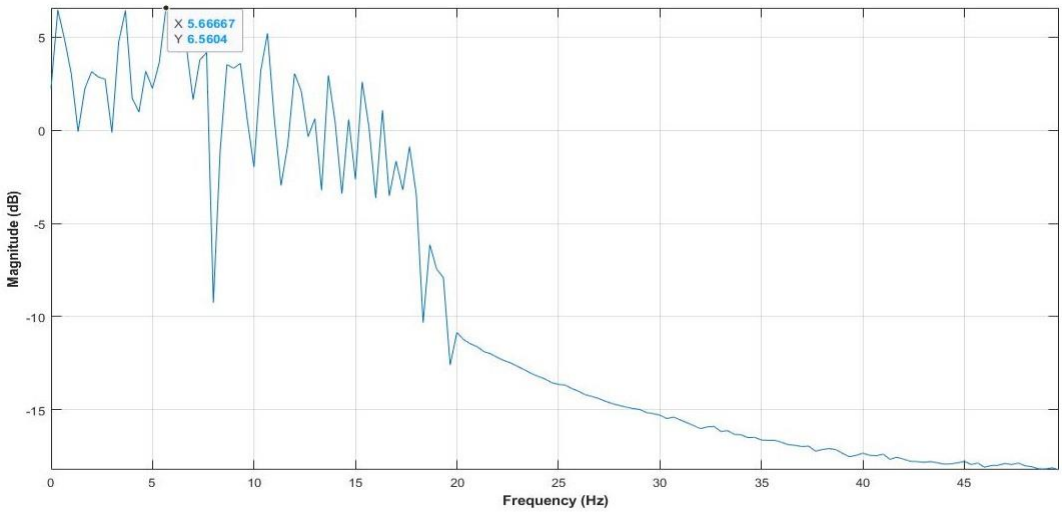

Figure 0.15. The magnitude and frequency of the vibrations, in 15 m/s.

3.5.4. At Speed 20 m/s

When the wing's impulsive air velocity was increased to 20 m/s, the resulting vibration amplitude range was between -0.4 and 0.2 m/s2 as shown in figure 3.16.

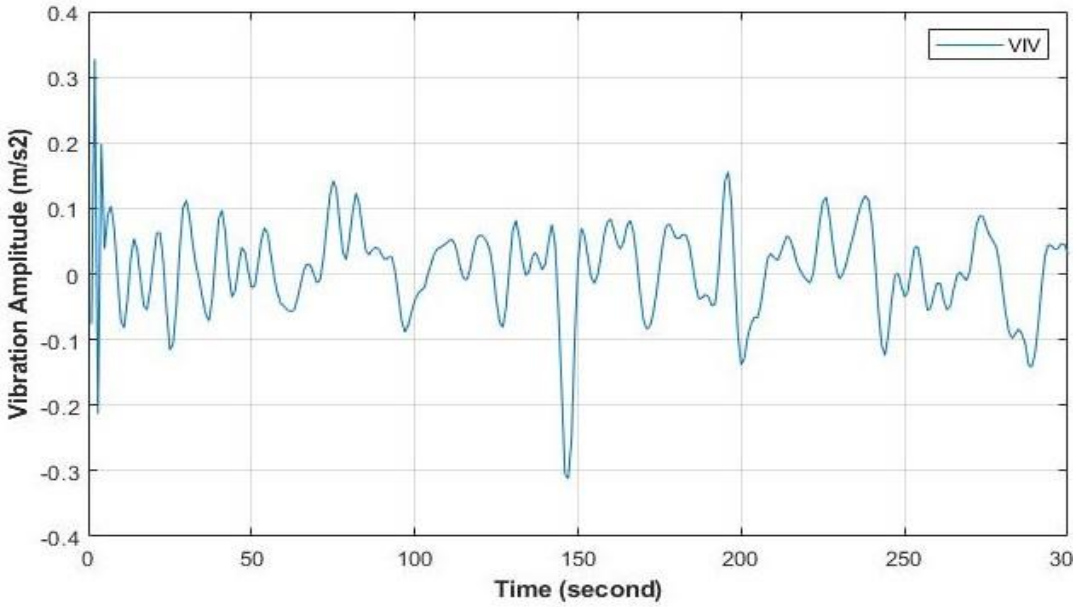

Figure 0.16. Vortex-induced vibration at speed 20 m/s.

In Figure 3.18, the converted vibration magnitude was found to be 6.3 dB at 2.66 Hz.

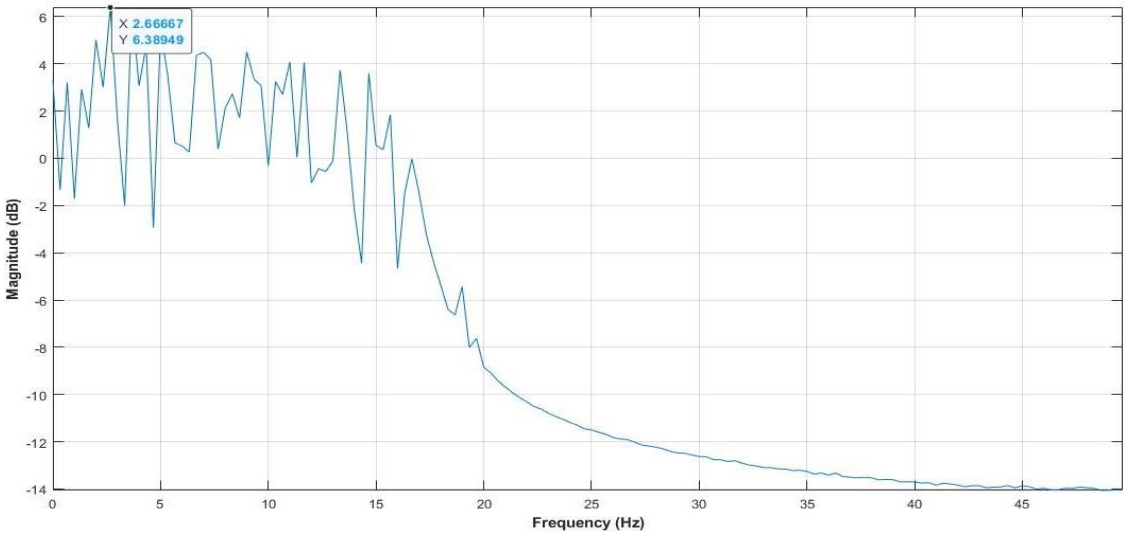

Figure 0.17. The magnitude and frequency of the vibrations, in 20 m/s.

PART 4

SYSTEM IDENTIFICATION

4.1. PREFACE

This chapter describes the dynamic modeling of an aircraft wing subjected to vibration using nonlinear SI techniques. A laboratory size Experimental setup of an aircraft wing to vibration was designed and developed to collect input-output data to model the nonlinear behavior of the wing. the dynamic behavior representation of an aircraft wing consists of two nonparametric, Systems intelligence (SI) techniques include neural network time series (NNTS). The approach included the best-characterized neural network time-series method: the one that used nonlinear external (external) input (NN-NARX) models.

4.2. SYSTEM IDENTIFICATION (SI)

Using input and output data, a system's mathematical model can be identified or quantified through a process called system identification (SI). The dynamic behavior of a pipe riser suffering VIV in maritime applications was predicted using SI in this thesis (Figure 4.1) [56], [57].

The SI technique first determines the model structure after collecting input/output data based on the experimental setup. The model estimation coefficient is then evaluated using validation approaches such as MSE. Finally, the validation methods are compared against the actual and predicted outputs. Put succinctly, to create mathematical models of dynamic systems, SI employs statistical approaches to interpret data collected from experiments. In this part, the input-output relationship is modeled using NARX model.

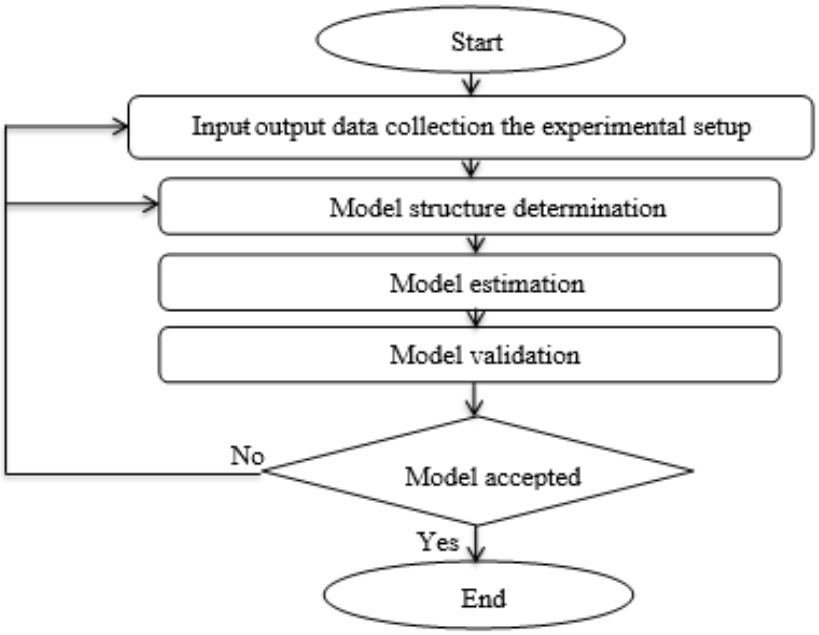

Figure 0.1. SI flowchart [58].

4.3. MODEL STRUCTURE DETERMINATION

Used to describe the steps used to settle on a workable architecture for a machine learning model. How well a model learns and generalizes from data, as well as how well it performs on a given task, are all heavily dependent on the model's structure. Investigate several neural network topologies and machine learning algorithms that might be applicable to the issue at hand. Different model structures can be trained using the training set, their performance can be evaluated using the validation set, and the final model can be tested using the test set.

4.3.1. Model with Nonlinear Auto-Regressive Inputs (NARX)

Nonlinear Auto Regressive with exogenous inputs (NARX) describes this type of model. It is a specific kind of artificial neural network (ANN) design in the context of modeling and predicting time series data. Nonlinear relationships and complicated dynamic behavior in the data are ideal situations for NARX networks to excel in. The autoregressive (AR) and the exogenous input (X) components are essential to the NARX network. The autoregressive component describes the connection between the present and previous outputs, while the exogenous input component describes the

connection between the current output and other inputs or factors. When training a NARX network, past values of the output and their corresponding exogenous inputs are used to make prediction values of the output. By optimizing its weights with a method like gradient descent, the network learns to simulate the nonlinear interactions and dependencies between the inputs and outputs. Time series forecasting, system identification, and control are some domains where the NARX architecture shines. This method has been put to good use wherever precise forecasts of complicated and nonlinear time series data are needed, such as in finance, economics, engineering, and environmental modeling.

When building the architecture of a neural network, choosing the total number of hidden neurons is a pivotal choice. How many hidden neurons should be used is a trade-off between model complexity and generalization ability and depends on various parameters, such as the problem's difficulty, the training dataset's size, and the intended trade-off. If a neural network has delayed connections, then that network has a certain number of delays, which can be measured in terms of the number of time steps or layers. Delayed connections allow data to travel from a one-time step or layer to the next layer, allowing the network to learn and remember temporal dependencies. In order to assess how well a regression model performs.

A NN-NARX model's error measures how far off its predictions are from the actual values of the target variable. It quantifies the dissimilarity between the expected and actual results for a single input. The NN-NARX model attempts to maximize predicted accuracy and congruence with the truth by decreasing the size of the error or mistake. The model's predictions will be more accurate and dependable if the error is reduced to a minimum. Mean square error (MSE) and similar metrics are frequently used to quantify the error and show how far off the estimates were from the actual results. one popular metric is the Mean Square Error (MSE), defined as the average squared difference between the predicted and actual values. A good indicator of the model's accuracy.

Several studies employed the NARX structural model for SI and control purposes. Below is a definition of the NARX algorithm [59]:

$$y(k) = \frac{B(z^{-1})}{A(z^{-1})}\, u(k) + \frac{\xi(k)}{A(z^{-1})} \tag{0.1}$$

One alternative rendering is as

$$A(z^{-1})\, y(k) = B(z^{-1})\, u(k) + \xi(k) \tag{0.2}$$

Where

$$A(z^{-1}) = 1 + a_1 z^{-1} + \cdots + a_n \mathrm{z}^{-\mathrm{n}}) \tag{0.3}$$

$$B(z^{-1}) = b_0 + b_1 z^{-1} + \cdots + b_n z^{-(n-1)}\ ) \tag{0.4}$$

Input data $u(k)$, *output* $y(k)$, *noise* $\xi(k)$,*and a back shift operator* $\boldsymbol{z^{-1}}$ are all shown below, with the polynomials having $A(z^{-1})$ and $B(z^{-1})$ related parameters, after neglecting the noise error $\boldsymbol{\xi(t)}$ and defining $B(z^{-1})$ and $A(z^{-1})$ the NARX becomes:

$$y(k) = f\ [y(k-1), \ldots., y(k-n_a)\, u(k-1),\ \ u(k-n_a)] \tag{0.5}$$

where n_a is the historical input and output value and f is the nonlinear function that can be implemented with smart tools like a Neural Network. analyze (VIV) how it reacts to being attacked from different directions.

4.3.2. System Identification by Neural Network

For nonlinear dynamic SI, a neural network is one of the methods of artificial intelligence that can be used. It is composed of many neurons (NE) grouped in distinct layers. a neural network model for a multilayer perceptron (MLP-NN) has at least three layers: the input layer (INL), hidden layer (HL), and output layer (OL) (OL). The hidden layer equations can be expressed as follows [37][60]:

$$v_1 = x_1 w_{11} + +x_2 w_{12} + y_1 w_{13} + y_2 w_{14} + b_1 \quad (0.6)$$

$$v_2 = x_1 w_{21} + +x_2 w_{22} + y_1 w_{23} + y_2 w_{24} + b_2 \quad (0.7)$$

$$f_1 = \frac{1}{1+e^{-v_1}} \quad (0.8)$$

$$f_2 = \frac{1}{1+e^{-v_2}} \quad (0.9)$$

where x_1,x_2 represent the real input data of the input network and, $\boldsymbol{y_1}$, $\boldsymbol{y_2}$ represent the actual output of the input network., w_{11} , w_{12} , w_{13} , w_{14} , w_{21}, w_{22} , w_{23} , w_{24} represent the weights between INL and HL, b_1 , b_2 represent the bias weights for HL, $v1$,v_2 represent the summing values for HL and f_1 , f_2 represents the final values for HL.

In Figure 4.2 and Figure 4.3 feature inputs (x_1, x_2, x_3,..., x_n) are represented by nodes in the input layer. Each neuron in the first hidden layer receives input from each of the input features. Between the input and output levels is where the "hidden" layers come into play. There are many hidden neurons, or nodes, in each hidden layer. The outputs of the hidden neurons are passed on to the next layer, while inputs are taken from the layer below (either the input layer or the previously hidden layer). Nodes in the output layer represent the network's output values (y_1, y_2, y_3,..., y_n). In a neural network, the number of nodes in the output layer changes according on the type of task being performed. The network's final predictions or choices are produced by these nodes.

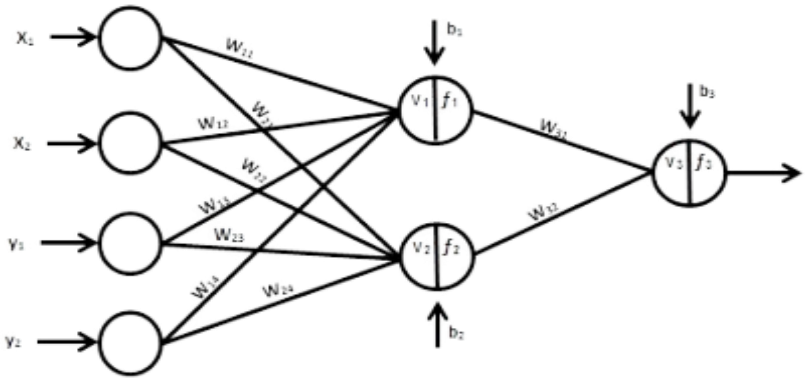

Figure 0.2. Structure of neural network[61].

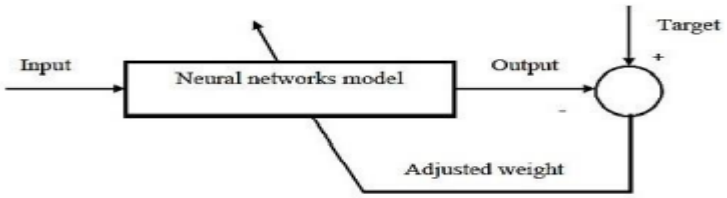

Figure 0.3. Schematic diagram of a neural network [62].

The equations for the OL can be formulated as follows:

$$v_3 = f_1 w_{31} + f_2 w_{32} + b_3 \tag{0.10}$$

$$f_3 = \frac{1}{1+e^{-v_3}} \tag{0.11}$$

where w_{31} , w_{32} represent the weights between the hidden layer (HL) and the output layer (OL), b_3 represents the bias weight for the OL, v_3 represents the summation value for the OL, and f 3 represents a final value predicted to the OL and f_3 represents a final value predicted to the OL Figure 4.5 illustrates how the LMSE validation technique clarifies the neural network implementation by defining the best identification in terms of the number of hidden neurons (NE) and the number of delays (ND).

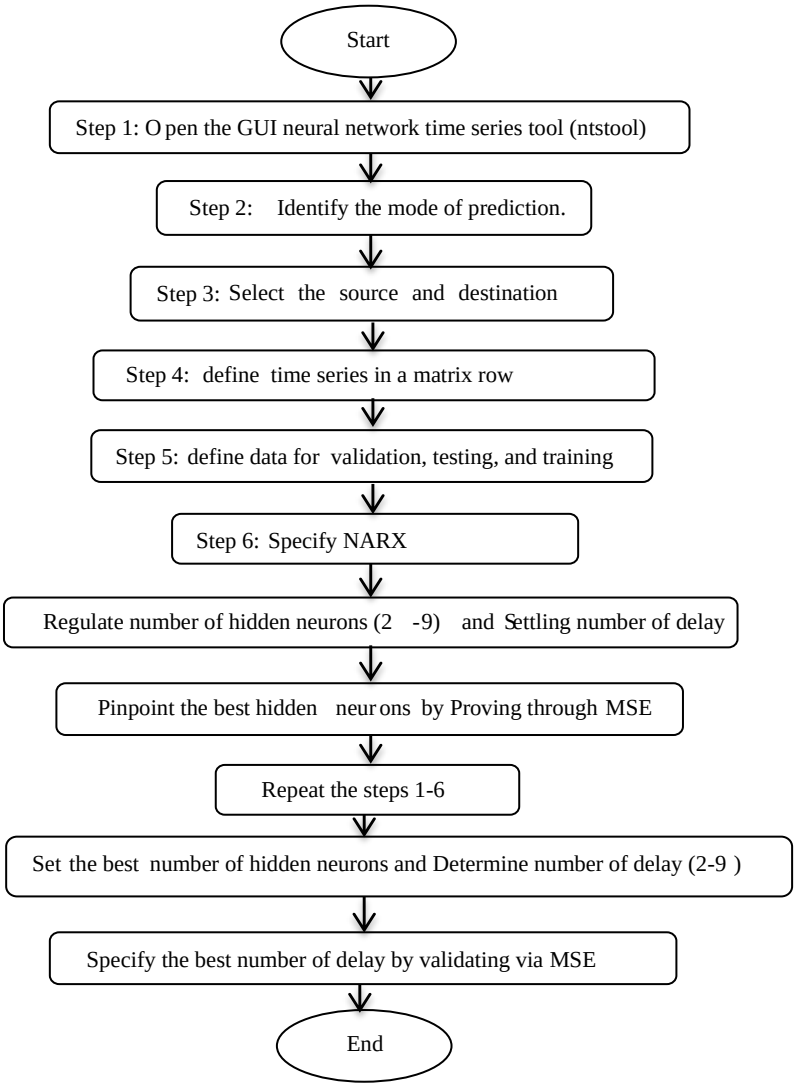

Figure 0.4. Neural network flowchart steps [58].

$$\boldsymbol{\varepsilon(t) = \frac{1}{N}\sum_{t=1}^{N} y(t) - \hat{y}(t)^2} \qquad (0.12)$$

Where:

$y(t)$is the actual output

$\hat{y}(t)$is the predicted output

4.4. SYSTEM IDENTIFICATION MODEL

Here, we show you the outcomes of using NN-NARX-style nonlinear SI approaches to the dynamic model. the experimental setup's input and output data were used to illustrate the nonlinear SI models. The input data flow was represented by 10 samples per second for 30 seconds, and it included 300 data sets. in order to build this model, 300 data sets were employed. The information was split three ways: 180 for training, 60 for verifying, and 60 for testing. finding the optimal model to represent the system was a two-stage procedure. It was found that keeping the ND constant at 2 and varying the NE from 2 to 9 resulted in the smallest mean square error (MSE). Second, the LMSE of the NE was used to determine the ND that resulted in the lowest MSE, with possible values ranging from 2 to 9.

According to Table 4.1 and Table 4.2 the NN-NARX model achieved the best MSE of 0.0027 with NE = 4 and ND = 2, while the best MSE of 0.0028 was achieved with NE = 4 and ND = 3.

Table 0.1. MSE for the NN-NARX model at ND = 2 in 10 m/s.

NE	MSE
2	0.0039
3	0.0028
4	0.0027
5	0.0082
6	0.0241
7	0.0603
8	0.0235
9	0.0058

Table 0.2. MSE for the NN-NARX model at NE = 4 in 10 m/s.

ND	MSE
2	0.0029
3	0.0028
4	0.0029
5	0.0029
6	0.0029
7	0.0029
8	0.003
9	0.003

As shown Figure 4.5 to prepare for the wind speed and vibration data at a 10 m/s wind speed, the neural network window should be accessed. In the neural network window, the neural network type is set to NARX (Nonlinear Autoregressive with Exogenous Input). the data is divided into three sets: 60% for training, 20% for validation, and the remaining 20% for testing. In the NARX model, the parameters NE (number of delays) and ND (number of neurons) can be adjusted according to preference. For this particular case, NE is set to 4 and ND is set to 3. results of the MSE for each part of the process.

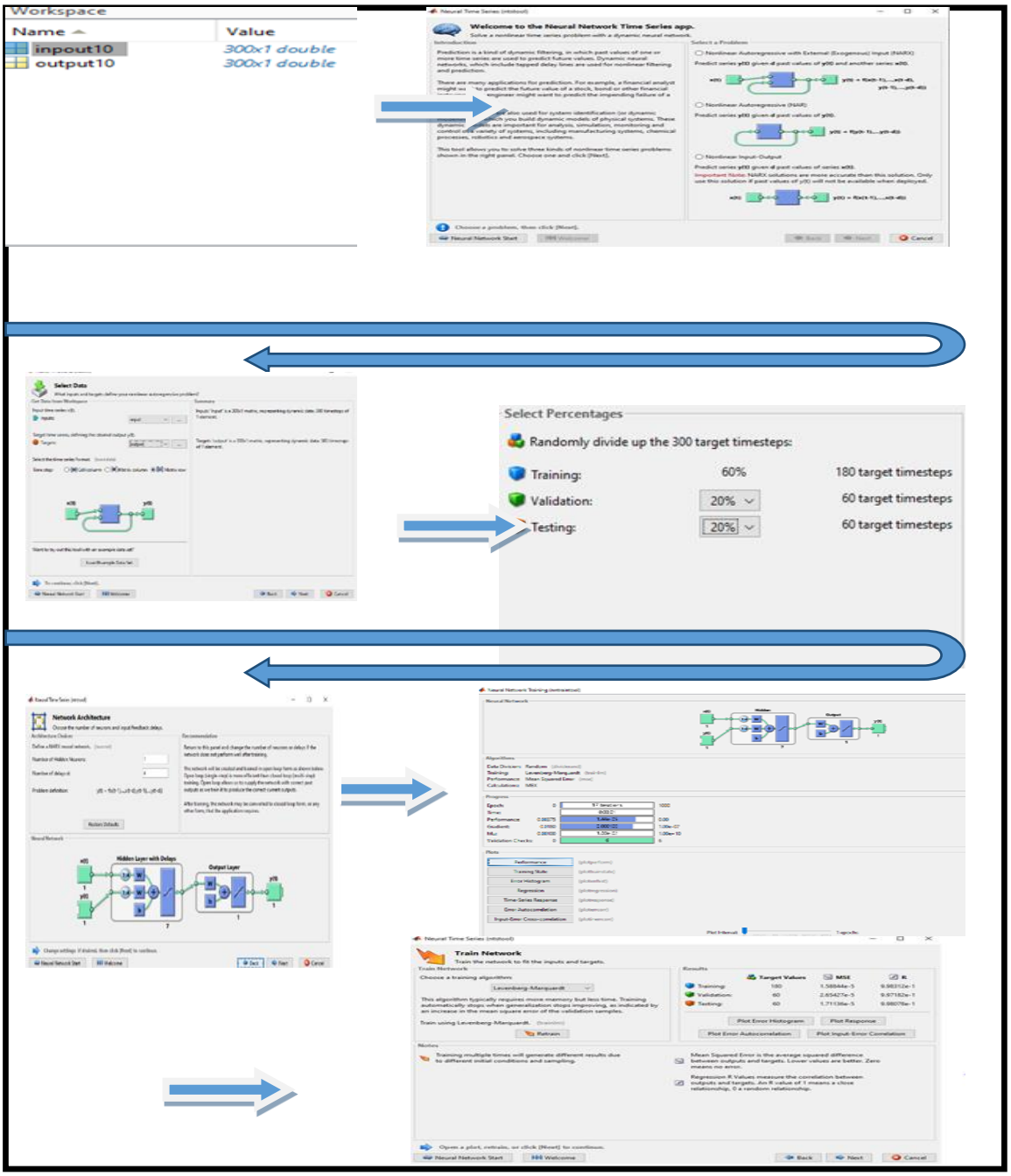

Figure 0.5. Adjusting the settings of a neural network in 10 m/s.

According to Table 4.3 and Table 4.4, the NN-NARX model achieved the best MSE of 0.000034389 with NE = 4 and ND = 2, while the best MSE of was 0.000031376 achieved with NE = 4 and ND = 7.

Table 0.3. MSE for the NN-NARX model at ND = 2 in 15 m/s.

NE	MSE
2	0.00018114
3	0.00011997
4	0.000034389
5	0.000044715
6	0.00008756
7	0.0002568295
8	0.000089618
9	0.0001355

Table 0.4. MSE for the NN-NARX model at NE = 4 in 15 m/s.

ND	MSE
2	0.000034732
3	0.000034269
4	0.000035217
5	0.000036791
6	0.000031376
7	0.000031376
8	0.000037359
9	0.000036242

The neural network window needs to be accessible in order to get ready for the wind speed and vibration data at 15 m/s. The NARX (Nonlinear Autoregressive with Exogenous Input) neural network type is selected in the network window. 180 of the data is used for training, 60 for validation, and the remaining 60 is used for testing. The NARX model allows for customization via the parameters NE and ND. NE gets the value 4 while ND gets the value 7. The MSE is calculated by comparing the trained network's performance on the testing data to the trained network's performance on the training as show figure 4.6.

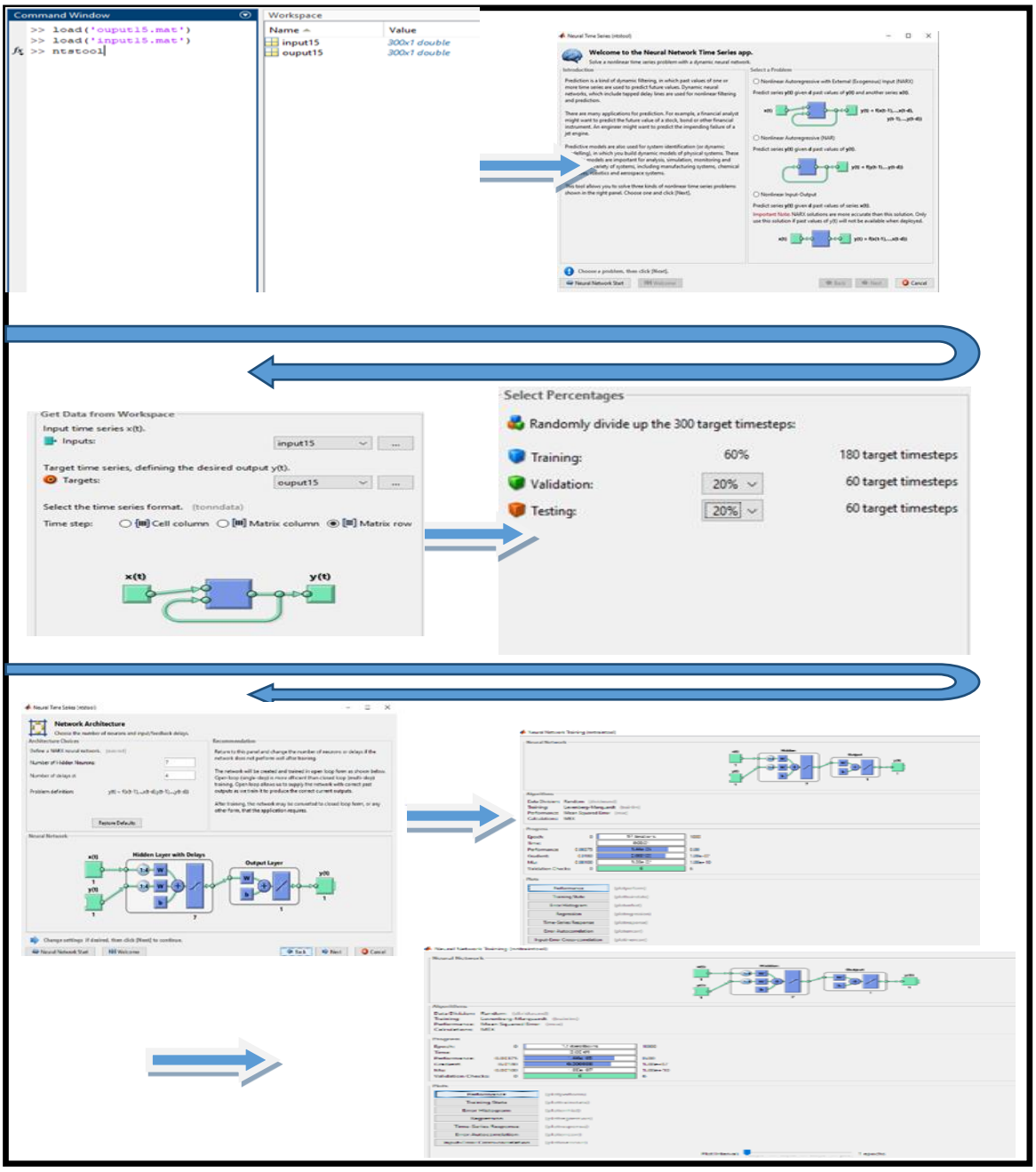

Figure 0.6. Neural network configuration at 15 m/s.

Table 4.5 and Table 4.6 show that the NN-NARX model achieves the best results was 0.00033758 with NE = 4 and ND = 2, while the second best results with NE = 4 and ND = 4 yield an MSE of 0.00064992.

Table 0.5. MSE for the NN-NARX model at ND = 2 in 20 m/s.

NE	MSE
2	0.00031191
3	0.00033758
4	0.00033758
5	0.0022
6	0.0061
7	0.0164
8	0.004
9	0.00093215

Table 0.6. MSE for the NN-NARX model at NE = 4 in 20 m/s.

ND	MSE
2	0.00092573
3	0.00076226
4	0.00064992
5	0.00093681
6	0.00090765
7	0.0008484
8	0.00083811
9	0.00091279

The model was constructed using 300 data points collected at 20 meters per second. There were 180 samples used for training, 60 for validating, and 60 for testing. can see whether model does a better job of reflecting the system by looking at cases where both NE and ND get the value 4. Performance on the testing data is compared to performance on the training data, and the difference is used to determine the MSE. here, it is Figure 4.7 to see.

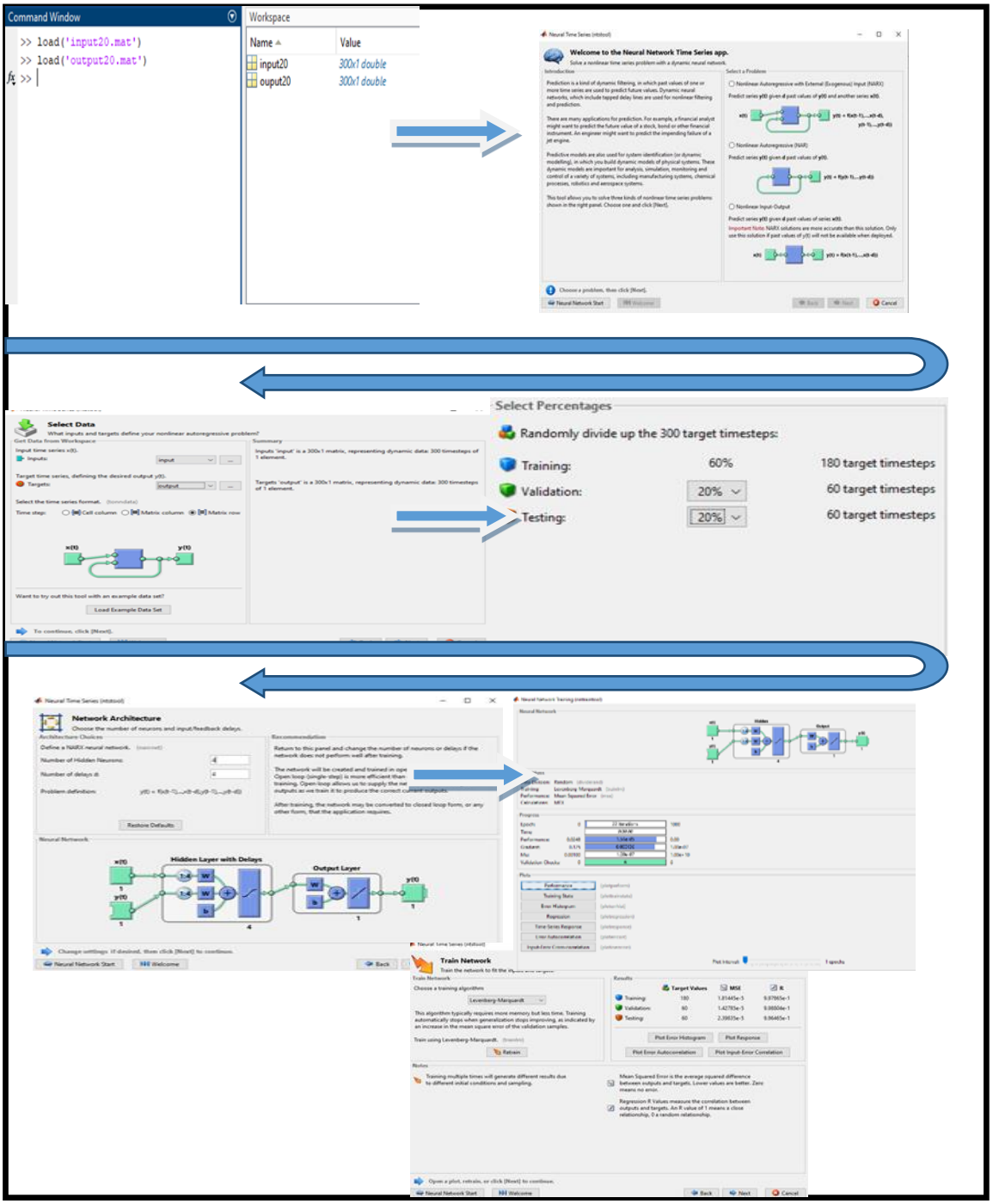

Figure 0.7. neural network configuration at 20 m/s.

Figure 4.8 how the box looks for the least error-prone trained and corrected NN-NARX model.

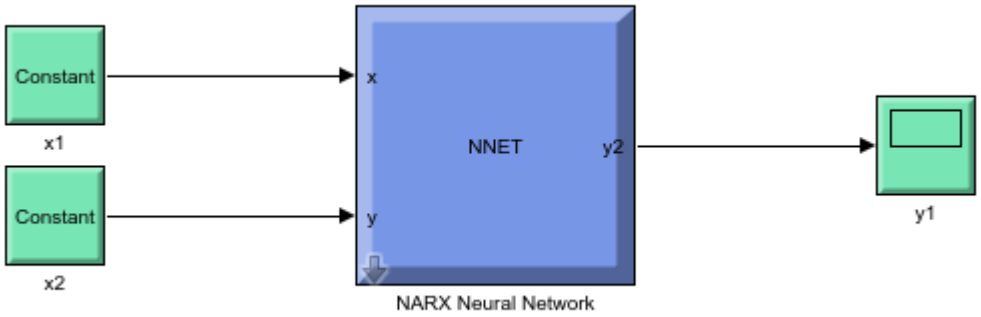

Figure 0.8. NN-NARX block diagram

In MATLAB, we make a matrix of velocity versus time, and another matrix of vibration versus time. It is entered into the block diagram in this form to give us the shape of the vibration that the NN-NARX Model expects of vibration and the shape of the error shown in Figure 4.9

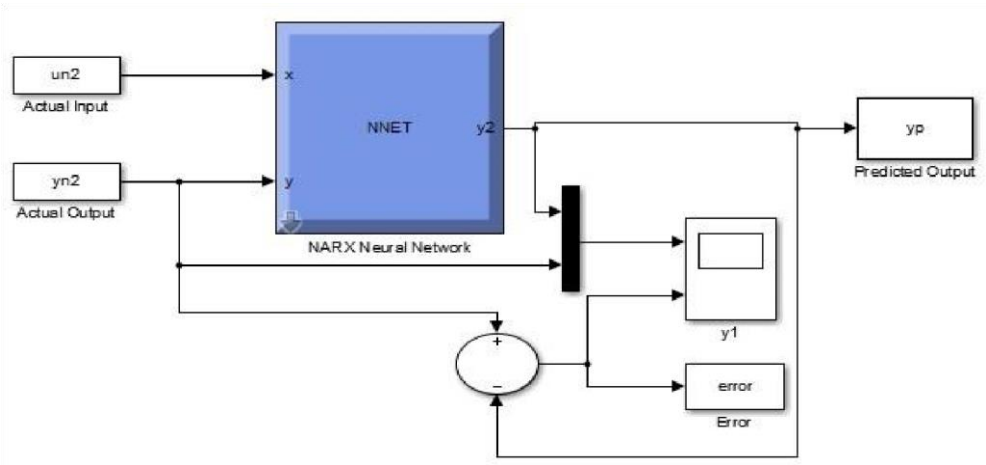

Figure 0.9. NN-NARX block diagram

4.5. SYSTEM IDENTIFICATION RESULTS

The modeling method was performed for three different speeds, and the results are shown here in graphical form. The actual vibration is represented in blue, while the predicted one is shown in red. The discrepancy between the two is seen on the error graph. To further ensure precise analysis and forecasting, we highlight the best Mean Square Error, the optimal number of hidden neurons, and the optimal delay count.

Table 0.7. MSE and define for NN-NARX model.

Speed	NE	ND	MSE
10 m/s	4	3	0.0028
15 m/s	4	7	0.000035217
20 m/s	4	4	0.00064992

This Table 4.7 summarises the Results for each speed, with the lowest MSE found at ND and NE.

4.5.1. NN-NARX Model at Speed 10 m/s

The NARX model's prediction of the expected vibration at a speed of 10 m/s is shown in Figure 4.10. There is a high degree of agreement between the anticipated and measured vibrations, demonstrating the model's validity. The model's accuracy in capturing the vibration behavior is further supported by the mean squared error (MSE) of 0.0028 achieved with NE = 4 and ND = 3.

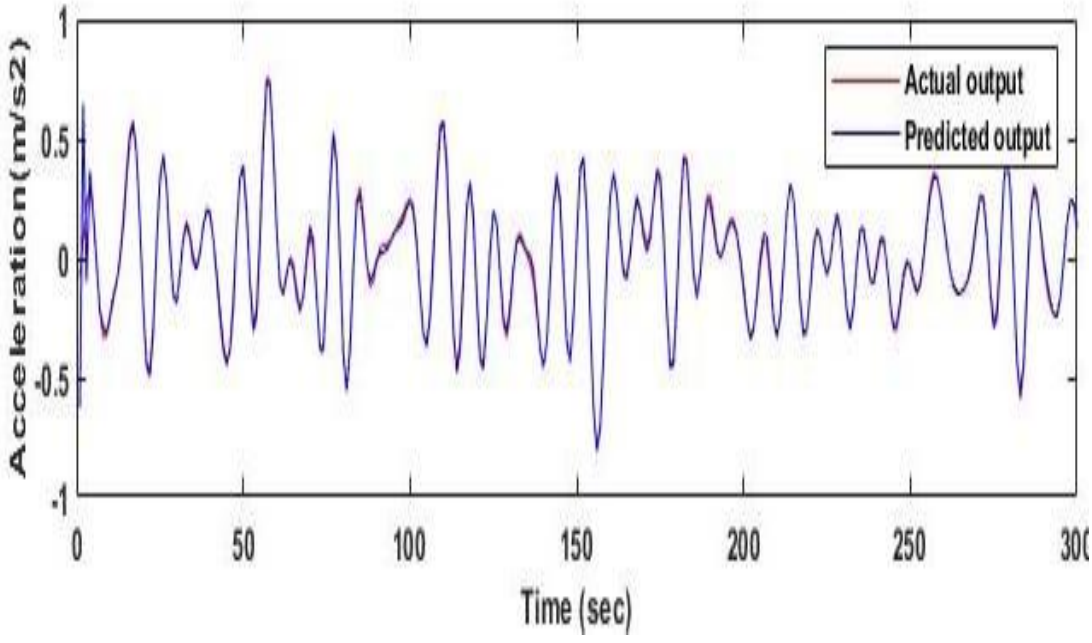

Figure 0.10. Vibration amplitude of NN- NARX in 10 m/s.

The NN-NARX model's error analysis is depicted in the diagram. Specifically, it shows in Figure 0.11 how the NN-NARX model's anticipated vibration differs from the observed vibration.

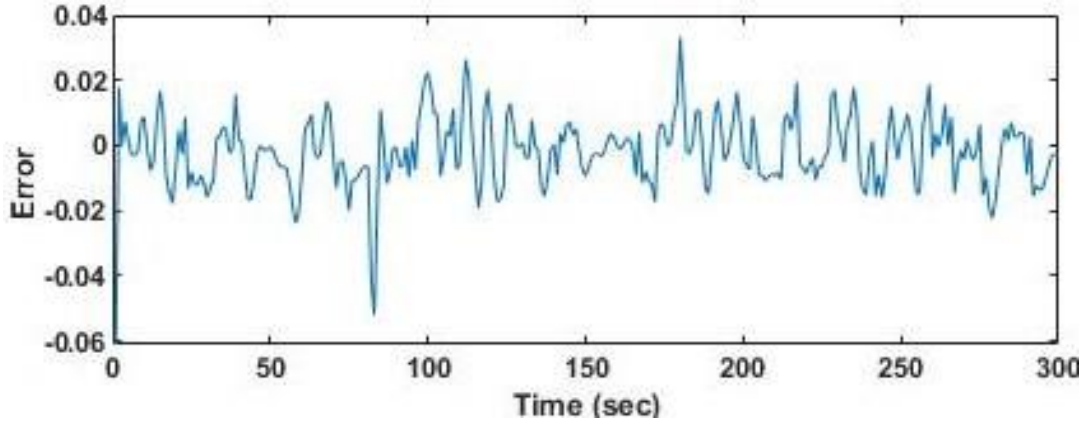

Figure 0.11. Error of NN- NARX in 10 m/s.

4.5.2. NN-NARX Model at Speed 15 m/s

Figure 4.12 vibration analysis showcases the NARX model's remarkable accuracy in predicting the expected vibration. At a speed of 15 m/s, the NARX model achieved an impressive performance with a minimum mean squared error (MSE) of 0.000035217. The model was trained with four hidden layers (NE = 4) and seven delays (ND = 7), resulting in a highly precise representation of the real vibration data.

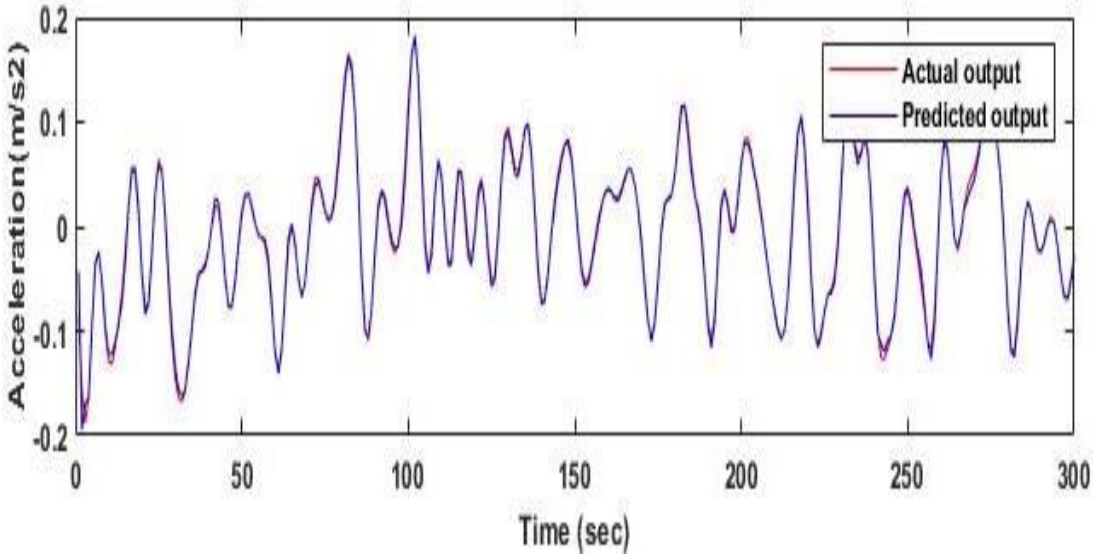

Figure 0.12. Vibration amplitude of NN- NARX in 15 m/s.

The discrepancy between the NN-NARX model's predictions and observed vibrations is an error in 15 m/s. The extent to which the model successfully represents vibrations of that velocity is dependent on its magnitude shown in Figure 4.13.

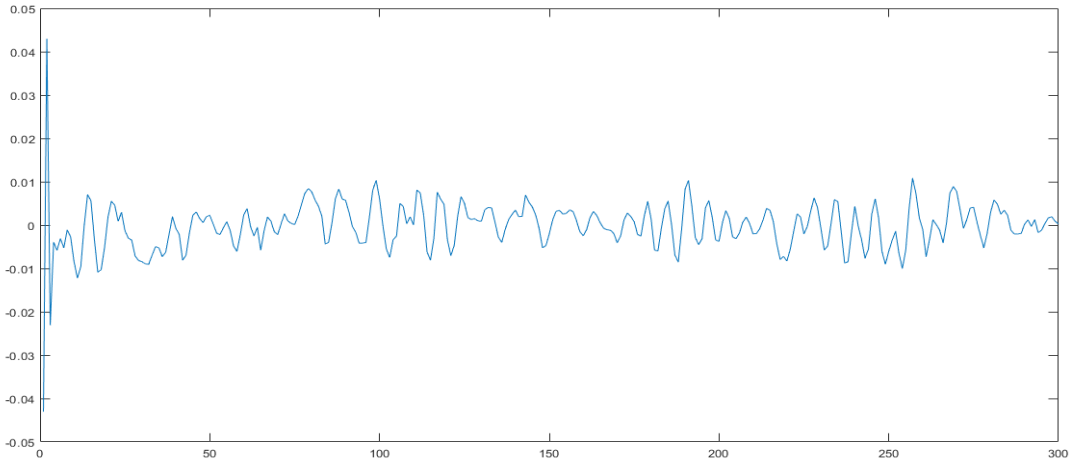

Figure 0.13. Error of NN- NARX in 15 m/s.

4.5.3. NN-NARX Model at speed 20m/s

Figure 4.14 vibration amplitudes of actual vibration (shown in blue) and the predicted vibration generated by the NARX model (shown in red) at a velocity of 20 m/s. when best MSE was 0.00064992 in NE = 4 and ND=4.

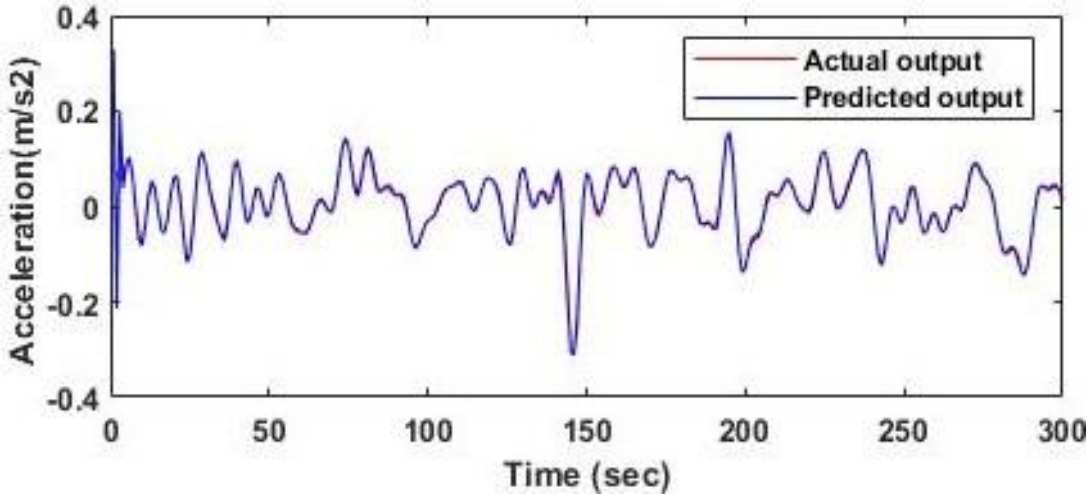

Figure 0.14. Vibration amplitude of NN- NARX in 20 m/s.

Figure 4.15 errors in forecasting vibrations are getting smaller. The model excels at 20 m/s, accurately portraying the dynamics of vibrations occurring at greater velocities. This result substantiates the NARX model's competence in foreseeing and evaluating drone wing vibrations.

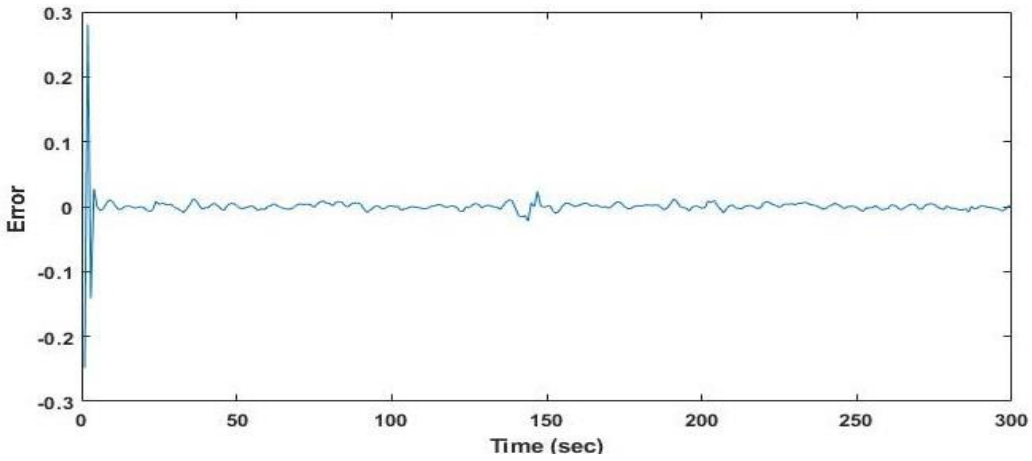

Figure 0.15. Error of NN- NARX in 20 m/s.

PART 5

RESULTS OF ACTIVE VIBRATION CONTROL

5.1. PREFACE

Proportional-Integral-Derivative (PID) is a standard control algorithm in engineering and automation. The difference between the target and actual output calibrates a control variable. Current error is addressed by the proportional part, the steady-state error is eliminated by an integral part, and the derivative part accounts for the rate of error growth. For reliable and precise operation, PID controllers are necessary.

Particle swarm optimization (PSO) is a metaheuristic optimization algorithm. It has modeled how animals act in groups, such as flocks of birds or schools of fish. In PSO, a swarm of particles traverses the problem space, changing its trajectory and speed according to its best local and global solutions. Non-linear problems and complex search spaces are where it shines. PSO is easy to apply and has shown promising results in many settings. it may converge too quickly. The research community has offered enhancements and variants to boost its effectiveness. When it comes to optimization, PSO is a formidable algorithm that can successfully simulate the work of a swarm.

The Particle Swarm Optimization (PSO) algorithm is combined with the PID control technique to form PID-PSO. The PID controller's parameters are optimized via PSO for improved control performance. It is widely utilized in control engineering applications because of how easily it automates the PID tuning process.

The effectiveness of a PID-PSO controller can be measured in terms of its Mean Square Error (MSE). The average squared deviation between the target value and the

system's output is calculated. PID-PSO aims to maximize control performance by reducing MSE through PSO-optimized PID gains.

The fitness value in PID-PSO measures the solution's quality relative to some performance criterion, such as Mean Squared Error (MSE). The PID parameters are optimized to reduce the fitness value. When discussing PSO for optimal parameters, the iterations refer to the total number of steps executed by PSO. The control problem's complexity and performance goals guide the fitness function selection and the number of iterations.

In order to mitigate the deflection of a segmented aircraft wing model due to VIV, this chapter gives a simulation of AVC techniques. The controller reduces the sway of the simulated wing when subjected to a perturbing load, such as that produced by a vortex. To fine-tune the controller's performance and increase its precision, smart optimization techniques were used [63].

controllers that use a sophisticated tuning method, Particle-swarm optimization (PID-PSO) and The AVC procedures use controllers based on the proportional-integral-derivative (PID) formula.

5.2. PID CONTROLLERS

Because of its stability, efficiency, and excellent quality, used extensively for factories' control systems. The optimal values for the controller parameters (KP, KI, and KD) are calculated. KP, KI, and KD all have an effect on the controller name. Any controller with a non-zero proportional gain and fixed other parameters is known as a P controller. The controller is said to be a PI controller if this both are non-zero and its derivative gain is also zero. A PD controller is one in which the integral gain is zero while the proportional as well as derivative gains are non-zero. In the end, a PID controller is defined as one in which no parameters are zero in value. Consequently, the PID controller's generic form.

depicted in Figure 5.1 was the primary emphasis of this section. Yet, one of the current difficulties is reprogramming the PID controller to exhibit intelligent behaviors by tuning its settings with the aid of intelligent optimization techniques [64]. Heuristic, particle swarm optimization (PSO), and a method for incrementally improving knowledge (iterative learning algorithm) (ILA) optimization techniques had been implemented to fine- tune PID settings. An expression for PID control in real time looks like this:

$$(t) = K_p\,(t) + K_I \int_0^t \mathrm{e(t)dt} + K_D \frac{\mathbf{de(t)}}{\boldsymbol{dt}} \tag{0.1}$$

Where u(t) is the output from the controller, KP, KI, and KD are the proportional, integral, and derivative gains, and e(t) is the deviation between the expected and actual output. The PID block form can be expressed similarly to how it is in the Laplace transform domain:

$$u(s) = \left(K_P + \frac{K_I}{S} + K_D S\right) e(s) \tag{0.2}$$

The derivative and integral terms of Eq. 5.1 are transformed into discrete time as follows:

$$\int_0^t e(t)dt \approx T \sum_{k=0}^{n} e(k) \tag{0.3}$$

$$\frac{d_e(t)}{dt} \approx \frac{e(k)-e(k-1)}{T} \quad \text{or} \quad \frac{\Delta e(k)}{T} \tag{0.4}$$

Then, at time t, the represents a single step, and Eq 5.1 simplifies to:

$$\mathrm{u(t)} = \mathrm{K_P e(k)} + \mathrm{K_I} \sum_{\mathrm{k=0}}^{\mathrm{n}} \mathrm{e(k)} + \mathrm{K_D \Delta e(k)} \tag{0.5}$$

The PID controller in discrete time by Laplace transform can be represented as:

$$G(z) = \left[K_P + \frac{K_I}{1-Z^{-1}} + K_D(1-Z^{-1})\right] e(z) \tag{0.6}$$

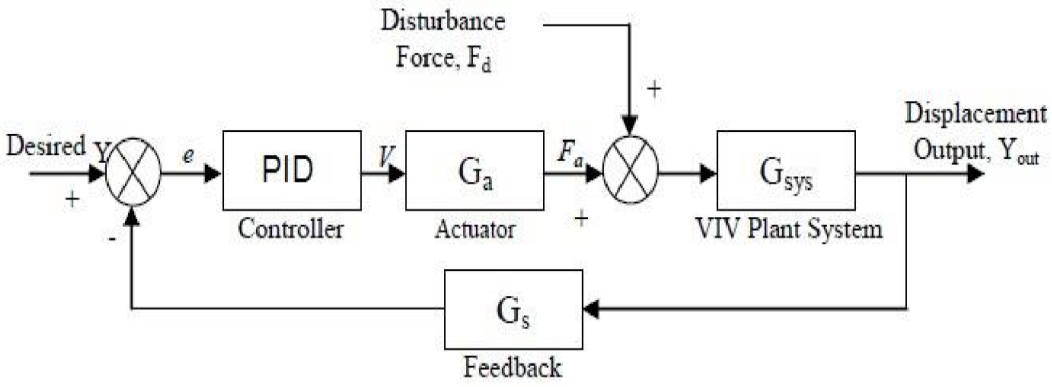

Figure 0.1. Basic scheme of a PID controller[64].

In Figure 5.1: An actuator is a device that produces a signal used to manipulate a system. Second, "Plant/System" stands for the actual system or process being managed. Third, the system's output is measured in order to receive feedback. The fourth step, "Error Calculation," involves calculating the difference between the target value and the actual output. Fifth, a PID controller uses the error to determine the control signal's P, I, and D terms. External forces or disturbances that affect the actuator or the system are accounted for in Actuator Disturbance, the sixth factor. An actuator drives the system in response to the calculated control signal. By monitoring the system's output and updating the error value, Feedback Displacement allows for constant fine-tuning.

5.3. PSO TUNING METHOD

To solve Non-linear dynamic problems In engineering fields in industrial applications that rely on a naive optimization technique can be solved, by modeling complex engineering systems after the cooperative efforts of animals such as fish schools, flocks of birds, and swarms of bees [49].

The method's underlying idea is based on the birds' velocities and locations; each bird symbolizes a solution to the search problem, working with and against the others in the process of solution development. Particles learn to fly better from each other and from their own experiences [65].

The i_{th} particle is denoted by $XI = xi_1, xi_2, ...,$ and the better prior location yielding the minimal number of fitness for just any particle is denoted, by $PI = pi_1, pi_2 ..., pi_d$, and is, therefore, the best-known position. A visitor, denoted by the letter g, is the particle in the population that has the highest probability of being the best particle. The following equations govern the updating of the particle velocity $VI = vi_1, vi_2, ... vi_d$. [47]:

$$V_{id}^{n+1} = W.V_{id}^{n} + c_1.rand(\quad).(p_{id}^{n} - x_{id}^{n}) + c_2.rand(\quad).(p_{gd}^{n} - x_{id}^{n}) \tag{0.7}$$

where the two positive constants, c1, and c2, were equal to 1.494, iterations, a swarm size of 40, gives back an unpredictable value between 0 and 1, generated by the function rand() [65], A new particle velocity is computed using Eq 5.6, which takes into account the particle's current velocity, its history, and the gap between where it is now and where it has been better in the past, both individually and collectively. Then the particle takes off in a straight line for its new destination. The integration to square error (ISE), absolute error (IAE) is the product of the IAE and the integration time (ITAE) were utilized as quantitative markers of fitness to evaluate the PID performance. PSO's Figure 5.3 illustrates the PSO tuning procedure [66]:

$$ISE = \int_0^{\infty} e^2(t).dt \tag{0.8}$$

$$IAE = \int_0^{\infty} |e_t|.dt \tag{0.9}$$

$$ITAE = \int_0^{\infty} t.|e_t|.dt \tag{0.10}$$

In Eq 5.6 The programming function "rand()" stands for a random number generator and is widely used. It takes an argument and returns a bogus random number between 0 and 1 when called. Each possible value in the range has an equal chance of being generated when the number is generated uniformly. The rand( ) function is frequently used in algorithms, simulations, and other applications that require randomization to introduce unpredictability or variety.

IAE considers the primary numerical difference between the expected and actual outputs, regardless of direction. It gives equal weight to positive and negative errors, providing a more accurate picture of the total deviation Eq 5.7 shows its mathematical equation.

By multiplying the absolute error by the period, ITAE captures a mistake's scale and persistence. It considers how long an error has been around and aims to minimize its size and persistence. Eq 5.8 shows its mathematical equation.

In conclusion, while all three metrics evaluate control system performance, ISE places more weight on squared errors, IAE on absolute errors, and ITAE on both. Metrics are selected following individual needs and priorities. Eq 5.9 shows its mathematical equation.

How ISE, IAE, and ITAE relate to the MES is determined by the method used to arrive at that figure. When there are significant outliers or faults in the system, ISE typically produces a more significant MES than IAE or ITAE. The MES percentage decreases when errors are balanced or dispersed around zero, as is the case with IAE and ITAE. The MES percentage and how it is arrived at and interpreted can change with different uses and settings.

The best position (P best) Shows the optimal answer that a single particle has come up with. The P best value of each particle is kept in isolation. helps the particle narrow down its search area, movement, and velocity updates for the particle are affected.

Global best (G best) represents the optimal solution found by any swarm particle. Common to all swarm particles, provides a standard against which all particles can be measured. affects how particles behave and how their velocities are updated.

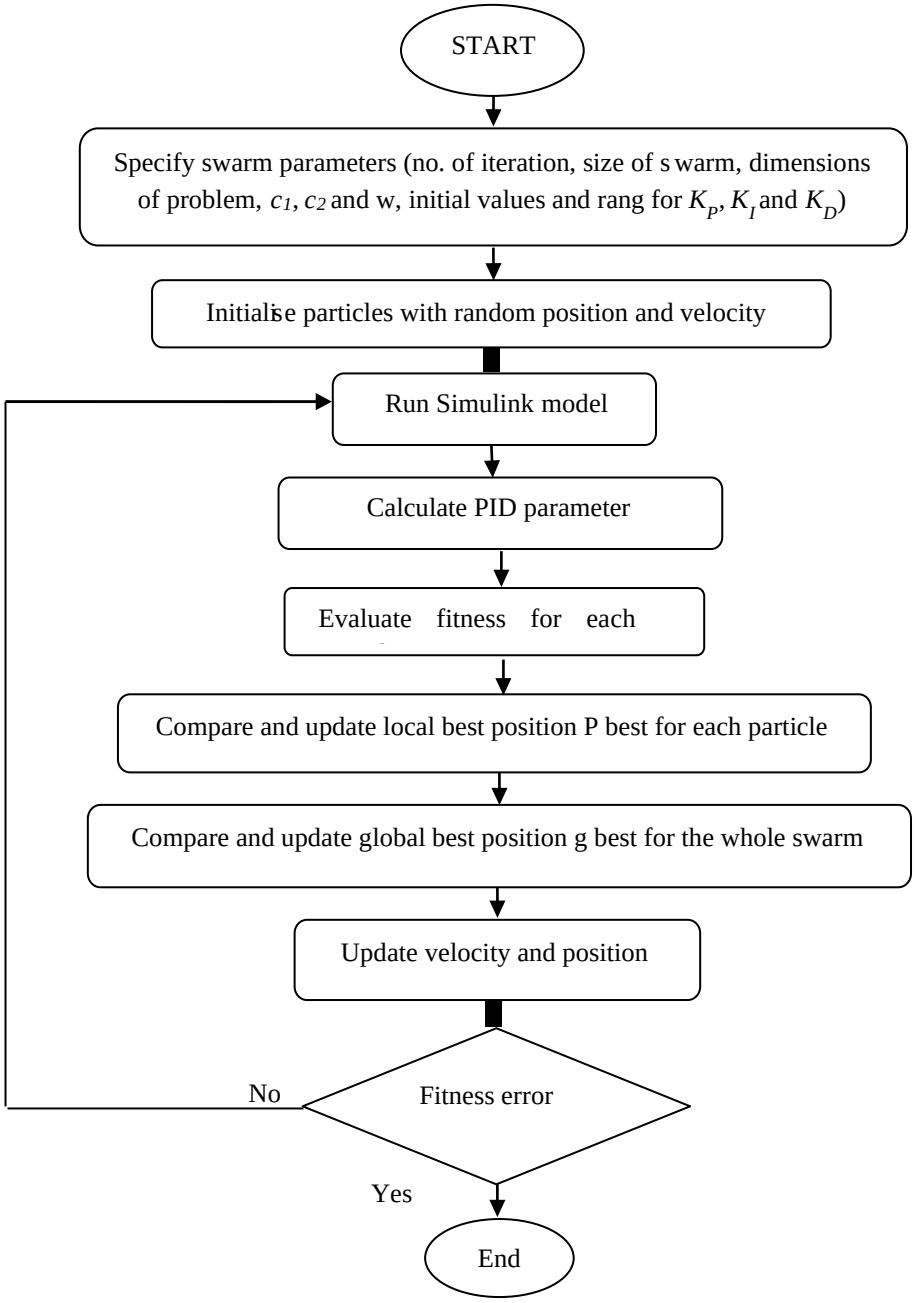

Figure 0.2. PSO tuning method flowchart.

The work steps in the Figure5.2 can be illustrated as follows:

1. Define swarm parameters: Determine the number of iterations, the size of the swarm, the dimensions of the problem, the coefficients, and the starting values for the PID parameters that will be used by the PSO method.
2. Create particles with uniformly distributed initial locations and initial velocities within the range of parameters.

3. Run the Simulink model representing the system that will be controlled or tuned using the PID parameters; this involves setting up and running the model.
4. Determine the PID parameters based on the particle positions using a predetermined mapping or equation.
5. Run the Simulink model using each particle's PID parameters and evaluate the system's fitness or performance.
6. If an improvement is detected in the fitness between each particle's current and best positions, the local best position is updated.
7. Update the global best position by evaluating how each particle's current location stacks up against the best position discovered by each swarm member.
8. Particle velocities and locations are updated using equations and coefficients that consider the best possible places at both the local and global scales.
9. Verify the fitness error and continue or stop: See how the post-update fitness error stacks up. If fixing the problem is not enough, start over at Step 3. Stop optimizing if the margin of error is tolerable.

5.4. ACTIVE VIBRATION CONTROL SIMULATION

The (NN-NARX) SI model of VIV use to calibrate the use of a PID controller, which stands for proportional, integral, and derivative that dampened a wing model's oscillation. parameters PID were found using a heuristic procedure that involved first locating the P gain value that resulted in the smallest MSE, then locating the I gain value that resulted in the smallest MSE when the P gain value was fixed, further finally locating the D gain value that resulted in the smallest MSE only when best values of P and I gain were fixed. During the particle optimization procedure, the parameters of PID were completed by deciding on a swarm size of 40, which was the optimal value found in prior studies by [42].

In a PID-PSO setup, the number of iterations is the number of times the PSO algorithm updates the particle locations and velocities, and the PID controller assesses the system's reaction [50].

To estimate the inaccuracy, the system was run in Simulink using function commands, with the initial gain values KP, KI, and KD set to 0. Previous studies were conducted to determine the optimal swarm size for the PID-PSO approach it was 40. The MSE method and three quantitative fitness indicators (ISE, IAE, and ITAE) were used to validate the system and compare the results. The response performance of the PID-PSO system, as well as the fitness and frequency performance based on ISE, were analyzed. the response performance of the PID-PSO system and the fitness and frequency performance based on ISE were examined.

Finally, the response performance of PID-PSO and the fitness and frequency performance depending on ITAE. The PSO MATLAB code as shown in Appendix B was used as it was compatible with block of PID controller as shown in Figure 0.3.

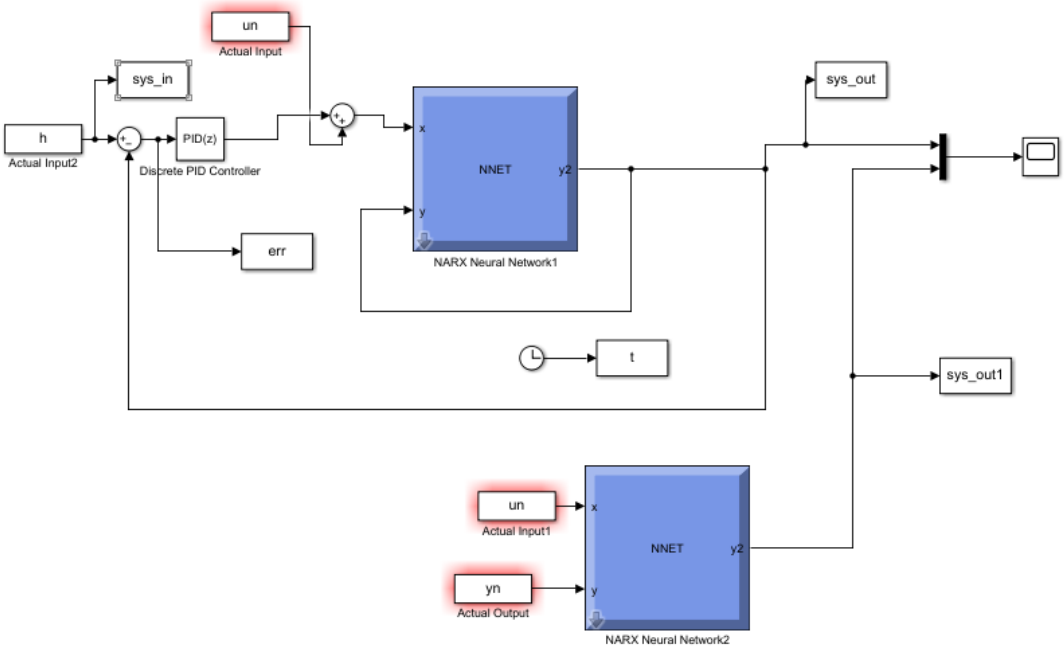

Figure 0.3. The system and PID-PSO controller block diagram for the NN-NARX model.

As shown Figure 5.4: For speeds of 10 m/s, 15 m/s, and 20 m/s, we have three separate data sets. Each data set consists of 300 rows, where the time measurements are combined with either the speed or vibration values in a two-column matrix.

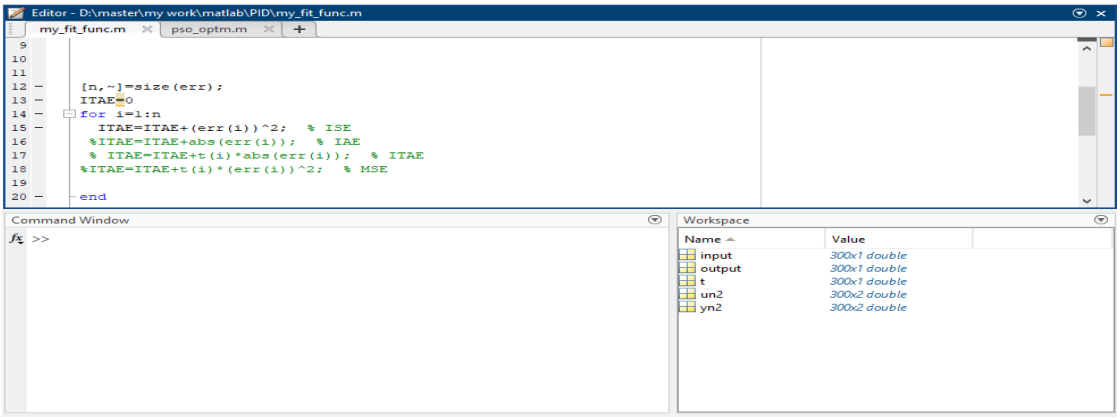

Figure 0.4. Initializing and entering data into the program.

We give the system a mixture velocity at a specific time and a specific wavelength, And NARX expects vibration and PID reducing vibration, and The PSO code starts with optimizing system properties as shown in Figure 5.5.

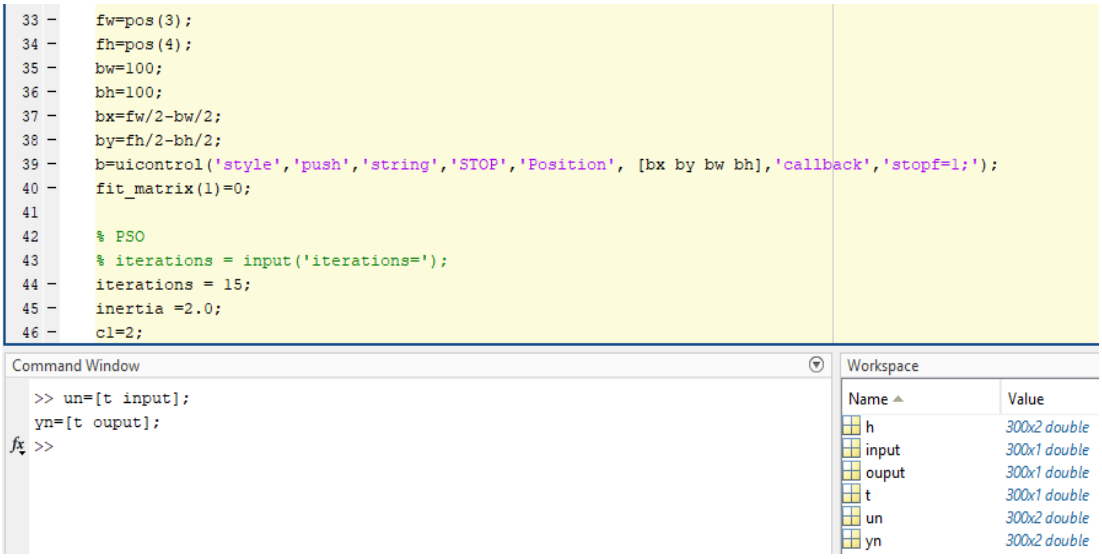

Figure 0.5. Initiate the coding process.

Figure 5.6: The optimization process for the PID system using the PSO algorithm displays and begins to run. By iteratively modifying the PID settings, the method seeks the minimum error rate within a certain tolerance. It tries out several settings for the parameters and adjusts them based on the current optimal answer. The algorithm will keep optimizing Until it reaches the nearest location from the determined point and the point by a zero matrix, with time being a critical factor in this process.

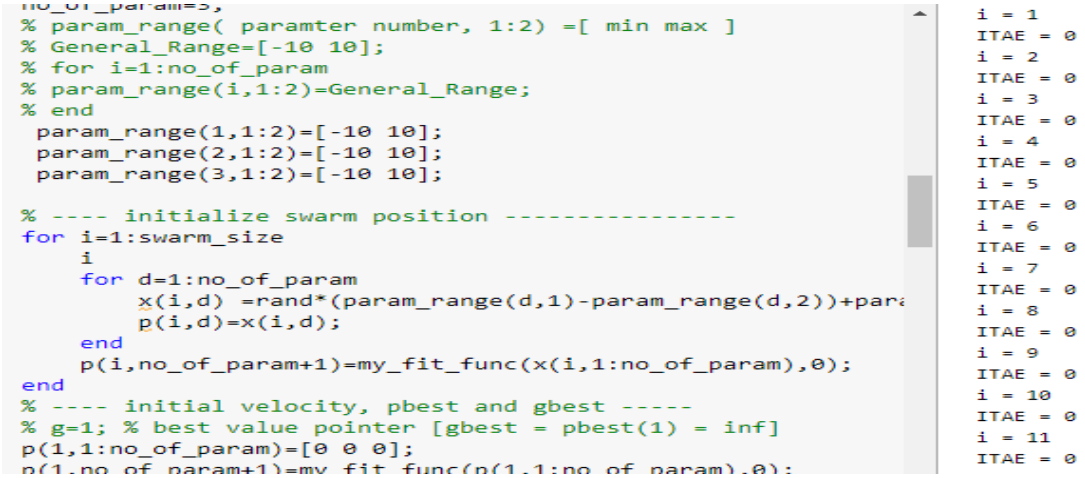

Figure 0.6. Particle Swarm Optimization.

In Figure 5.7 Visual representation of the results is provided through the use of matrices and four figures to display the results of the study. The performance-related variables and parameters have been computed and are stored in the matrices. The figures offer visual representations of the outcomes.

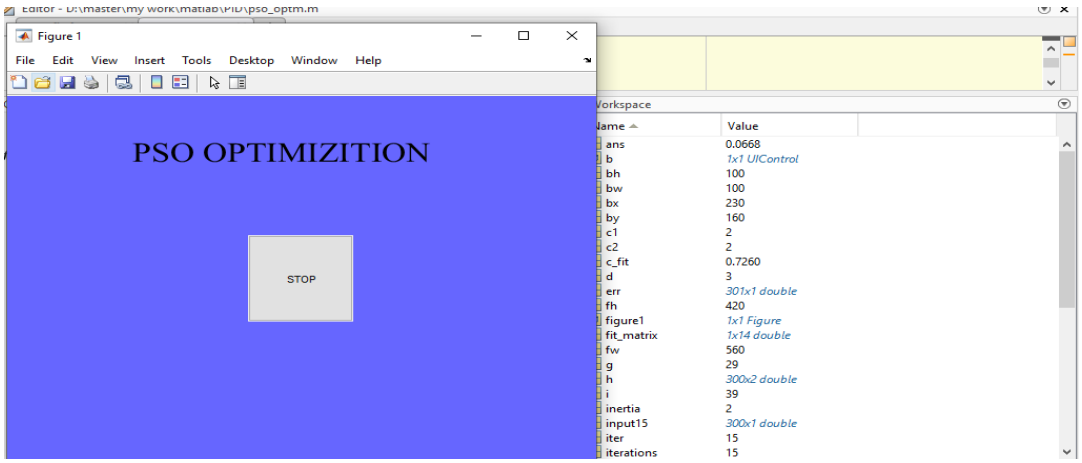

Figure 0.7. Terminate the optimization of work.

After optimizing the control system, Figure 5.8 displays the best K_matrix results at 10 m/s. Similarly, Figure 5.9 shows the optimal K_matrix at 15 m/s, highlighting the controller gains' role in system regulation. Additionally, Figure 5.10 presents successful outcomes, demonstrating how fine-tuning the controller gains optimizes stability, reduces vibrations, and improves performance at 20 m/s.

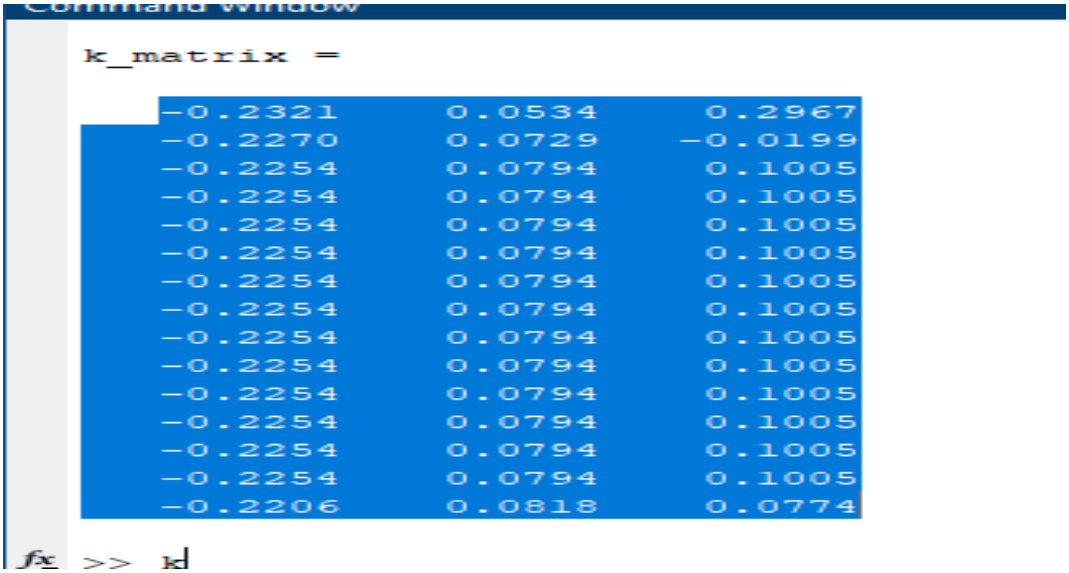

Figure 0.8. K_ matrix in 10 m/s.

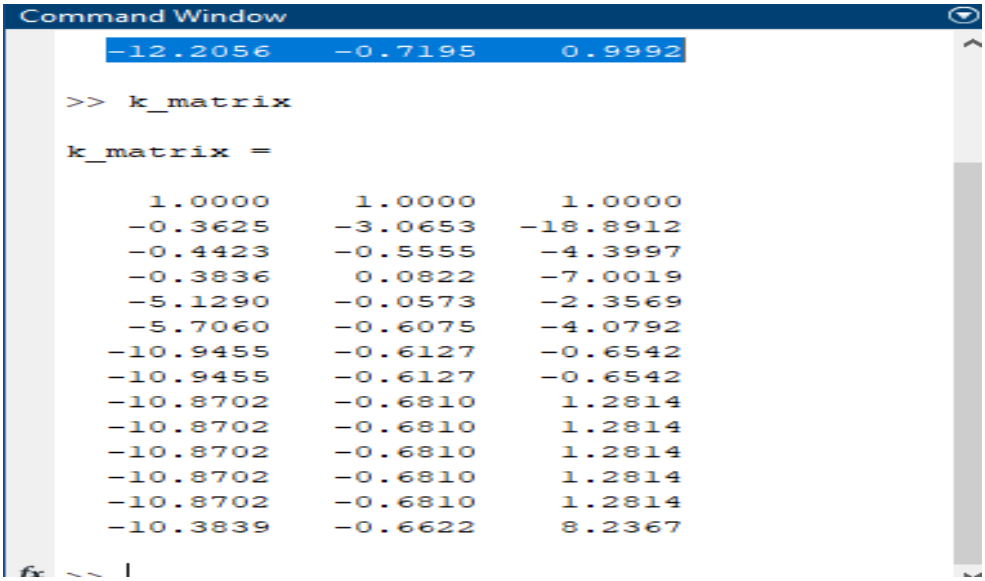

Figure 0.9. K_ matrix in 15 m/s.

```
>> k_matrix

k_matrix =

   -0.2505    0.2133    0.9847
   -0.2604    0.3232   -0.3362
   -1.0000    0.3000    0.1648
   -1.0000    0.3000    0.1648
   -1.0000    0.3622   -1.0000
   -1.0000    0.3514   -1.0000
   -1.0000    0.3250   -1.0000
   -1.0000    0.3250   -1.0000
   -1.0000    0.3254   -1.0000
   -1.0000    0.3254   -1.0000
   -1.0000    0.3256   -1.0000
   -1.0000    0.3256   -1.0000
   -1.0000    0.3256   -1.0000
   -1.0000    0.3258   -1.0000
   -1.0000    0.3258   -1.0000

fx >>
```

Figure 0.10. K_ matrix in 20 m/s.

5.5. MODEL ACTIVE VIBRATION CONTROL RESULTS

In this section, the most important results that we obtained are presented, and they include: Mean square error, the system's k_p, k_I, and k_D values, Vibration amplitude, and Vibration magnitude before and after control, Fitness value, the number of iterations, and The effectiveness of a PID-PSO can be evaluated by calculating the vibration reduction ratio. It is calculated by comparing the vibration levels before and after applying the PID-PSO at three velocities.

Table 0.1. PID-PSO parameters setting on the NN-NARX model.

Parameter	**Speed**	K_P	K_I	K_D	**MSE**
Value	10 m/s	-0.2206	0.0818	0.0774	0.0092
	15m/s	-12.205	-0.7195	0.9992	0.0668
	20 m/s	-1	0.3258	-1	0.0013

In Table 5.1: The system's k_p, k_I, and k_D values, as well as the Mean Square Error at each speed, are tabulated below.

5.5.1. Active Vibration Control at Speed 10 m/s

The Figure 0.11 illustrates how the PID-PSO control system may be used to effectively lessen vibration. The calculated vibration reduction ratio of 47.995 demonstrates the

substantial reduction in vibration amplitude attained with the use of the PID-PSO control strategy.

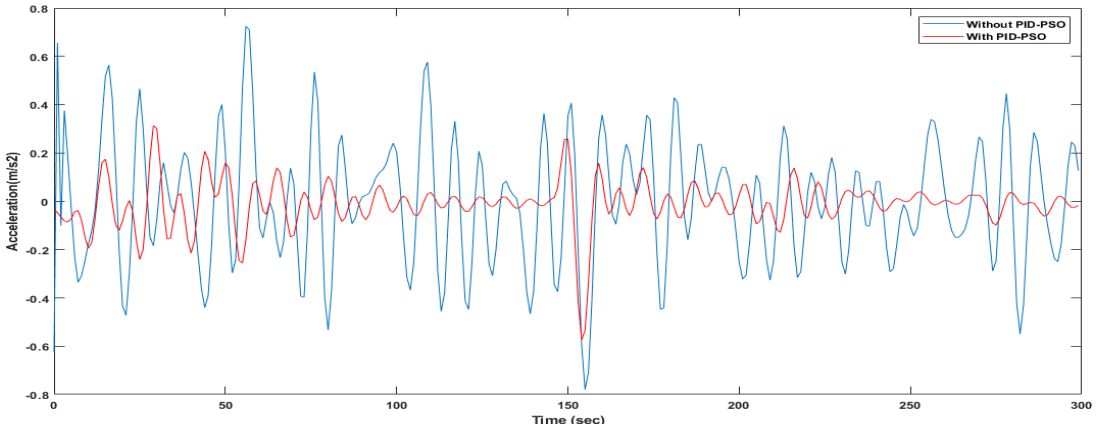

Figure 0.11 Normalized vibration amplitude with and without PID-PSO in 10 m/s.

The number of iterations required to achieve this reduction was 15, and the fitness value was ≅ 2.8. as shown in Figure 5.12

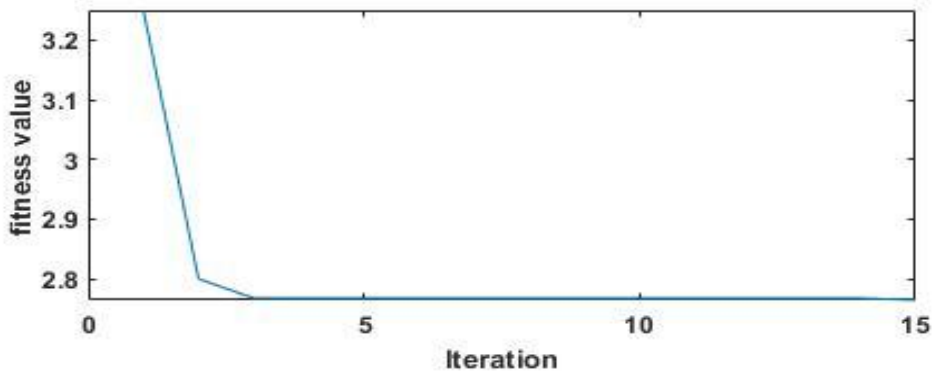

Figure 0.12 Fitness value based in 10 m/s.

The Figure 5.13 how a targeted strategy can significantly reduce the maximum magnitude of vibrations. When moving at 10 metres per second, the maximum magnitude of vibration decreased from 12.620 decibels at 13.33 hertz to 5.33 decibels at 9.88 hertz. This decrease in amplitude suggests that the applied method is effective in dampening vibration and may increase system performance as a whole.

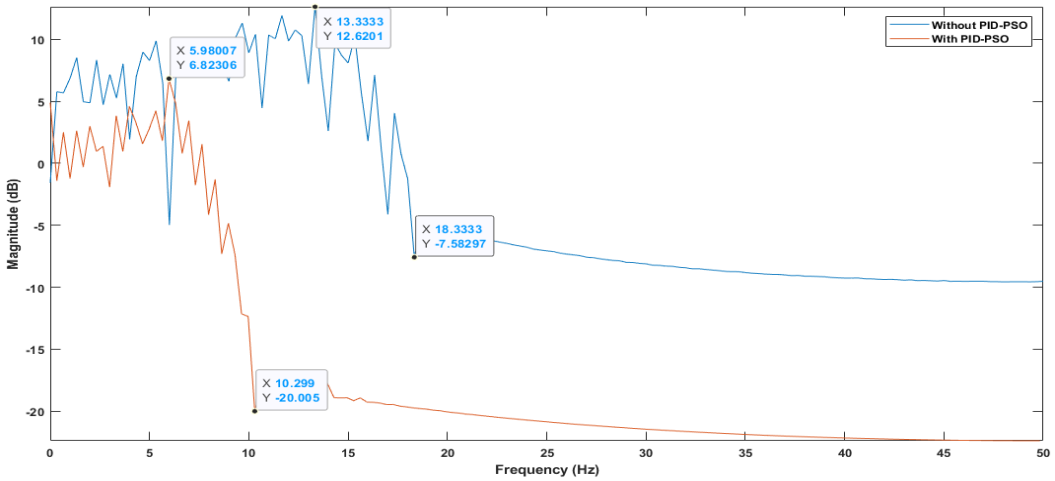

Figure 0.13 Frequency response with/without the controllers PID-PSO in10 m/s.

5.5.2. Active Vibration Control at Speed 15 m/s

The effect of using the PID-PSO control method on vibration amplitudes is shown in the figure. The blue line shows the amplitudes of the vibrations before PID-PSO was applied, and the red line shows the amplitudes of the vibrations after PID-PSO was applied. And the vibration reduction ratio was 44.837%, as shown in Figure 0.14.

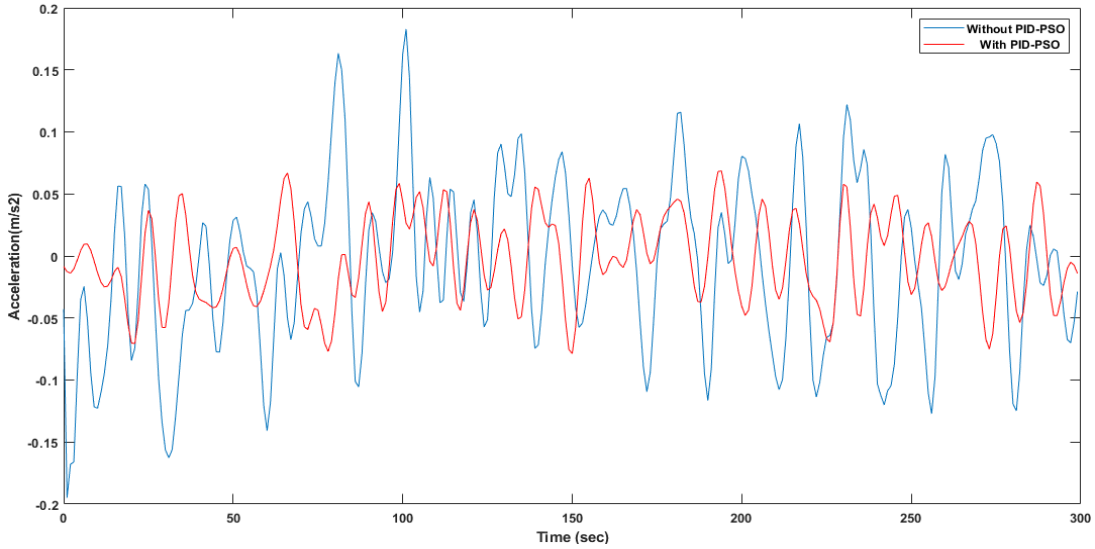

Figure 0.14. Normalized vibration amplitude with and without PID-PSO at speed 15 m/s.

In Figure 5.15 number of iterations required to achieve this reduction was 14, and the fitness value was ≅ 0.3.

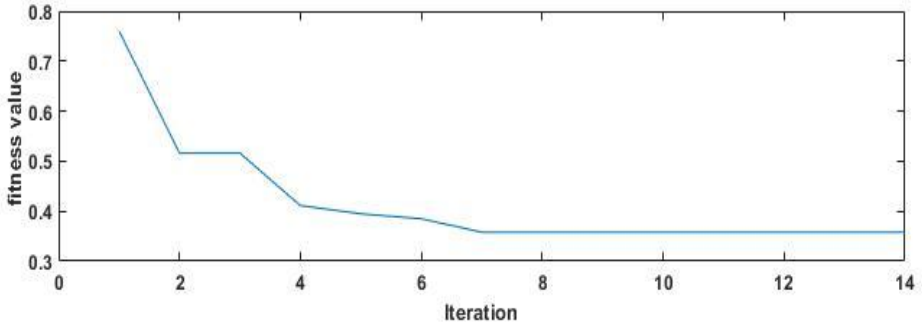

Figure 0.15. Fitness value based in 15 m/s.

The biggest vibration magnitude was reduced from 6.560 dB at 5.66 Hz to 2 dB at 5.7 Hz after implementing PID-PSO note in the Figure 0.16.

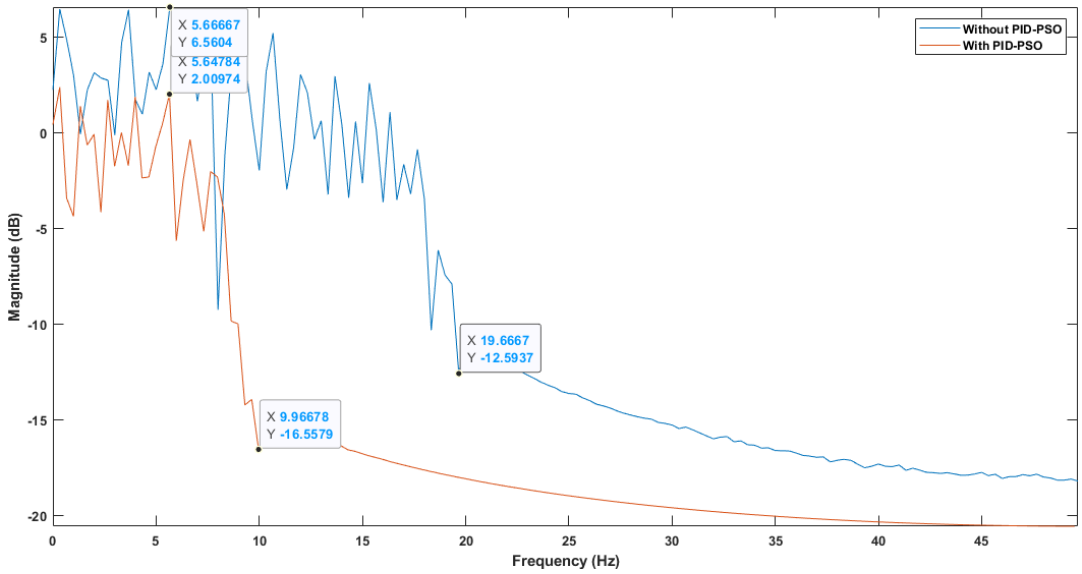

Figure 0.16. Frequency response with/without the controllers PID-PSO 15 m/s.

5.5.3. Active Vibration Control at Speed 20 m/s

Vibration amplitudes are shown in the Figure 5.17 to have decreased due to PID-PSO control. The blue line shows the amplitudes of the vibrations before PID-PSO was applied, and the red line shows the amplitudes of the vibrations after PID-PSO was applied. PID-PSO has been successful in reducing vibrations, as evidenced by the substantial decrease in levels. the calculated reduction in vibration ratio of 44.812%.

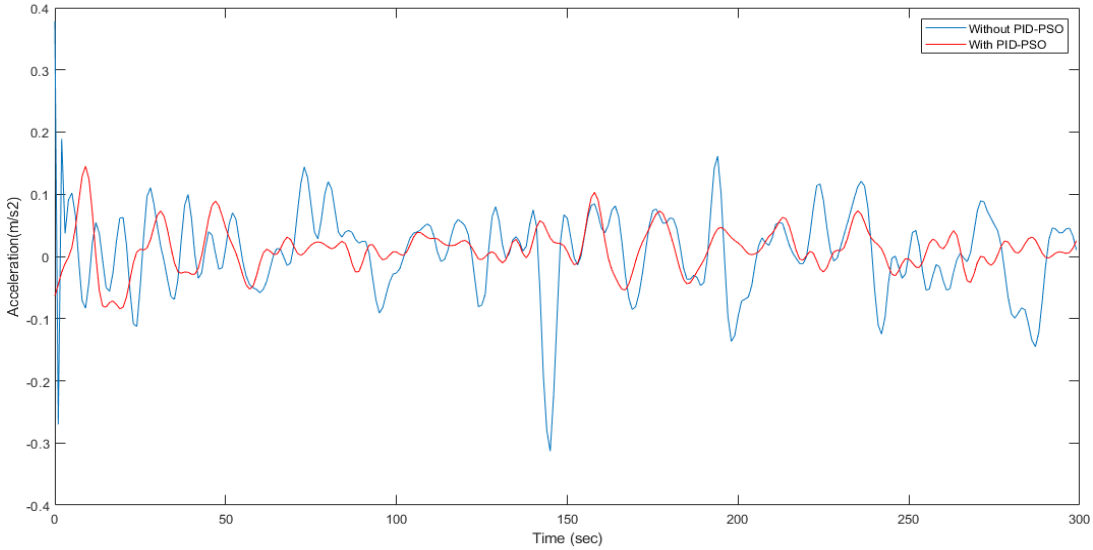

Figure 0.17 Normalized vibration amplitude with and without PI-PSO D in 20 m/s.

In Figure 5.18 Number of iterations to achieve this reduction was 15, and the fitness value was ≅ 0.4.

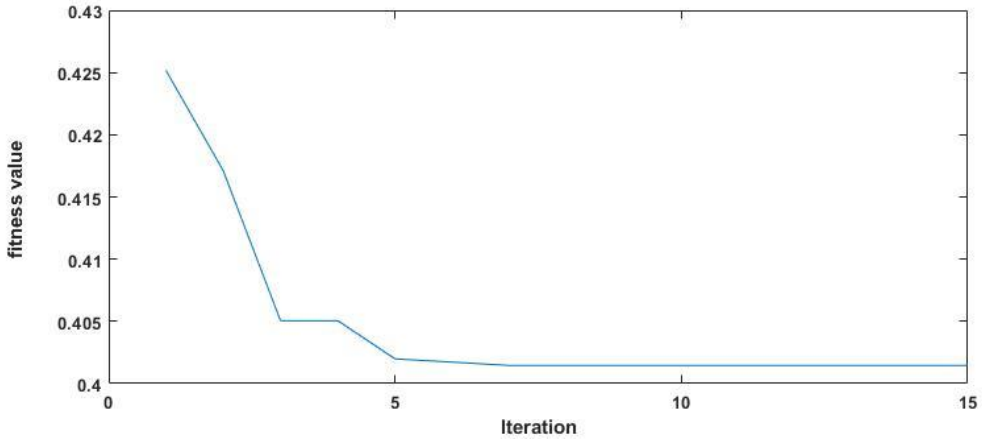

Figure 0.18. Fitness value based in 20 m/s.

Vibration levels were drastically reduced after switching to a PID-PSO control scheme. Successful damping of the biggest vibration reduced its magnitude from 6.38 dB at 2.66 Hz to 2.99 dB at 0.724 Hz. The results show that by using PID-PSO, an improved vibration profile was achieved, reducing the potential harm from increased vibration levels as shown in Figure 5.19.

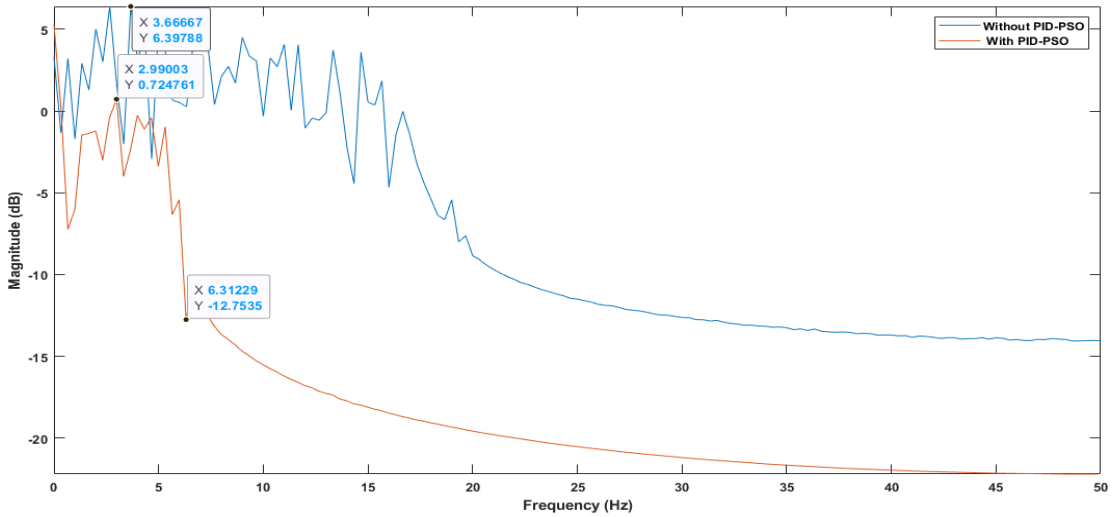

Figure 0.19. Frequency response with/without the controllers PID-PS in 20 m/s.

PART 6

CONCLUSION

6.1. SUMMARY

In this study, a suite was designed for wing NACA 2416; we have successfully manufactured an aileron model. Made of PLA using a 3D printer. Controlling the airflow with an inverter and monitoring the airspeed and vibration using sensors. The air is passed over the object at rates ranging from 10 to 20 m/s for a set amount of time. Collected data from sensors placed at the tip of the wing. Measured air velocity and vibration acceleration over a period of 10 seconds, resulting in 300 data points; preprocessed the collected data by filtering, resampling, or removing any noise or outliers. Ensured the data was properly scaled and formatted by a low pass filter for further analysis.

NARX model was constructed that incorporated the exogenous input (air velocity) and predicted the vibration acceleration at the wing tip. split the collected data into a training set(20% or 60 data), a validation set(60% or 180 data), and a testing set(20% or 60 data). the training set was used to estimate the parameters of the NARX model and fine-tune its structure. the MES can then be used to evaluate the model's performance.

Utilized SI, NARX, PID, PSO, and fitness evaluation to control the vibrations on a wing based on the measured air velocity and vibration-predicted data. implemented a PID controller to regulate the vibrations based on the predicted behavior from the NARX model. The PID controller adjusted control inputs according to the error between the desired and predicted vibration accelerations. used PSO as an optimization algorithm to optimize the PID controller gains. PSO searched for optimal or near-

optimal values of the PID gains that minimized a fitness function, allowing for the identification of the most suitable parameters for the PID controller.

Defined a fitness function that evaluated the performance of the PID controller based on the Mean Squared Error (MSE) between the desired and actual vibration accelerations. The MSE served as a metric to assess how effectively the PID controller was controlling the vibrations. The fitness function guided the PSO algorithm in searching for optimal PID gains by minimizing the MSE. applied the PSO algorithm to search for optimal PID gains that minimized the fitness function. The particles' positions and velocities were iteratively updated until convergence or a satisfactory solution was obtained. The resulting PID gains provided the control parameters for the vibration control system.

The natural frequency of the wing was also calculated, resulting in a vibration amplitude range of (-0.15 to 0.2 m/s^2) as shown in figure 3.10, and the largest vibration magnitude was 8.54 dB at 3.94 Hz as shown in figure 3.11.

At a speed of 10 m/s: Figure 3.12 displays the VIV amplitude range of (-1 to 0.8 m/s2), while figure 3.13 shows the largest vibration magnitude of 12.620 dB at 13.33 Hz. Using the NN-NRAX method, the mean squared error (MSE) was 0.0028 in NE = 4 and ND = 3, as shown in figure 4.10. Figure 4.11 displays the correspondence between the predicted and actual vibration amplitudes. After implementing PID-PSO to control vibration, the vibration reduction ratio was 47.995%, as shown in figure 5.11 . The number of iterations required to achieve this reduction was 15, and the fitness value was ≅ 2.8, as shown in figure 5.12, Table 5.1 shows that the MSE with controller gains of KP=-0.2206, KI=0.0818, and KD=0.0774 was 0.0092. Additionally, figure 5.13 displays the decrease in the largest vibration magnitude from 12.620 dB at 13.33 Hz to 5.33 dB at 9.88 Hz.

At a speed of 15 m/s: The wing resulted in a VIV amplitude range of (-0.2 to 0.2 m/s^2) as shown in figure 3.14, and the largest vibration magnitude was 6.560 dB at 5.66 Hz as shown in figure 3.15. Using the NN-NRAX method, the MSE was 0.000035217 in NE = 4 and ND = 7, as shown in figure 4.12. Figure 4.13 displays the correspondence

between the predicted and actual vibration amplitudes. After implementing PID-PSO to control vibration, the vibration reduction ratio was 44.837%, as shown in figure 5.14. The number of iterations required to achieve this reduction was 14, and the fitness value was ≅ 0.3, as shown in figure 5.15. Table 5.1 shows that the MSE with controller gains of KP=-12.205, KI=-0.7195, and KD=0.9992 was 0.0668. Additionally, figure 5.16 displays the decrease in the largest vibration magnitude from 6.560 dB at 5.66 Hz to 2 dB at 5.7 Hz.

In speed of 20 m/s: The VIV amplitude was found to range from -0.4 to 0.2 m/s^2, as shown in Figure 3.16. Additionally, the largest vibration magnitude was recorded at 2.66 Hz, as depicted in Figure 3.17. using the NN-NRAX method with an MSE of 0.00064992, NE = 4, and ND = 4. The corresponding error form and amount of correspondence between the predicted and actual for vibration amplitude by the neural network were shown in Figures 4.14 and 4.15, respectively. The results indicate that the neural network model accurately predicted the system's vibration amplitude. After applying the PID-PSO controller to control the vibration, the vibration reduction ratio was found to be 44.812%, and the vibration amplitude decreased significantly as depicted in Figure 5.17. The number of iterations to achieve this reduction was 15, and the fitness value was ≅ 0.4 as shown in Figure 5.18. The controller gains were KP = -1, KI = 0.3258, and KD = -1, with an MSE of 0.0013, as shown in Table 5.1.the largest vibration magnitude was reduced from 6.38 dB at 2.66 Hz to 2.99 dB at 0.724 Hz, as shown in Figure 5.19.

Based on modeling, the effect of an active vibration controller was studied on the suppression of vortex-induced vibration in a wing with a fixed spurt. The results showed that the proposed AVC achieved extremely good attenuation levels while maintaining several essential parameters. The primary goal of this research was to develop the best controller to suppress the attenuation of the undesired vibration on the aircraft wing system. The findings corroborated this aim.

Achieve the objectives of the research by implementing active control of the wing of the aircraft furthermore reducing the vibration significantly and improving the stability

of the wing and ensuring the suitability of the system and control using PID to the wing of the aircraft.

When applied to VIV problems in wings, the black box strategy of the NN-NARX model for executing the SI technique was novel. Validation and trustworthiness of the NN-NARX structural model were established. These findings confirm that the primary goal of this work, as indicated in Chapter One, is to use nonlinear SI techniques to represent the aircraft wing model's dynamic behavior. Black-box modeling of the vibrating system was accomplished using the SI method. Mathematical models for analyzing and optimizing vibration data gathered during the experimental activity were shown by tuning a proportional-integral-derivative (PID) controller using particle swarm optimization (PSO). It has also been shown that the system achieves its aims. The developed method is quite useful for dampening or removing wing vibrations.

6.2. FUTURE WORKS

1. The flow speed range generated by the Centrifugal fan used in this research was also limited. A higher range configuration of the disturbance wind tunnel system is recommended for future study.
2. A different type of material is also recommended to be used in making the wing to make it that bears higher pressure and has more flexibility include polymers like ABS and PETG (Polyethylene Terephthalate Glycol) (PETG).
3. In this study, only one controller (PID-PSO) was used to suppress the vibration. Other intelligent controllers, such as controller parameters with learning parameters setting (PID-ILA) as well as Fuzzy-PID Controller (FPID).
4. There is a need for further research on the effect Use other types of SI methods for example ant colony approach.
5. Experimental control, we can use an actuator such as a piezoelectric or control rod driven by DC motor that will be located behind the wing to break the vortices.

REFERENCES

[1] A. Basutkar, K. Baruah, and S. K. Kudari, "Frequency Analysis of Aircraft Wing Using FEM," ***Lect. Notes Mech. Eng.,*** **no. January**, pp. 527–533, doi: 10.1007/978-981-15-1124-0_46 (2020).

[2] D. J. Mead, "Passive vibration control," p. 540,: **https://www.wiley.com/en-us/Passive+Vibration+Control-p-9780471942030** (1998).

[3] D. Hodges, G. Pierce, and M. Cutchins, " I**ntroduction to Structural Dynamics and Aeroelasticity** ," *Appl. Mech. Rev.*, vol. 56, no. 3 , doi: 10.1115/1.1566393 (2003).

[4] H. Dowell, *A Modern Course in Aeroelasticity*. Springer International Publishing,. **https://books.google.com.tr/books?id=fppIEAAAQBAJ**(2021).

[5] H. A. Abdulameer and H. R. Wasmi, "**Vibration Control Analysis of Aircraft Wing by Using Smart Material**," vol. 6, no. 8, pp. 7–43, (2015).

[6] J. R. Banerjee, X. Liu, and H. Kassem, "Free vibration and flutter characteristic of high aspect ratio aircraft wing," (2013).

[7] T. Knight, A. Wimpenny, and A. He, "Elimination of vortex inducted vibration in sample probes and thermowells using helical strakes; a report on the development, testing and proving of a helical, **http://orbitalgas.com/wp-content/uploads/2017/01/Elimination_VIV_Sample_Probes_Thermowells.pdf (**2016**).**

[8] A. Baz and J. Ro, "Active control of flow-induced vibrations of a flexible cylinder using direct velocity feedback," ***J. Sound Vib.***, vol. 146, no. 1, pp. 33–45, (1991).

[9] N. Shaharuddin, "Active vibration control of transverse vibrating segmented marine riser." **PhD Thesis, Department of Applied Mechanics, Faculty of Mechanical** …, (2015).

[10] H. M. Blackburn, R. N. Govardhan, and C. H. K. Williamson, "A complementary numerical and physical investigation of vortex-induced vibration," ***J. Fluids Struct.***, vol. 15, no. 3–4, doi: 10.1006/jfls.2000.0345 (2001).

[11] M. M. Zdravkovich, "Review and classification of various aerodynamic and hydrodynamic means for suppressing vortex shedding," ***J. Wind Eng. Ind. Aerodyn.***, vol. 7, no. 2, pp. 145–189, doi: 10.1016/0167-6105(81)90036-2 (1981).

[12] F. M. Khaleel, I. A. Hasan, and M. J. Mohammed, “PV panel system modelling method based on neural network,” **in *AIP Conference Proceedings***, vol. 2386, no. 1, p. 40029 (2022).

[13] Y. Shirai, H. Arakawa, N. Toda, Y. Taneda, and K. Sakura, “Active Vibration Control for Aircraft Wing,” ***jsme Int. journal. ser. c, Dyn. Control. Robot. Des. Manuf.***, vol. 36, no. 3, doi: 10.1299/jsmec1993.36.319 (1993).

[14] C. C. Fuller, S. Elliott, and P. A. Nelson, *Active Control of Vibration*. Elsevier Science,. **https://books.google.com.tr/books?id=HGP4iGWhAdEC** (1996).

[15] C. H. K. Williamson, “Oblique and parallel modes of vortex shedding in the wake of a circular cylinder at low Reynolds numbers,” ***J. Fluid Mech.***, vol. 206, pp. 579–627, (1989).

[16] C. N. Hansen, *Understanding Active Noise Cancellation*. Taylor & Francis, **https://books.google.com.tr/books?id=zf7qaoBvZr4C** (2002).

[17] K. A. Markowski and C. I. Muresan, “Smart beam system: Identification and minimal realization using digraphs theory,” **in *2017 22nd International Conference on Methods and Models in Automation and Robotics*** *(MMAR)*, (2017).

[18] A. Preumont, *Vibration Control of Active Structures: An Introduction*. Springer Netherlands, **https://books.google.com.tr/books?id=9KGZDAEACAAJ**(2011).

[19] A. Mohammed, “FREE VIBRATION AND FLUTTER ANALYSIS OF HIGH ASPECT RATIO WINGS” (2008).

[20] Z. Hao, T. Wang, X. Cao, and Q. Zhang, “Design of eccentric mass-type vibrationdamping electric actuator control system for non-fixed-wing aircraft (August 2020),” ***IEEE Access***, vol. 8, doi: 10.1109/ACCESS.2020.3042854(2020).

[21] M. I. Babar, A. Javed, F. Mazhar, and R. F. Latif, “Experimental flutter analysis of the wing in pitch and plunge mode,” ***6th Int. Conf. Aerosp. Sci. Eng. ICASE 2019***, doi: 10.1109/ICASE48783.2019.9059148 (2019).

[22] L. Han, D. Wei, Y. Wang, and X. Zhang, “Vortex-induced vibration mechanism of the NACA 0012 airfoil based on a method of separating disturbances,” ***J. Sound Vib.***, vol. 501, p. 116044, doi: 10.1016/j.jsv.2021.116044(2021).

[23] C. Norberg, “Flow around a circular cylinder: aspects of fluctuating lift,” ***J. Fluids Struct.***, vol. 15, no. 3–4, pp. 459–469, (2001).

[24] B. M. Benner, D. W. Carlson, B. Seyed-Aghazadeh, and Y. Modarres-Sadeghi, “Vortex-Induced Vibration of symmetric airfoils used in Vertical-Axis Wind

Turbines," ***J. Fluids Struct.***, vol. 91, no. xxxx, p. 102577, 2019, doi: 10.1016/j.jfluidstructs.(2019).

[25] A. A. Ali, H. Y. Mahmood, and M. W. Saeed, "Active Vibration Control of Aircraft Wing Using Piezoelectric Transducers," ***Int. J. Sci. Eng. Res.***, vol. 7, no. 5, pp. 977–984, (2016).

[26] Z. Qin, "Vibration and aeroelasticity of advanced aircraft wings modeled as thin-walled beams: Dynamics, stability and control." **Virginia Polytechnic Institute and State University**, (2001).

[27] S. Pinho, "Vibration of an aircraft model lab handout," no. May 2020, doi: 10.13140/RG.2.2.16847.61607 (2020).

[28] S. N. Kane, A. Mishra, and A. K. Dutta, "Preface: International Conference on Recent Trends in Physics (ICRTP 2016)," ***J. Phys. Conf. Ser.***, vol. 755, no. 1, 2016, doi: 10.1088/1742-6596/755/1/011001 (2016).

[29] S. A. El-Serafi, M. H. Eissa, H. M. El-Sherbiny, and T. H. El-Ghareeb, "Comparison between passive and active control of a non-linear dynamical system," ***Jpn. J. Ind. Appl. Math.***, vol. 23, no. 2, pp. 139–161, doi: 10.1007/BF03167548(2006).

[30] M. S. Saad, H. Jamaluddin, and I. Z. M. Darus, "Implementation of PID controller tuning using differential evolution and genetic algorithms," ***Int. J. Innov. Comput. Inf. Control***, vol. 8, no. 11, pp. 7761–7779, (2012).

[31] S. L. Patil, H. J. Tantau, and V. M. Salokhe, "Modelling of tropical greenhouse temperature by auto regressive and neural network models," ***Biosyst. Eng.***, vol. 99, no. 3, pp. 423–431, (2008).

[32] I. Z. M. Darus and Z. A. Lokaman, "Dynamic modelling of twin rotor multi system in horizontal motion," ***J. Mek.***, (2010).

[33] D. Gómez Pizano, "Comparison of frequency response and neural network techniques for system identification of an actively controlled structure," *Dyna*, vol. 78, no. 170, pp. 79–89, (2011).

[34] N. M. R. Shaharuddin and I. Z. Mat Darus, "Active vibration control of marine riser," *Proc. **2012 IEEE Conf. Control. Syst. Ind. Informatics, ICCSII 2012,*** no. September 2015, pp. 114–119, 2012, doi: 10.1109/CCSII.2012.6470484(2015).

[35] N. M. R. Shaharuddin and I. Z. Mat Darus, "Fuzzy-PID control of transverse vibrating pipe due to vortex induced vibration," *Proc. - **UKSim 15th Int. Conf. Comput. Model. Simulation**, UKSim 2013*, no. April, pp. 21–26, 2013, doi: 10.1109/UKSim.2013.134(2013).

[36] N. M. R. Shaharuddin and I. Z. Mat Darus, "System identification of flexibly mounted cylindrical pipe due to vortex induced vibration," ***IEEE Symp. Comput. Informatics, Isc. 2013***, no. April, pp. 30–34, 2013, doi: 10.1109/ISCI.2013.6612370 (2013).

[37] L. B. Mohammed, M. A. Hamdan, E. A. Abdelhafez, and W. Shaheen, "Hourly solar radiation prediction based on nonlinear autoregressive exogenous (narx) neural network," ***Jordan J. Mech. Ind. Eng***., vol. 7, no. 1, (2013).

[38] T. A. Tahseen, M. Ishak, and M. M. Rahman, "Performance predictions of laminar heat transfer and pressure drop in an in-line flat tube bundle using an adaptive neuro-fuzzy inference system (ANFIS) model," ***Int. Commun. Heat Mass Transf***., vol. 50, pp. 85–97, (2014).

[39] E. Yazid, M. S. Liew, S. Parman, and V. J. Kurian, "Estimation of Response Transfer Functions of Offshore Structures Using the Time-Varying ARX Model," **in** ***ISOPE International Ocean and Polar Engineering Conference***, 2013, p. ISOPE-I(2013).

[40] M. A. Hamdan, H. R. A. Khalil, and E. A. M. Abdelhafez, "Comparison of neural network models in the estimation of the performance of solar still under jordanian climate," ***J. Clean Energy Technol***., vol. 1, no. 3, pp. 238–242, (2013).

[41] T. G. Ling, M. F. Rahmat, and A. R. Husain, "System identification of electro-hydraulic actuator system using ANFIS approach," ***J. Teknol.(Sciences Eng.),*** vol. 67, no. 5, pp. 41–47, (2014).

[42] M. J. Mohammed and I. Z. M. Darus, "Discrete Time PID Controller on Vortex Induced Vibration for Marine Risers Based on Neural Network Identification Model," **in** ***Proceedings of the 2014 First International Conference on Systems Informatics, Modelling and Simulation***, pp. 14–19 (2014).

[43] S. Gao and J. Liu, "Adaptive neural network vibration control of a flexible aircraft wing system with input signal quantization," ***Aerosp. Sci. Technol.***, vol. 96, p. 105593, doi: 10.1016/j.ast.2019.105593(2020).

[44] S. M. Khot, N. P. Yelve, R. Tomar, S. Desai, and S. Vittal, "Active vibration control of cantilever beam by using PID based output feedback controller," ***J. Vib. Control,*** vol. 18, no. 3, pp. 366–372, (2012).

[45] H. Mohd Khair, K. Aishwarya, A. R. Ribhan Zafira, and A. Siti Anom, "Design a PID controller for a constant speed of combustion engine," ***Aust. J. Basic Appl. Sci.***, vol. 5, no. 12, pp. 1586–1593, (2011).

[46] H. Alimohammadi, B. B. Alagoz, A. Tepljakov, K. Vassiljeva, and E. Petlenkov, "A NARX model reference adaptive control scheme: Improved disturbance rejection fractional-order PID control of an experimental magnetic levitation system," ***Algorithms***, vol. 13, no. 8, doi: 10.3390/A13080201(2020).

[47] M. I. Solihin, L. F. Tack, and M. L. Kean, “Tuning of PID controller using particle swarm optimization (PSO),” **in *Proceeding of the international conference on advanced science, engineering and information technology***, vol. 1, no. 11, pp. 458–461(2011).

[48] B. Nagaraj and N. Murugananth, “A comparative study of PID controller tuning using GA, EP, PSO and ACO,” **in *2010 International Conference On Communication Control And Computing Technologies*,** pp. 305–313 (2010).

[49] H. M. Yatim and I. Z. Mat Darus, “Self-tuning active vibration controller using particle swarm optimization for flexible manipulator system,” ***WSEAS Trans. Syst. Control,*** vol. 9, no. 1, pp. 55–66, (2014).

[50] H. E. A. Ibrahim, F. N. Hassan, and A. O. Shomer, “Optimal PID control of a brushless DC motor using PSO and BF techniques,” ***Ain Shams Eng. J***., vol. 5, no. 2, pp. 391–398, (2014).

[51] Vishal and J. Ohri, “GA tuned LQR and PID controller for aircraft pitch control,” ***India Int. Conf. Power Electron***. *IICPE*, vol. 2015-May, , doi: 10.1109/IICPE.2014.7115839(2015).

[52] A. Ur Rehman, M. U. Khan, M. Z. H. Ali, M. S. Shah, M. F. Ullah, and M. Ayub, “Stability enhancement of commercial boeing aircraft with integration of PID controller,” ***ICAEM2021-2021Int.Conf.Appl.Eng.Math.Proc***.,pp.43–48,doi: 10.1109/ICAEM53552.2021.9547186(2021).

[53] D. Izci, S. Ekinci, A. Demiroren, and J. Hedley, “HHO Algorithm based PID Controller Design for Aircraft Pitch Angle Control System,” ***HORA 2020 - 2nd Int. Congr. Human-Computer Interact. Optim***. *Robot. Appl. Proc.*, pp. 5–10,doi: 10.1109/HORA49412.2020.9152897(2020).

[54] “Eclipson EWW180 - Printable flying wing.”

[55] “NACA 4 digit airfoil generator (NACA 2416 AIRFOIL).” http://airfoiltools.com/airfoil/naca4digit?MNaca4DigitForm%5Bcamber%5D=2&MNaca4DigitForm%5Bposition%5D=40&MNaca4DigitForm%5Bthick%5D=16&MNaca4DigitForm%5BnumPoints%5D=81&MNaca4DigitForm%5BcosSpace%5D=0&MNaca4DigitForm%5BcosSpace%5D=1&MNaca4DigitForm%5Bclo

[56] I. Z. Mat Darus, “Soft computing adaptive Vibration control of flexible structures.” **Ph. D. Thesis, Department of Automatic Control and System Engineering**, (2004).

[57] I. Z. M. Darus and M. O. Tokhi, “Soft computing-based active vibration control of a flexible structure,” ***Eng. Appl. Artif. Intell.***, vol. 18, no. 1, pp. 93–114, doi: 10.1016/j.engappai.2004.08.017(2005).

[58] M. Ataalah, I. A. Hasan, and M. J. Mohammed, “An intelligent modeling of

photovoltaic comparison among NAR, NARX, and nonlinear," **in *AIP Conference Proceedings***, vol. 2386, no. 1, p. 40033 (2022).

[59] I. Z. M. Darus and A. A. M. Al-Khafaji, "Non-parametric modelling of a rectangular flexible plate structure," ***Eng. Appl. Artif. Intell.***, vol. 25, no. 1, pp. 94–106, (2012).

[60] L. J. Wei, "The system identification of HVAC using artificial neural network." **Master of Engineering, Dept. Mechanical Engineering, University Technology**, (2012).

[61] M. J. Mohammed, "Discrete Time PID Controller on Vortex Induced Vibration for Marine Risers Based on Neural Network Identification Model,"doi: 10.1109/SIMS.2014.13(2014).

[62] S. Z. M. Hashim, M. O. Tokhi, and I. Z. M. Darus, "Nonlinear dynamic modelling of flexible beam structures using neural networks," ***Proc. IEEE Int. Conf. Mechatronics 2004****, ICM'04*, pp. 171–175, 2004, doi: 10.1109/icmech.(2004).

[63] H. Asgari, X. Chen, and R. Sainudiin, "Applications of artificial neural networks (ANNs) to rotating equipment," (2011).

[64] Y. T. Zhou, J. Bin Nie, N. Han, C. Chen, and Z. F. Yue, "Study on PID parameters tuning based on particle swarm optimization," **in *Advanced Materials Research***, vol. 823, pp. 432–438(2013).

[65] M. Clerc, "The swarm and the queen: towards a deterministic and adaptive particle swarm optimization," **in *Proceedings of the 1999 congress on evolutionary computation-CEC99*** *(Cat. No. 99TH8406)*, vol. 3, pp. 1951–1957(1999).

[66] H. He, J.-Z. Zhou, H. Lei, C.-S. Li, and L. Yang, "Research on fuzzy-PID excitation controller of synchronous generator based on improved PSO algorithm," **in *2009 International Conference on Machine Learning and Cybernetics***, vol. 2, pp. 770–775 (2009).

APPENDIX A

A.1 ARDUINO (NANO)

```
/MS4525DO
#include <Wire.h>   //I2C library 0x28H
byte fetch_pressure(unsigned int *p_Pressure); //convert value to byte data type
//Smoothing
const int numReadings = 20;
int readings[numReadings];      // the readings from the analog input
int readIndex = 0;              // the index of the current reading
float total = 0;                // the running total
float average = 0;              // the average
#define TRUE 1
#define FALSE 0
#include "FrSkySportSensor.h"
#include "FrSkySportSensorAss.h"
#include "FrSkySportTelemetry.h"
#if !defined(TEENSY_HW)
#include "SoftwareSerial.h"
#endif
FrSkySportSensorAss ass; // Create ASS sensor with default ID
#ifdef POLLING_ENABLED
FrSkySportTelemetry telemetry(true); // Create telemetry object with polling
#else
FrSkySportTelemetry telemetry; // Create telemetry object without polling
#endif
void setup()
{
 //MS4525DO
 Wire.begin();
 Serial.begin(9600);
 //delay(500);
 //Smoothing
 for (int thisReading = 0; thisReading < numReadings; thisReading++) {
  readings[thisReading] = 0;
 }
```

```
  // Configure the telemetry serial port and sensors (remember to use & to specify a pointer to sensor)
#if defined(TEENSY_HW)
  telemetry.begin(FrSkySportSingleWireSerial::SERIAL_3, &ass);
#else
  telemetry.begin(FrSkySportSingleWireSerial::SOFT_SERIAL_PIN_12, &ass);
#endif
}
void loop()
{
  MS4525DO ();
  // Set airspeed sensor (ASS) data
  ass.setData(average);  // Airspeed in km/h
#ifdef POLLING_ENABLED
  // Set receiver data to be sent in case the polling is enabled (so no actual receiver is used)
  telemetry.setData(90,    // RSSI value (0-100, 0 = no telemetry, 100 = full signal)
                    4.9);  // RxBatt (voltage supplied to the receiver) value in volts (0.0-13.2)
#endif
```

A.2 Arduino (MEGA) CODE

```
  // Send the telemetry data, note that the data will only be sent for sensors
  // that are being polled at given moment
  telemetry.send();
}
byte MS4525DO () {
  byte _status;
  unsigned int P_dat = 0;
  unsigned int T_dat;
  double PR;
  double V;
  double VV;
```

```
  _status = fetch_pressure(&P_dat);
  PR = (double)((P_dat - 900) / (14744.7)) ; //((P_dat - 819.15) / (14744.7));
  PR = (PR - 0.49060678) ; //(PR - 0.49060678)
  PR = abs(PR);
  V = ((PR * 13789.5144) / 1.225); //((PR * 13789.5144) / 1.225);
  VV = (sqrt((V)));
  //Smoothing
  // subtract the last reading:
  total = total - readings[readIndex];
  // read from the sensor:
  readings[readIndex] = VV;
  // add the reading to the total:
  total = total + readings[readIndex];
  // advance to the next position in the array:
  readIndex = readIndex + 1;
  // if we're at the end of the array...
  if (readIndex >= numReadings) {
    // ...wrap around to the beginning:
    readIndex = 0;
  }
  // calculate the average:
  average = total / numReadings;
  // send it to the computer as ASCII digits
  int x = average + 7;
  Serial.print("speed m/s :");
  Serial.println(x);
}
byte fetch_pressure(unsigned int *p_P_dat) {
  byte address, Press_H, Press_L, _status;
  unsigned int P_dat;
  address = 0x28;
  Wire.beginTransmission(address);
  Wire.endTransmission();
```

```
  //delay(10);
  Wire.requestFrom((int)address, (int) 4);//Request 4 bytes need 4 bytes are read
  Press_H = Wire.read();
  Press_L = Wire.read();
  Wire.endTransmission();
  _status = (Press_H >> 6) & 0x03;
  Press_H = Press_H & 0x3f;
  P_dat = (((unsigned int)Press_H) << 8) | Press_L;
  *p_P_dat = P_dat;
}
```

A.3 CODE TO CONVERT AMPLITUDE TO MAGNITUDE

```
clc
% Import the h a variable called 'values'
 t=1:2;
 ite=(length(1:301));
dt=20/ite;
time=dt:dt:20;
figure(1);plot(time, h)
xlabel('Time (second)','FontWeight','bold');
% Create ylabel
ylabel('Vibration Amplitude (cm)','FontWeight','bold');
% Create title
title('VIV Response at Ur=7.728','FontWeight','bold');
grid;
% Load Example Data
signal = h;
N = length(signal);
fs = 100; % 62.5 samples per second
fnyquist = fs/2; %Nyquist frequency
X_mags = abs(fft(signal));
bin_vals = [0 : N-1];
```

```
fax_Hz = bin_vals*fs/N;
N_2 = ceil(N/2);
figure(2);plot(fax_Hz(1:N_2), 10*log10(X_mags(1:N_2)))
xlabel('Frequency (Hz)','FontWeight','bold');
% Create ylabel
ylabel('Magnitude (dB)','FontWeight','bold');
% Create title
title('Single-sided Magnitude spectrum (Hertz)','FontWeight','bold');
axis tight
grid
```

A.4 PSO CODE

```
%% Initialization
% Parameters
clc
% Import the ouput.mat
% Import the  input.mat
% Import the h
% Import the t
%Normalising input
%utk masukkan dalam simulin utk buat validation\
un=[t' input(1:300)];
yn=[t' ouput(1:300)];
%utk masukkan dalam simulin utk buat validation\
% User Interface
stopf = 0;
figure1 = figure('Color',[0.4 0.4 1]);
annotation(figure1,'textbox',...
    [0.2 0.7 1 0.2],...
    'String',{'PSO OPTIMIZITION'},...
    'FontSize',24,...
    'FontName','Times New Roman',...
```

```
    'LineStyle','none');
pos= get(figure1,'Position');
fw=pos(3);
fh=pos(4);
bw=100;
bh=100;
bx=fw/2-bw/2;
by=fh/2-bh/2;
b=uicontrol('style','push','string','STOP','Position', [bx by bw bh],'callback','stopf=1;');
fit_matrix(1)=0;

% PSO
% iterations = input('iterations=');
iterations = 15;
inertia =2.0;
c1=2;
c2=2;
swarm_size =40;
no_of_param=3;
% param_range( paramter number, 1:2) =[ min max ]
% General_Range=[-10 10];
% for i=1:no_of_param
% param_range(i,1:2)=General_Range;
% end
 param_range(1,1:2)=[-10 10];
 param_range(2,1:2)=[-10 10];
 param_range(3,1:2)=[-10 10];

% ---- initialize swarm position ----------
for i=1:swarm_size
    i
    for d=1:no_of_param
        x(i,d) =rand*(param_range(d,1)-param_range(d,2))+param_range(d,2);
```

```
        p(i,d)=x(i,d);
    end
    p(i,no_of_param+1)=my_fit_func(x(i,1:no_of_param),0);
end
% ---- initial velocity, pbest and gbest -----
% g=1; % best value pointer [gbest = pbest(1) = inf]
p(1,1:no_of_param)=[1 1 1];
p(1,no_of_param+1)=my_fit_func(p(1,1:no_of_param),0);
% [~, g] = min(p(:,no_of_param+1));
g=1;
toggle_sw=0;
% p(1:swarm_size,no_of_param+1)=inf; %pbest=inf
v(1:swarm_size,1:no_of_param)=0; % initial velocity

%% Iterations
for iter = 1 : iterations
    %--- evaluating position --------
    for i=1:swarm_size
        for d=1:no_of_param
            x(i,d)=x(i,d)+v(i,d)/1.5;

%             %Limits
            if x(i,d)>param_range(d,2)
                x(i,d)=param_range(d,2);
            end
            if x(i,d)<param_range(d,1)
                x(i,d)=param_range(d,1);
            end

        end

        c_fit=my_fit_func(x(i,1:no_of_param),0);
        if c_fit<p(i,no_of_param+1)
```

```
    p(i,:)=[x(i,1:no_of_param) c_fit];
  end
 clc


  drawnow
  if stopf==1
    disp('STOP Request')
  end
  disp('current particle')
  disp('============================')
  disp ([num2str(x(i,:))])
  disp('# of particle          Fitness')
  disp('============================')
  disp ([num2str(i) '              '  num2str(c_fit)])
  disp('Best particle')
  disp('============================')
  disp ([p(g,1:no_of_param)])
  disp('Iteration          Best Fitness')
  disp('============================')
  disp ([num2str(iter) '              '  num2str(p(g,no_of_param+1))])


end
%--- global best position --------
[~, g] = min(p(:,no_of_param+1));
c_fit=my_fit_func(x(g,1:no_of_param),1)
fit_matrix(iter)=p(g,no_of_param+1);
k_matrix(iter,1:no_of_param)=p(g,1:no_of_param);
%--- updating velocity vectors----
for i=1:swarm_size
  for d=1:no_of_param
```

```
        v(i,d)=rand*inertia*v(i,d) + c1*rand*(p(i,d) - x(i,d)) + c2*rand*(p(g,d) -
x(i,d));
      end
   end
   if stopf==1
      break
   end
   figure(2)
   plot(1:iter,fit_matrix)
   if toggle_sw==0
save('my_pso_param0.mat','p','v','k_matrix','fit_matrix')
toggle_sw=1;
   else
      save('my_pso_param1.mat','p','v','k_matrix','fit_matrix')
    toggle_sw=0;
   end
end
k=p(g,1:no_of_param)

c_fuit=my_fit_func(k,1);
```

A.4 CODE TO DRAW THE REQUIRED FIGURE

```
function ITAE=my_fit_func(k,plotfig)
assignin('base', 'k',k)
sim('had20.slx')
%utk masukkan dalam simulin utk buat validation\
[n,~]=size(err);
ITAE=0
for i=1:n
 ITAE=ITAE+(err(i))^2;  % ISE
 %ITAE=ITAE+abs(err(i));  % IAE
 % ITAE=ITAE+t(i)*abs(err(i));  % ITAE
```

```
%ITAE=ITAE+t(i)*(err(i))^2;  % MSE

end
if plotfig
   figure(3)
   plot(t(1:300),sys_in(1:300),t(1:300),sys_out(1:300))
end
if plotfig
   figure(4)
   plot(t(1:300),sys_out1(2:301),t(1:300),sys_out(2:301),'r')
end
%ITAE=ITAE/t(n);  % MSE
```

APPENDIX B

B.1 THE ENDER-3

The Ender-3, 3D printer manufactured by Creality, is a popular choice for hobbyists and beginners due to its affordability, reliability, and versatile capabilities using the Fused Deposition Modeling (FDM) technology. This printer offers a build volume of 220mm x 220mm x 250mm, providing sufficient space for most hobbyist 3D printing projects. The Ender-3 features a manual bed leveling system that enables users to adjust the bed corners using a knob to achieve a level surface, which is crucial for successful 3D printing. Additionally, the Ender-3 has compatibility with various filament materials, including PLA, ABS, PETG, and others, making it a versatile tool for various printing applications.

The Ender-3 firmware is open-source, which means that users can customize it as needed, allowing for a more tailored experience. The printer also features high upgradability, with numerous aftermarket parts and accessories available to improve performance and functionality.

In summary, the Ender-3 offers hobbyists and beginners an affordable, reliable, and versatile 3D printing option. The manual bed leveling system, filament compatibility, open-source firmware, and upgradability make it a preferred choice for those seeking to engage in 3D printing projects.

Figure Appendix B 1. Ender-3, 3D printer

B.2 THE ANEMOMETER PROSKIT (MT-4615)

The Anemometer Proskit (MT-4615) is a handheld and portable device used for measuring wind speed. It is capable of measuring wind speeds ranging from 0.4 to 40 meters per second (m/s) with an accuracy of ±3%. The device is equipped with a large LCD display screen that can display the current wind speed reading in different units, including meters per second (m/s), kilometers per hour (km/h), feet per minute (ft/min), miles per hour (mph), or knots (nautical miles per hour).

In addition to measuring wind speed, the Proskit (MT-4615) Anemometer also has the capability to measure wind chill temperature and record maximum and average wind speed readings. The device is powered by a 9V battery and is commonly used in various fields, including weather monitoring, outdoor sports, and HVAC (heating, ventilation, and air conditioning) system testing and maintenance.

Overall, the Anemometer Proskit (MT-4615) is a reliable and user-friendly tool for measuring wind speed and related parameters. Its portability and versatility make it a popular choice for professionals in a variety of fields.

Figure Appendix B 2. The Anemometer Proskit (MT-4615)

B.3 AN INVERTER

An inverter is an electronic device that converts direct (DC) power to alternating (AC) power. This process allows for the powering of household appliances and electronic devices using DC power from sources such as solar panels or batteries. Inverters are commonly used in locations without access to a traditional power grid, as well as in vehicles, boats, and RVs for powering appliances on the go. They can also serve as backup power sources during power outages and other emergencies. There are different types of inverters, including pure sine wave, modified sine wave, and square wave inverters.

Figure Appendix B 3 An inverter

B.4 PITOT-STATIC TUBE

A Pitot-static tube is an instrument used in fluid mechanics and aviation to measure fluid velocity by detecting the pressure difference between the total pressure and the static pressure. It consists of a Pitot tube that measures the total pressure by facing directly into the fluid flow and one or more holes on the side of the tube facing perpendicular to the fluid flow, which measure the static pressure. By subtracting the static pressure from the total pressure, the dynamic pressure can be determined, which is directly proportional to the fluid velocity. The Pitot-static tube is commonly used to measure airspeed and flow rates in various industrial applications, including pipes and ducts.

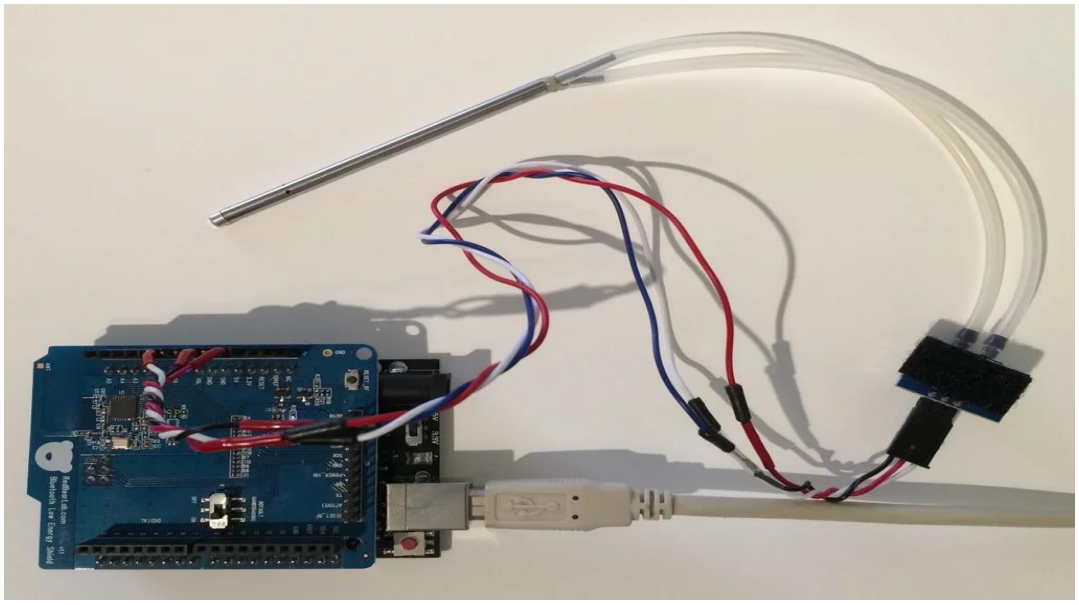

Figure Appendix B 4. Pitot-static tube

B.5 INTERFACE ACCELEROMETER MPU6050

The MPU6050 is an IC commonly used in electronics, robotics, and drones to measure motion and orientation. The chip contains both an accelerometer and a gyroscope, and is interfaced using the I2C communication protocol with a microcontroller or a digital device. The microcontroller sends commands to configure the MPU6050 and to retrieve sensor data. The accelerometer data provides information on the device's tilt and acceleration in three dimensions, whereas the gyroscope data provides data on its rotation. Combining these data allows for accurate motion tracking and orientation information.

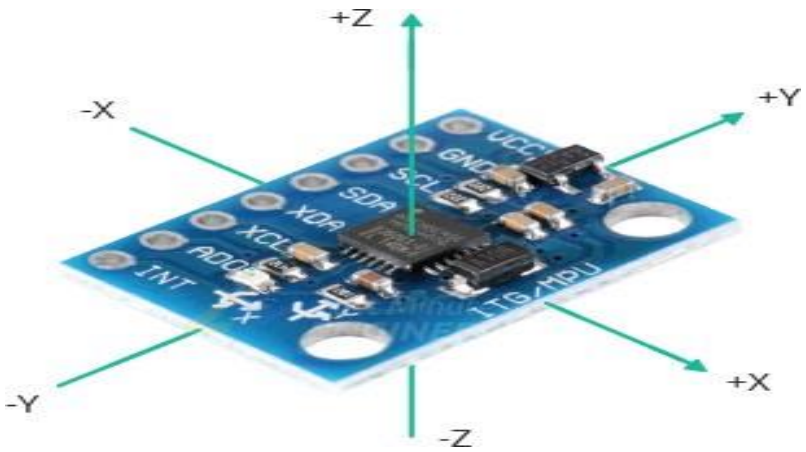

Figure Appendix B 5. Accelerometer MPU6050

B.6 DF-5 CENTRIFUGAL FAN

The DF-5 centrifugal fan is a popular industrial fan that uses centrifugal force to increase the velocity of gases passing through it. It is composed of a rotating fan wheel housed within a casing, which draws air in through the inlet and expels it at a higher pressure and flow rate through the outlet. The fan is utilized in various ventilation, heating, and air conditioning systems, as well as in industrial processes to control the flow of gases. The DF-5 centrifugal fan is known for its high efficiency, compact size, and low noise, making it a commonly used option in many applications.

Figure Appendix B 6. DF-5 centrifugal fan.

B.7 PLA. POLYLACTIC ACID (PLA)

The fuselage of this wing will be printed into parts by a 3D printer and then the body will be assembled. There are many materials that can be printed from and these materials are PLA. Polylactic acid (PLA), also known as polylactide, is indeed a thermoplastic derived from plant-based ingredients such as maize starch, tapioca roots, and sugar cane, as opposed to petroleum-based products. This material's more ecofriendly roots have made it a hit with in 3D printing sector, and it's even making its way into medicine and the food industry. The fact that PLA filament can be produced from renewable resources and has useful mechanical qualities has contributed to its widespread adoption in the additive manufacturing industry. Considering how simple it is to work with, it is frequently the material of choice for those just getting started

with 3D printing. This semi-crystalline polymer melts around 180 degrees Celsius, well below the melting point of ABS filament, which occurs between 200 and 260 degrees Celsius.

Figure Appendix B 7. Polylactic acid (PLA)

B.8 ARDUINO (MEGA)

The Arduino type (MEGA) is a device that uses sensor wires to read data from the sensor on an aircraft wing. Arduino is a free and open-source electrical platform that can turn incoming input into a digital file. The tools and accessories attached to it, The data receiver takes the signal from the board's sensors and relays it to the Arduino. As a result, the reference becomes something that is assured to work when saved on a computer or similar device.

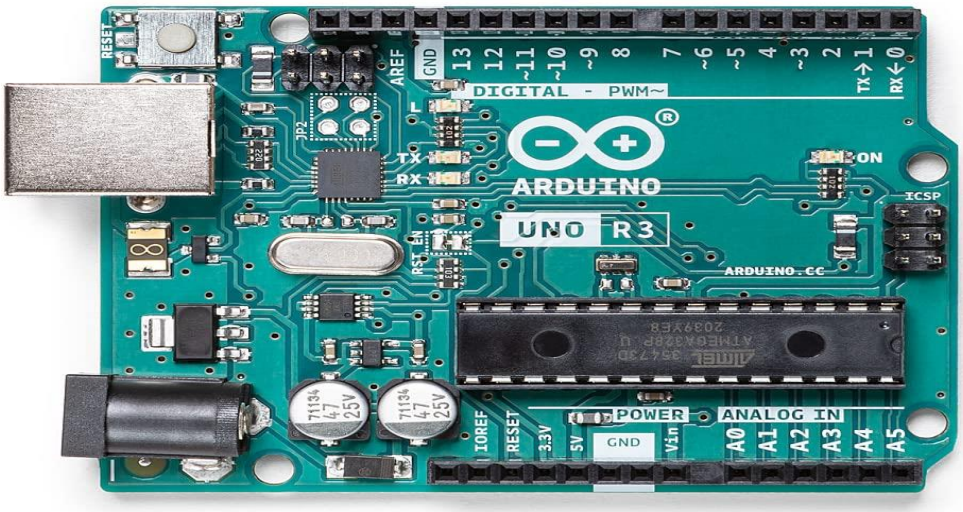

Figure Appendix B 8. Arduino (MEGA)

B.9 ARDUINO (NANO)

which is an essential component of the Arduino and is more typically when we are looking for the smallest possible Arduino board, we chose the Nano.in addition to its Mini-B USB connector, the Arduino (Nano) offers pin headers for straightforward hookup to a breadboard.. It is just an Arduino MAGE in a different case; it can do the same things. Except a regular USB port, In terms of ports, the only item missing is (DC) power jack, as well as the cable it uses, is a Mini-B USB one. The Arduino type (MEGA) is a device that uses sensor wires to read data from the sensor on an aircraft wing. Arduino is a free and open-source electrical platform that can turn incoming input into a digital file. The tools and accessories attached to it,the data receiver takes the signal from the board's sensors and relays it to the Arduino. As a result, the reference becomes something that is assured to work when saved on a computer or similar device. which is an essential component of the Arduino and is more typically, for use with a breadboard, take a glance no beyond the Arduino (MEGA)

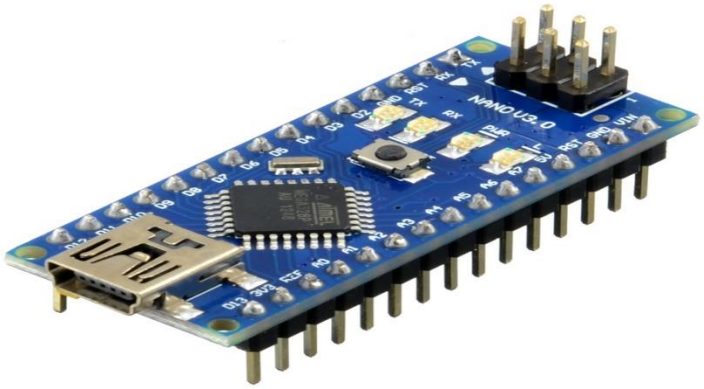

Figure Appendix B 9. Arduino (MEGA)

RESUME

Hadi Mustafa Kadhim AL-TALABA was born in DHI QAR, Iraq, and completed his education at local schools, including elementary, middle, and high school. He later enrolled at AL-FARAHIDI University in Baghdad, where he studied Aeronautical Technologies Engineering in the Engineering Technical College and graduated in 2019. After completing his studies, he worked as a teaching assistant in various Iraqi universities. In 2021, he began his graduate studies at KARABÜK University Institute of Higher Education to pursue a master's degree.